Multiscale and Multiphase Numerical Modelling of High Velocity Suspension Flame Spray Process for the Development of Nanostructured Thermoelectric Coatings

by

Ebrahim Gozali

The Thesis is submitted in accordance with the requirements of the

University of Liverpool

for the degree of Doctor in Philosophy

September 2015

Supervisors: Dr Spyros Kamnis, Prof. Sai Gu & Dr Konstantinos Papadikis

Abstract

The manufacture of nanostructured coatings by thermal spraying is currently a subject of increasing research efforts in order to obtain unique and often enhanced properties compared to conventional coatings. High Velocity Suspension Flame Spraying (HVSFS) has recently appeared as a potential alternative to conventional High Velocity Oxygen-Fuel (HVOF) spraying: for the processing of nanostructured spray material to achieve dense surface layers in supersonic mode with a refined structure, from which superior physical and mechanical properties are expected. The aim of this thesis is to, first, apply CFD methods to analyse the system characteristics of high speed thermal spray coating processes in order to improve the technology and advance the quality and efficiency of the HVSFS process. The second aim is to analyse heat transfer in thin films and thermoelectric thin films.

The first part of this thesis aims to deepen the knowledge on such multidisciplinary process and to address current drawbacks mainly due to cooling effects and reduction of the overall performance of the spray torch. In this matter, a detailed parametric study carried out to model and analyse the premixed (propane/oxygen) and non-premixed (ethanol/oxygen) combustion reactions, the gas flow dynamics of HVSFS process, the interaction mechanism between the gas and liquid droplet including disintegration and vaporization, and finally investigation of the droplet injection point (axially, transversely, and externally), at the example of an industrial DJ2700 torch (Sulzer-Metco, Wohlen, Switzerland). The numerical results reveal that the initial mass flow rate of the liquid feedstock mainly controls the HVSFS process and the radial injection schemes are not suitable for this system. The second part of this thesis focuses on investigating the effects of solvent composition and type on the liquid droplet fragmentation and evaporation, combustion, and HVSFS gas dynamics. Here the solvent mixture is considered as a multicomponent droplet in the numerical model. The numerical results can be considered as a

reference for avoiding extraneous trial and error experimentations. It can assist in adjusting spraying parameters e.g. the ratio or percentage of solvents for different powder materials, and it can give a way of visualization of the phenomena occurring during liquid spray. In the third part, effects of solid nanoparticle content on liquid feedstock trajectory in the HVSFS are investigated. Theoretical models are used to calculated thermo-physical properties of liquid feedstock. Various solid nanoparticle concentrations in suspension droplets with different diameters are selected and their effects on gas dynamics, vaporization rate and secondary break up are investigated. It is found out that small droplets with high concentrations are more stable for break up, thereby; vaporization is the dominant factor controlling the process which results in leaving some drops without fully evaporation. However, larger droplets undergo sever fragmentation inside the combustion chamber and release the nanoparticles in the middle of barrel after full evaporation. Finally a heat transfer model is developed for nanoparticles traveling inside thermal spray guns. In the absence of experimental data for Nano-scale inflight particles, the model is validated in thermoelectric thin films as candidate applications of the HVSFS process. For this purpose, one dimensional heat conduction problem in a thin film is investigated through solving three different heat conduction equations, namely: parabolic heat conduction equation (Fourier equation), hyperbolic heat conduction equation (non-Fourier heat conduction), and ballistic-diffusive heat conduction equations. A stable and convergent finite difference scheme is employed to solve the hyperbolic heat conduction (HHC) equation and the ballistic-diffusive equations (BDE). The ballistic part of the BDE is solved with the Gauss-Legendre integration scheme. Then these equations are applied across a thermoelectric thin film to investigate the steady-state and the transient cooling mechanism at the cold junction surface. The numerical results indicate that those equations predicted inaccurate results for the transient heat conduction in a thin film lead to less accurate prediction of cooling at cold side boundary, temperature, and heat flux profile in a thermoelectric film.

Contents

List of Figures

List of Tables

Acknowledgement

I would first like to take this opportunity to thank my primary thesis supervisor, Dr. Spyros Kamnis for his continued guidance throughout my research work. His genuine interest in my project, rigorous yet never overbearing supervision and dynamic personality have made this experience truly enjoyable. Through his insightful direction, Dr. Kamnis demonstrated his quality as a researcher and supervisor, and I consider myself privileged to have known him as a both mentor and a good friend. Thanks for all the good times Spyros!

I am grateful to Prof. Sai Gu for initially selecting me for doing research in his group and supervising my project throughout my PhD study.

I would also like to express my thanks and appreciation to Dr. Konstantinos Papadikis. His guidance and supervision were invaluable. I am extremely grateful for all his advices and suggestions towards writing my thesis. I am privileged to have worked with him.

Last but not least, a special thanks to all the members of my family, notably my parents, brothers, sisters and close friends who have always encouraged me in my various undertakings. To my beautiful wife Elham, thank you for everything.

Nomenclature

Chapter 3

General symbols

A constant in eddy dissipation model = 4.0

A_0 constant in realizable $k-\varepsilon$ model = 4.04

A_d surface area of a droplet (m^2)

A_s coefficient in realizable $k-\varepsilon$ model

a decreasing parent droplet radius

B constant in eddy dissipation model = 0.5

B_0 wave breakup model constant

B_1 wave breakup model constant

C_1 constant for the linear pressure-strain model = 1.8

C_2 constant for the linear pressure-strain model = 0.6

$C_{i,s}$ vapour concentration at the droplet surface $(\mathrm{kmol/m^3})$

$C_{i,\infty}$ vapour concentration in the bulk gas $(\mathrm{kmol/m^3})$

$C_{1\varepsilon}$ constant for the turbulent dissipation of energy = 1.44

$C_{2\varepsilon}$ constant for the turbulent dissipation of energy = 1.92

C_b TAB model constant = 0.5

C_D drag coefficient

C_d TAB model constant = 5

c_d specific heat capacity of a droplet at constant pressure $(\mathrm{J/KgK})$

$c_{p,\infty}$ heat capacity of the gas $(\mathrm{J/KgK})$

C_F TAB model constant = 1/3

C_K TAB model constant = 8

C_μ coefficient for turbulent viscosity

d_d droplet diameter (m)

$D_{i,m}$ diffusion coefficient of ethanol vapour in the bulk flow $(\mathrm{m}^2/\mathrm{s})$

E total energy $(\mathrm{J/Kg})$

F additional force term

G_b generation of turbulence energy due to buoyancy $(\mathrm{Kg/ms})$

G_k generation of turbulence energy due to mean velocity gradients $(\mathrm{Kg/ms})$

h convective heat transfer coefficient $(\mathrm{W/m^2 - K})$

h_{fg} enthalpy of vaporization $(\mathrm{J/Kg})$

K thermal conductivity $(\mathrm{W/mK})$

k turbulence kinetic energy $(\mathrm{m^2/s^2})$

k_c mass transfer coefficient $(\mathrm{m/s})$

$M_{\omega,i}$ molecular weight of species i $(\mathrm{Kg/Kmol})$

m_d droplet mass (Kg)

N number of chemical species in the system

N_i molar flux of vapour $(\mathrm{Kmol/m^2 - s})$

Nu Nusselt number

Oh Ohnesorge number

p pressure (pa)

p_{op} operating pressure (pa)

Pr Prandtl number

p_{sat} saturated pressure (pa)

r radial distance from centreline (m)

r_d droplet radius (m)

$R_{i,r}$ net rate of production of species i due to reaction r

R universal gas constant

Re Reynolds number

S actual surface area of a droplet

s surface area of a sphere

Sc Schmidt number

S_m mass source term

Ta Taylor number

t time (s)

U Kinematic viscosity $(\mathrm{m^2/s})$

T temperature (K)

u_d droplet velocity $(\mathrm{m/s})$

u_{rel} relative velocity magnitude between the gas phase and discrete droplet $(\mathrm{m/s})$

v gas phase velocity $(\mathrm{m/s})$

$v_{i,r}$ stoichiometric coefficient for reactant i in reaction r

$v_{j,r}$ stoichiometric coefficient for product j in reaction r

$v_{R,r}$ stoichiometric coefficient for a particular reactant R in reaction r

x_i local bulk mole fraction

Y_i Mass fraction of each species in flow

Y_M contribution of the fluctuating dilatation to the overall dissipation rate $(\mathrm{Kg/ms^2})$

Y_P mass fraction of product P

Y_R mass fraction of a particular reactant, R

y non-dimensional distortion

Greek symbols

ε turbulence dissipation rate $(\mathrm{m^2/s^3})$

μ dynamic viscosity $(\mathrm{m^2/s})$

ρ density $(\mathrm{kg/m^3})$

σ droplet surface tension $(\mathrm{N/m})$

σ_k turbulent Prandtl number for k

σ_ε turbulent Prandtl number for ε

Subscripts

eff Sum of the physical and turbulent values

i referring to one of many species

d droplet

g gas

l liquid

op operating

r radial coordinate direction

R reactant

x axial coordinate direction

∞ free stream conditions

Chapter 4

General symbols

A_d surface area of a droplet (m^2)

a averaging coefficient

c_d specific heat capacity of a droplet at constant pressure $(\mathrm{J/KgK})$

$c_{p,\infty}$ heat capacity of the gas $(\mathrm{J/KgK})$

d_d droplet diameter (m)

$D_{i,m}$ diffusion coefficient of ethanol vapour in the bulk flow $(\mathrm{m}^2/\mathrm{s})$

h convective heat transfer coefficient $(\mathrm{W/m^2 - K})$

$h_{vap,i}$ latent heat of vaporization for component i $(\mathrm{J/Kg})$

K_∞ thermal conductivity of the continuous phase $(\mathrm{W/mK})$

k_c mass transfer coefficient $(\mathrm{m/s})$

$k_{c,i}$ mass transfer coefficient of component i $(\mathrm{m/s})$

m_d droplet mass (Kg)

Nu Nusselt number

Oh Ohnesorge number

Pr Prandtl number

Re Reynolds number

Sc Schmidt number

t time (s)

T_∞ local temperature of the continuous phase (K)

T_d droplet temperature (K)

Y_s vapour mass fraction at the surface

Y_∞ vapour mass fraction in the bulk gas

Chapter 5

General symbols

C volume concentration of solid particles in suspension

a averaging coefficient

c_p specific heat capacity of titania powder (3780 J/kg-K)

k_p thermal conductivity of titania powder (10.4 W/m-K)

k_l thermal conductivity of the base fluid

Greek symbols

ρ_l density of liquid ethanol (kg/m^3)

ρ_d density of solid titania powder (4230 kg/m^3)

μ_l viscosity of liquid ethanol (m^2/s)

Chapter 6

General symbols

C volumetric specific heat (J/Km^3)

E_n exponential integral function of order n

J magnitude of the electric current

K thermal conductivity (W/mK)

l mean free path (m)

q heat flux (W/m^2)

S Seebeck coefficient (V/K)

T temperature (K)

t time (s)

u internal energy (J/m^3)

v Group velocity $(\mathrm{m/s^1})$

x coordinate

Greek symbols

θ non-dimensional temperature (K)

τ relaxation time (s)

η non-dimensional coordinate

μ directional cosine

α thermal diffusivity $(\mathrm{m^2 s^{-1}})$

σ electrical conductivity $(\Omega^{-1}\mathrm{m^{-1}})$

Abbreviations

SOFC	Solid Oxide Fuel Cell
HVOF	High Velocity Oxygen Fuel
HVSFS	High Velocity Suspension Flame Spray
CFD	Computational Fluid Dynamics
BTE	Phonon Boltzmann Transport Equation
BDE	Ballistic Diffusive Heat Conduction Equations
APS	Atmospheric Plasma Spray
STS	Suspension Thermal Spray
SPTS	Solution Precursor Thermal Spray
HHC	Hyperbolic Heat conduction
CD	Convergent Divergent
TAB	Taylor Analysis Breakup
DPM	Discrete Phase Model
TE	Thermoelectric

1 Introduction

The thermal spray process is one of the most successful technologies of all the advanced coating due to the wide variety of spray materials that can be applied to all kind of substrate materials. Thermally sprayed coatings have been used to protect components from different types of wear and corrosion [1-2]. Various base materials have been also coated with a low thermal conductivity material to increase their heat resistance. However, conventional spray techniques have limitations in terms of their coating thickness and resulting microstructure. Even though the powder manufacturers nowadays can produce very fine powder cut sizes 5-10µm allowing depositing thin dense layers down to 30µm, the main issue is that small powders are hard to handle. Novel applications such as in the field of sensor technology, development of solid electrotypes (e.g. for SOFC), thermoelectric devices, and for a new generation of nanostructured tribocoatings require thin coatings in the range of 5-50µm.

The use of liquid feedstock instead of direct processing of spray powders in the thermal spray technology is one of the most recent and promising innovations [3]. Suspension spraying provides the feasibility to form thin (< 20 µm) and dense layers, where thermally-sprayed coatings are refined with distinctive microstructural features [3-5]. High Velocity Suspension Flame Spraying (HVSFS) has been developed from the conventional HVOF spraying method in order to enable processing of Nano-structured spray material to achieve dense surface layers in supersonic mode with a refined micro or nanostructure, from which superior mechanical and physical properties are expected.

Describing a theoretical model for the HVOF process is complex, because it involves turbulence, combustion, multicomponent flow, compressible flow, multiphase interaction, subsonic/supersonic, material melting, droplet deformation, and solidification. The description is even more complex for the HVSFS process. This is primarily because a third phase, the liquid solvent, is supplementing the solid/gas two phase flow of the HVOF process, resulting in some thermochemical and thermo-

physical changes on the novel HVSFS process compared to the HVOF process, including fragmentation, evaporation, and combustion of the solvent, which can result in a cooling effect in the spray gun, and different resulting particle morphologies [4].

Regarding the thermochemical and thermo-physical sub-processes of the HVSFS process in the combustion chamber, the following phenomena have to be modelled:

i. Combustion of fuel gas, based on the HVOF process (premixed combustion),
ii. Mass, momentum, and heat transfer between the suspension droplets (organic solvent and particles) and continuous gas phase,
iii. Fragmentation, evaporation, and combustion of the suspension organic solvent (non-premixed combustion),
iv. Agglomeration of particles and heat as well as impulse transfer from combustion gases to particles (*will not be considered in this thesis*).

The chemical, thermal, thermo-physical, and morphological states of the suspension and particles during the process ultimately determine the coating microstructure and its macroscopic properties. Parameters such as droplet size, injection velocity, the location of solution evaporation and initial combustion, mass flow rate of liquid feedstock, location of injection point, flame temperature and velocity fields in the combustion chamber and expansion nozzle can all have significant influence on the final outcome in terms of the coating structure and its properties. Another important parameter which significantly influences the process characteristics, the microstructure, and phase composition of coatings is the liquid phase of the suspension which can be homogeneous or a mixture solvent. Analysing the effects of solvent type and solvent composition on suspension droplet breakup, vaporization, combustion, and gas dynamics of the HVSFS process can provide an understanding into behaviour of the liquid phase and help to achieve application-specific coatings.

Nanostructured coatings are promising candidates for high efficiency thermoelectric devices based on the Peltier effect. Thermal transport is a key factor in these low-dimensional materials for device performance since the thermoelectric figure of merit is inversely proportional to thermal conductivity and experimental studies have shown that thermal conductivity considerably decreases with materials thickness which leads to a higher figure of merit [5-6]. Therefore, understanding

thermal transport in nanostructured coatings is crucial for engineering high performance devices. Heat transfer at Nano-scales differs significantly from that in macro-scales because of size effects on the electron and phonon transport. Such size effects can be exploited for developing highly efficient thermoelectric devices.

1.1 High Velocity Oxygen Fuel Process

The High Velocity Oxy-Fuel (HVOF) process is one of the most popular thermal spray technologies and has been used in many industries due to its flexibility, good control, and a high material throughput rate compared to other thermal spray techniques. The flow field of the HVOF process is characterised by a complex combination of turbulent mixing, combustion, compressible supersonic flow, and gas-particle interactions. A typical HVOF system is initiated at the combustion chamber, where fuel and oxygen are fed in and combusted into a gaseous mixture. These gaseous products are then forced through a nozzle which accelerates them to supersonic velocity. The coating in powder form may either be fed by a carrier gas into the combustion chamber or downstream after the convergent-divergent nozzle. The ability of this process to propel the powder particles at high velocity without overheating them is its most salient feature. The powder particles which most commonly range in size from 5 μm to 80 μm are softened or melted by the hot gas while being carried to a targeted substrate to build up coatings up to mm thickness. Mainly ceramic coatings applied via HVOF which have been extensively improved and extend product life by providing anti-corrosion, corrosion-resistant, wear-resistant surface layers, anti-adhesion, or combination of these properties. Nevertheless, the traditional HVOF process is merely suitable for the processing of micro-scale powders and has distinct restrictions in powder size due to powder supply [7]. This means that the HVOF process should be go through some adaptations for the processing of Nano-scale powders.

1.2 High Velocity Suspension Flame Spraying

Thermal spray represents a potential efficient technology for the manufacture of thermoelectric generators in order to extend their use for waste heat recovery at large surfaces and high service temperatures. However, thermal spray technology meets

certain challenges from both material and technological side. The efficiency of these devices is related to their basic material properties, through the dimensionless thermoelectric figure of merit, ZT. The figure of merit is defined as $ZT = S^2\sigma T/K$, where S is the thermopower or Seebeck coefficient, σ is the electrical conductivity, K is the thermal conductivity, and T is the absolute temperature. The ZT value for the best bulk materials is approximately unity, corresponding to about 10% Carnot efficiency, and has improved only incrementally in the past several decades. Nanostructured coatings by thermal spraying can be an effective way to reduce thermal conductivity of thermoelectric materials due to phonon scattering by pores and cracks in the coating. As a result, processes that enable to manufacture nanostructured coatings are being investigated in current research efforts. Referred to as high velocity suspension flame spraying (HVSFS), this relatively novel process is very promising for the manufacture of nanostructured coatings for a large range of applications [8].

One of the major challenges in processing nanoparticles by thermal spraying is their precise injection into the core of the high-enthalpy flow. As such, decreasing the particle average size down to the nanometre scale requires a significantly higher injection force equal to that imparted to them by the flow. In turn, the increased cold carrier gas flow rate requirement disrupts the high-enthalpy flow [3, 9].

Agglomeration of Nano-sized particles into micro-sized ones and their injection using a conventional injection route based on carrier gas is a first possibility to circumvent such a drawback [10]. Since in the agglomerated particles the molten front travels slower compared to the one in fully dense particles of the same diameter, the lower apparent density of those particles has to be taken into account when adjusting the particle momentum upon injection by adjusting the carrier gas flow rate together with other operating spray parameters. Although particle handling is easier, the disadvantage of this approach is that the coating does not show a complete nanometre-sized structure. Indeed, the strategy employed is that the operating parameters must be adjusted in a way that particles impinge the substrate in a semi-molten state. Upon solidification, the non-molten fraction of particles (inner core) keeps their nanometre-sized structure whereas the molten fraction of particles (outer shell, for single-element particles) generates micrometre-sized zones in the coating ensuring cohesion.

Suspension thermal spraying (STS) is a novel solution for injecting Nano-sized particles into the high-enthalpy flow, in which the carrier gas is replaced by a liquid. In this method, the nanoparticles are dispersed into the liquid phase with the aid of dispersants. Depending upon the spray torch design, the suspension is either radially or axially and either as a liquid stream or as drops after nebulization, injected into the high-enthalpy flow. The liquid stream or droplets are either fragmented due to flow shear forces and vaporized, or no fragmentation and only vaporization occurs, depending upon the flame jet conditions and the way of suspension injection.

High velocity suspension flame spraying (HVSFS) is based on the conventional high velocity oxy-fuel (HVOF) thermal spraying process and was developed with the aim of spraying submicron or nanoparticles suspensions with hypersonic speed to deposit thin and very dense coatings. Using a solution as the carrier fluid for processing nanostructured materials features some thermochemical and thermo-physical changes of the new HVSFS process compared to the standard HVOF process. These include a third phase (liquid), its fragmentation, evaporation and combustion including a cooling effect in the spray torch, whereas the resulting particle morphologies are different from the conventional HVOF process. Despite the fact that the first HVSFS method was introduced in 2006, compared to suspension plasma spraying, there has only been little effort on understanding the effects of process parameters on the coating quality. Several experimental studies have been conducted to illustrate the great potential of this system in producing nanostructured coatings. However, for a three-phase flow system (combustion gases/liquid droplets/spray particles) involving chemical reactions such as in the HVSFS process, the heat and mass transfer processes and interaction between the process boundary conditions are very complicated, making experimental process optimization a costly and time intensive procedure. Moreover, the measurement and analysis of gas, liquid, and nanoparticles behaviour with diagnostic tools within the system is not feasible.

Computational fluid dynamics (CFD) can be a valuable tool to provide information on phenomena occurring within the system or parts of the system that would not otherwise be visible. Numerical modelling can provide enhanced understanding of the designs and a means of visualization. Design and process optimization can be done with numerical modelling before physical prototyping and testing. The predictions can lead to better design and good understanding of the process parameters involved in HVSFS thermal spray technology.

1.3 Overall Aim and Objective of the Thesis

The aim of this thesis is to provide to the thermal spray community, new computational approaches and viewpoints in an effort to improve the technology and advance the quality and efficiency of the HVSFS thermal spray process.

The specific objectives of the research project are:

1) Discover optimum operating parameters for the HVSFS process in order to reduce the cooling effects and optimize the process.
2) Investigate the effects of solvent type and composition on the liquid feedstock disintegration, vaporization, combustion, and the HVSFS gas dynamics.
3) Investigate the effects of nanoparticle concentration and droplet size on the suspension feedstock vaporization, fragmentation, and the HVSFS gas dynamics.
4) Model and analyse the premixed combustion and gas dynamics, including modelling of the suspension evaporation, non-premixed combustion, secondary breakup, and analysis of the interaction mechanisms between gas and liquid.
5) Model and analyse the multicomponent droplets evaporation, non-premixed combustion, and breakup, including analysis of their interaction with the gas phase.
6) Investigate the transient heat conduction in thin film and thermoelectric thin film including analysis of the cooling mechanism in nanostructured thermoelectrics.
7) Develop a heat transfer model for nanoparticles travelling inside thermal spray torches.

Each research chapter of this thesis represents a standalone contribution consisting of a concise introduction, modelling approach and results and discussion sections. These chapters are summarised in Section 1.4.

It should be noted that there are very limited numbers of numerical studies in the literature about HVSFS process since most of the work undertaken to date in this field mostly focused on plasma and HVOF spraying processes. To the best of our knowledge, there is only one numerical investigation of the HVSFS process

conducted by Dongmo et al. [11]. Even though this research work provides an insight into the process, there exist considerable limitations and drawbacks about their modelling approach and outcome which are analytically presented in Chapter 2. Hence, the novelty of the thesis is reflected in the previously mentioned objectives of the project.

1.4 Thesis structure

The contents of this thesis have been organized into seven chapters. Chapter 1 presents a general introduction of the background information relevant to the current research project.

Chapter 2 provides a detailed account and review of the relevant literature for this research project. A description of the conventional high velocity oxygen fuel spraying (HVOF) in this study is presented as well as a more thorough investigation of the HVSFS process.

Chapter 3 aims to deepen knowledge on such multidisciplinary HVSFS process and to address current drawbacks mainly due to cooling effects and reduction of the overall performance of the spray torch. For this purpose, a detailed parametric investigation has been conducted by modelling and analysis of premixed (propane/oxygen) combustion and gas flow dynamics of HVSFS process, modelling of secondary non-premixed (ethanol/oxygen) combustion, analysis of the interaction mechanism between gas and liquid droplet including disintegration, vaporization and finally analysis of the droplet injection point (axially, transversely, and externally), at the example of an industrial DJ2700 torch (Sulzer-Metco, Wohlen, Switzerland). [12]This investigation will provide optimum parameters for controlling and optimizing the HVSFS process which can significantly influence the final outcome in terms of the coating structure and its properties. These parameters include injection velocity, initial droplet size, initial combustion and the location of solution evaporation, velocity field and flame temperature in the combustion chamber and expansion nozzle.

[1] Published: Gozali, E. Kamnis, S. and Gu, S. (2013). Numerical investigation of combustion and liquid feedstock in high velocity suspension flame spraying process. *Surface and Coating Technology*, 228, pp.176-186.

[2] Published: Gozali, E. Kamnis, S. and Gu, S. (2013). Analysis of Liquid Feedstock Behaviour in High Velocity Suspension Flame Spraying for the Development of Nanostructured Coatings. *Proceedings of the International Thermal Spray Conference*, ASM International.

Chapter 4 deals with the effects of solvent type and solvent composition with different mixing ratios on the liquid droplet fragmentation, evaporation, combustion, and HVSFS gas dynamics[3]. In this investigation the solvent mixture is treated as a multicomponent droplet of ethanol and water with various ratios. It should be noted that modelling the solvent as a multicomponent droplet has not yet been addressed in the thermal spray literature. This work aims to bridge this gap and to provide information that help to depict the mixture solvent behaviour in the HVSFS process. The numerical model consists of several sub-models that include modelling HVSFS flame jet turbulence by taking into account the compressibility effects, premixed combustion of propane-oxygen, non-premixed combustion of ethanol-oxygen, modelling aerodynamic of single and multicomponent droplet breakup, evaporation, and heat and mass transfer between liquid and gas phases, using an industrial DJ2700 torch (Sulzer-Metco, Wohlen, Switzerland).

Chapter 5 copes with the influence of nanoparticle concentration and droplet diameter on the vaporization rate, the secondary breakup of the liquid phase, and the HVSFS gas dynamics[4]. The numerical analysis for this study consists of modelling pre-mixed (oxygen/propane) and non-premixed (oxygen/ethanol) combustions, the interaction between gas and liquid phases (two-way coupling), as well as secondary break-up and vaporization of droplets. Moreover, for modelling the suspension, the thermo-physical properties are calculated from the theoretical models.

Chapter 6 attempts to develop a heat transfer model for nanoparticles moving inside a thermal spray torch. Heat transfer at Nano-scales differs significantly from that in macro-scales because of size effects on the phonon transport. For the Nano-scale heat transfer analysis, a phonon Boltzmann transport equation (BTE) can be an accurate method in this regard. The BTE, even in its simplest form, however, is difficult to solve because it involves variables in real and momentum spaces, as well as time. A ballistic-diffusive heat conduction equations (BDE) is established and demonstrates that they are a good approximation of the BTE. Therefore, the heat conduction problem is investigated in a thin film by solving numerically the BDE along with the

[3] Published: Gozali, E. Mahrukh, M. Gu, S. and Kamnis, S. (2014). Numerical analysis of multicomponent droplets in high velocity flam spray process. *Journal of Thermal Spray Technology*, 23(6), pp. 940-949.

[4] Published: Gozali, E. Mahrukh, M. Gu, S. and Kamnis, S. (2015). Effects of nanoparticles on liquid feedstock behaviour in high velocity suspension flame spray process, *Surface and Coating Technology*.

hyperbolic and parabolic heat conduction equations. These equations are applied across a thermoelectric thin film in order to analyse the transient heat conduction and cooling mechanism at the cold junction surface[5].

Finally, Chapter 7 provides a summary of the major conclusions of the current research, and presents recommendations for future work in this area. The recommendations primarily focus on the potential improvements on the integrated CFD modelling of the single and multicomponent nanoparticle loaded solvent droplets, as well as on the nanoparticle heat transfer modelling approaches applied to particles travelling inside thermal spray torches.

[5] Under-review: E. Gozali, S. Kamnis, and S. Gu. Heat Transfer in Nanostructured Thermoelectrics, International Journal of Heat and Mass Transfer, 2015.

2 Literature Review

2.1 High Velocity Oxygen-Fuel Spraying

In the simplest terms possible, the thermal spray processes represent a group of particulate deposition processes in which a material, in powder or wire form or dissolved or suspended in a liquid, is propelled and heated in a gas/plasma stream and deposited on a given substrate in a molten or semi-molten state, and the coating microstructure results from the solidification and sintering of the particles. Either burning mixtures of fuel gas and oxygen, or an electrical power source provides the thermal and kinetic energy to the flame. In total, thermal spray techniques based on their energy resources can be divided into main groups, namely: plasma spray techniques, high velocity oxygen fuel techniques, flame spray techniques, electrical arc techniques, and cold spray techniques [12-14]. The coating, in thermal spraying, is created by fast solidification of the semi-melted or melted droplets attached to the substrate. The main properties of coating are defined by the flattening degree and adhesion between the lamellas, together with the coating material itself, where a typical structure for the coating is a pancake-like lamellar structure. The particle velocity when attaching to the surface and melting behaviour mainly define the porosity and adhesion of the coating. Moreover, in thermal sprayed coatings, some special features such as the metastable phases and residual stresses can be observed due to the fast cooling rate of the particles [12-14].

Among thermal spray methods, the HVOF (high velocity oxy-fuel) spraying is mainly used for producing corrosion and wear resistance coatings. The HVOF process uses the combustion of mixtures of oxygen and fuels for melting and accelerating powder particles, in order to deposit the desired coating. Hydrocarbon gases or pure hydrogen are normally used as the fuel gas. A jet with supersonic speed is produced due to convergent-divergent nozzle design. The relationship between the thermal and kinetics energy of the process described by the flame temperature and particle velocity distinguish the HVOF process from other commonly used processes, such as

Atmospheric Plasma Spray (APS). The energy, in APS, is based on the plasma created by ionizing an inert gas, normally a mixture of helium and argon, between the cathode and the anode in the spray gun. Compared to the HVOF process, the resulting plasma flame temperature is very high. Good melting of the ceramic particles for producing ceramic coatings is enabled by APS due to the high process temperature. Nevertheless, dense ceramic coatings are, also, deposited by HVOF [15-18].

The production of dense coatings is the main feature of HVOF process, which hinders extra oxidation and phase transformation due to short inflight time of powder particles in relatively cold flame. Thermal spray coatings have been conventionally used on extending the life of the sprayed component, while HVOF is extensively applied to fabricate metal coatings. The pioneering industry was the aerospace which realized the great potential of the process. Applications of the process are jet engine components such as compressor stators, compressor air seals, stiffeners, and fan duct segments. The process includes a number of variables and it is very complex, despite the extensive industrial use of thermal spraying. There must be obtained a better understanding of the relationships of these variables and their effect on the coating properties in order to apply thermal spray coating to "prime reliant" applications.

2.1.1 Methods and Technology of HVOF Thermal Spray Process

HVOF operates under a continuous regime where a combustion gas and a fuel (usually hydrogen, propylene, propane, acetylene or kerosene) are burnt in an air cooled or water-cooled combustion chamber. The resulting flame is then fed into a converging/diverging expansion nozzle, also known as the barrel. The hot combustion gases are accelerated in the nozzle at supersonic velocities, leading to jet temperatures of approximately 3000°C and velocity range from 1525m/s to 1825m/s. The feedstock powder particles are injected at the rear of the spray gun in the same axial direction as the flame. Upon exposure to the high temperature and high velocity flame, the particles experience a significant increase in thermal and kinetic energy, thus resulting in partially melted and/or softened high-velocity particles. Coating formation in HVOF is therefore attributed to the combined effect of splat formation and plastic deformation of the particles upon impact with the substrate [12]. Figure 2.1 shows a diagram of a typical HVOF spray gun cross-section.

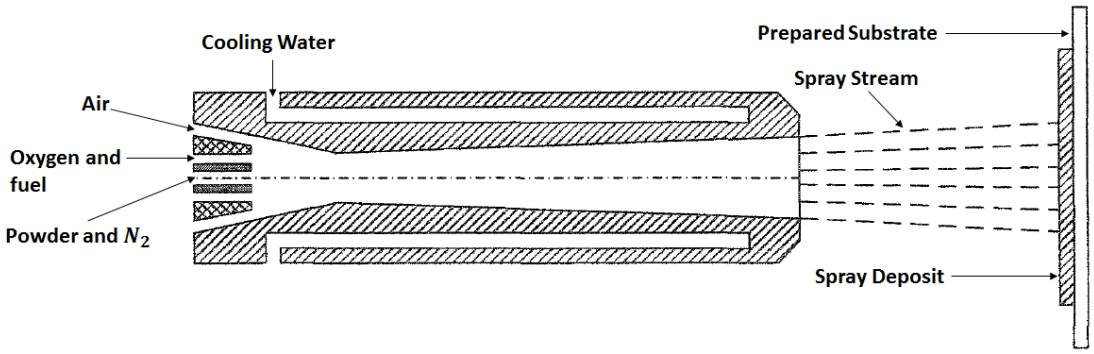

Figure 2-1: Schematic representation of a typical HVOF gun [12]

HVOF process is of great potential in producing coatings from those powder materials that are sensitive to phase transformation due to evaporation or oxidation. This is due to its process condition, which combines a relatively low flame temperature with a low exposure time in the flame. There exist a few different HVOF systems with quite different gun designs and capacities. The difference lies in their design, but all are based on the same fundamental principles. Hypersonic gas velocities are generated with the combination of gas flow rates of several hundred litters per minute and high pressure (over 4 bar) [18]. Division of these systems can lead to the first, second and third generation. The pressurized combustion of gaseous fuel with oxygen creates an exhaust jet moving at a speed of about 1500 to 2000 m/s in all first and second generation guns. Jet Kote, Diamond Jet (DJ), HV-2000 and CDS spray systems belong to this category. These systems, under standard spray conditions, use a power level of about 80 kW for operation and can spray about 2-3 kg/h of WC-Co. The third generation systems are operated at a power levels ranging from 100 to 200 kW and are capable of spraying about 10 kg/h. The difference between the previous ones and the third generation systems (JP-5000 and DJ Hybrid) is the operation at higher chamber pressures (8 to 12 bar versus to 3 to 5 bar) and higher gas/fuel flows [18-20].

2.1.2 Modeling of HVOF Process

The first CFD study of the HVOF thermal spraying process has been performed by [21-22]. In this study, both the external and internal flow of the Metco Diamond Jet gun is modelled. The model includes the combustion chemistry and standard $k-\varepsilon$ turbulence model. The chemistry model uses an approximation equilibrium model and

seven gas species: C_3H_6; O2; N2; H2O; CO2; CO; and H_2 for dissociation of the reaction products. An explicit time iterative scheme is used to solve the finite difference equations, using a density based formulation. The local gas velocity and temperature are used for tracking particles. Phase change of particles is not considered in this analysis.

Two-dimensional computational fluid dynamic (CFD) methods have been developed to simulate more complex physics. The internal and external computational domains with respect to gun are fully coupled in a commercial CFD code, originally designed for aerospace applications, using the finite volume method [23]. An iterative, segregated solution method with a Semi-Implicit Method for Pressure-Linked Equations (SIMPLE) is used. A one-dimensional approximate equilibrium chemistry model including the dissociation of the gaseous products is used for modelling the combustion.

More reactions and species in the combustion model are included in the computational study [24] to predict a more accurate flow field regarding the speed of the premixed methane and flame temperature. Assuming that most particle heating and acceleration occur in the barrel, the free jet outside the torch is not included in the simulation. However, at the free jet, cooling of the particles and deceleration should not be ignored because of their effects on final outcome of coatings. Also, for simplicity the combustion chamber is not included. Equilibrium conditions are used to determine the combustion chamber exit conditions, assuming complete combustion of the fuel. The particles temperatures and calculated gases are found to be slightly higher than the experimental results due to the model assumptions. Three-dimensional studies for heavier particle loading rates or different gun geometries are necessary as well as a complete simulation of spray combustion in the combustion chamber. The discretization schemes used to resolve the conservation equations determine the numerical stability and accuracy of the highly compressible flow. The first order of accuracy upwind scheme is used in many studies, which makes difficult the capture of the shock diamond inside the nozzle and free jet.

To capture shock diamonds in the free jet region, a second order of accuracy scheme is employed; however, only two shock diamonds are observed in the results [25]. Compressibility effects at the free jet region are successfully captured by only third order schemes such as the well-known QUICK [26]. Although the accuracy of solution is increased by the QUICK scheme, the solution may show unphysical

oscillations and unacceptable unbounded values for turbulence quantities or species concentrations. More accurate results are obtained for the gas flow by a number of research works using higher order discretization schemes [27-29].

Compressibility effects in the flow, combustion, and turbulence are appropriately represented in a comprehensive 2-D model [27]. To account for the effect of turbulence with standard semi-empirical wall functions in the cells adjacent to walls to represent turbulence boundary conditions, the improved renormalization group (RNG) $k-\varepsilon$ turbulence model is used [30]. Higher-order interpolation schemes are used to settle compressibility effects in the supersonic jets. There is a good agreement with experimental measurements. The combustion process is treated by an approximate, single-step, equilibrium formula that takes into account the effects of dissociation. It is assumed that propylene and oxygen react immediately upon entering the computational domain. Since propylene is a fast burning fuel, the assumption of rapidly reaction makes sense and become necessary in view of the fact that detailed multi-step reaction kinetics are very complex and speed limitations of the computers make it very difficult to simulate numerically. Different assumptions are made in a list of studies regarding the reaction rate (1) finite reaction rate limited by turbulence mixing [28-29]; (2) infinitely fast reaction rate [23, 27, 31]; finite reaction rate in Arrhenius form [32-34].

The authors have shown that fuel flow rate, total flow rate of fuel and oxygen (oxy-fuel flow rate), total inlet gas flow rate, and barrel length are the most sensitive parameters affecting the process. Increasing the total inlet gas flow rate increases the total thermal inertia and momentum inertia however; increasing the total inlet gas flow rate has limited effect on the gas temperature and velocity inside the nozzle. Flame temperature and velocity are significantly increased by increasing the oxy-fuel flow rate, particularly after exiting the nozzle.

There exist several drawbacks in the model, despite the good results provided by the authors. Only in the case of symmetric torches, a 2-D axisymmetric domain can be implemented. This case is almost limited and makes constrains on the powder feeding methods and torch design. The shock diamonds are not completely captured as compared with experimental results. The implemented standard wall functions by the authors are based on relatively simple empirical laws and in highly compressible flows may not accurately predict the local flow quantities. The inaccurate prediction of the flame thickness and stretch inside the combustion chamber is an immediate

defect. The supersonic jet expansion is considered for the model validation and any validation of the combustion model through the free jet temperature is excluded.

Only recently a CFD model has been developed to investigate the gas dynamics and combustion in a liquid-fuelled HVOF thermal spray gun [35-36]. The supersonic shock diamonds closely aligned the experimental observation in the free jet region are captured by using the third-order discretization scheme. Shock waves are also found in the thermal spray gun. Turbulence fluctuations critically affect reacting flow in the combustion chamber. Figure 2.2 shows schematically a liquid fuelled HVOF thermal spray gun. Figure 2.3 shows the trajectories of fuel droplets at various sizes. It is shown that the combustion process of liquid fuel is dependent on the initial fuel droplet sizes. Large droplets have dispersed fan-shape flame structure and less uniform temperature profiles while the small droplets generate a confined corn-shape flame and give more uniform temperature profile within the combustion chamber.
Moreover, there are well documentations about models describing the inflight behaviour of particles during HVOF spraying [23, 24, 31, 34, 37]. There are three types of models from the viewpoint of solution methods of governing equations for two-phase systems: semi-coupled [23, 24, 32, 37], coupled, and decoupled [31]. Since Eulerian approach, the coupled method, is not used in HVOF processes, only Lagrangian methods are discussed.

However, to advance the technology and manufacture smarter coating, the existing thermal spray methods must be modified in such a way that to process Nano-sized powders. In the case of HVOF thermal spraying process, it must be modified to high velocity suspension flame spray (HVSFS) process to produce finely-structured coatings. This requires some changes in the operating parameters and likely in gun design. Section 2.2 is devoted to the literature review of this new process.

2.2 HVSFS Thermal Spray Process

Thermal spraying of Nano-sized particles can largely provide benefits to high-efficient power converting devices such as solid oxide fuel cells (SOFCs) and thermoelectric (TE) devices. The high number of components and overall manufacturing costs, high performance requirements, long term stability, thermal cycling capability, and long start-up times are, currently, the main difficulties preventing the widespread implementation of SOFCs. Operating these units at tempe-

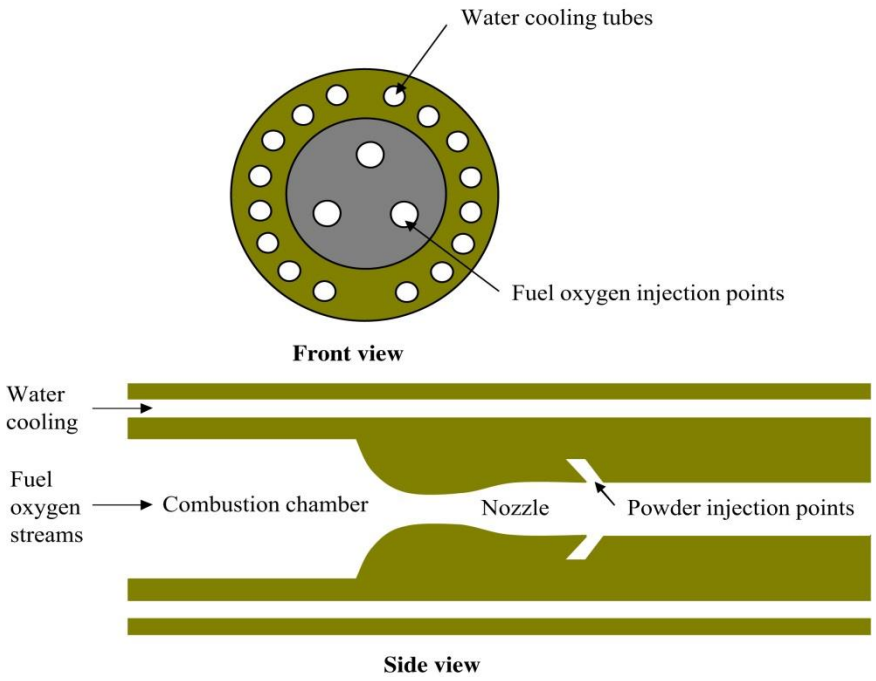

Figure 2-2: Schematic diagram of a liquid-fuelled HVOF thermal spray gun [36]

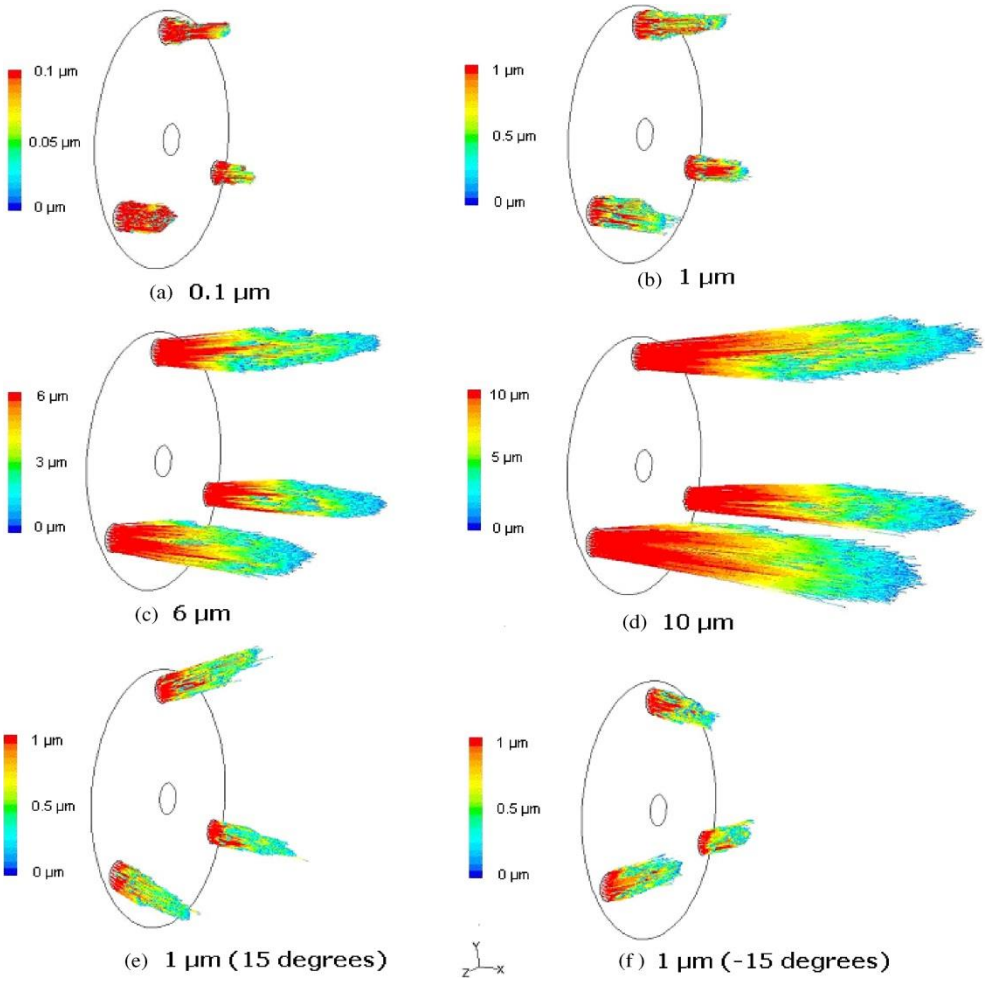

Figure 2-3: Droplet trajectories showing the droplet size evolution [36]

ratures far below the conventional 1000 ℃ can provide many benefits over the traditional types, allowing: increased structural robustness, low-cost peripheral material, reduced degradation, thermal stability, and increased flexibility in design and assembly [38]. Reducing the electrolyte thickness is one way to compensate for the increased resistance to ion transport at lower temperatures within the electrolyte. It is crucial a dense, thin, fully crystalline electrolyte layer is present to separate the fuel from the oxidant atmosphere [39]. Therefore, the thermal spray processing of nanoparticles is gaining attention in this field. The suspension spraying approach permits the deposition of nanoparticles to fabricate thinner coatings with a more refined microstructure and grain size [40]. Figure 2.4 depicts an example SOFC. The electrolyte depicted was produced by HVSFS process and the anode was produced by suspension plasma spraying [38].

There has always been a growing desire to deposit nanostructured films as part of the interest in developing more complex thermal spray coatings. However, current techniques must be adapted in order to deposit submicron and Nano-sized particles. A Nano-powder feedstock has to be mixed to form a suspension (suspension thermal spraying, STS) or a solution precursor (solution precursor thermal spraying, SPTS) for both health and safety reasons as well as to avoid particle agglomeration during storage and feeding into the spray device. The liquid injection method also increases the momentum of the feedstock particles, aiding penetration into the thermal jet core. STS and SPTS are more complex as compared to the conventional thermal spray methods due to the final particle morphology being larger controlled by the rates of vaporization and fragmentation of the liquid component of the feedstock upon injection. In the fields of STS and SPTS, the consistently high level of interest is reflected in a number of review papers [41-44]. In all, a variety of thermal spray methods have been utilized in pursuit of depositing nanoparticles from a liquid feedstock, including: plasma, flame, and HVOF. An overview of these achievements is provided as follows.

In the plasma spray method, Al_2O_3, TiO_2, and Hydroxyapatite (HA) are some of the most popular materials being deposited as a suspension. Their respective function include: photo-catalytic devices, prosthetics, and corrosion and wear protection. Fine splat morphologies and superior control of coating porosity, which are key features of prosthetic coatings, are achieved by SPTS of HA using a plasma torch [45]. Liquid feedstock plasma spraying has successfully deposited TiO_2 nanoparticles and achieved

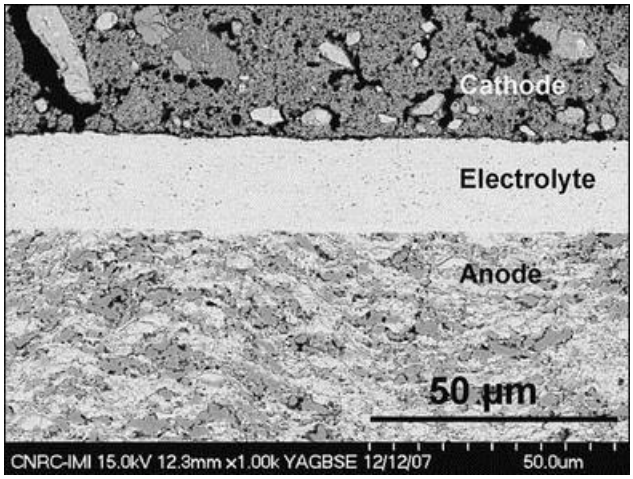

Figure 2-4: An example solid oxide fuel cell produced by HVSFS technique [38]

grain sizes of roughly 40 nm, and a high proportion (90 %) of desirable anatase phase; vital in the production of photo-catalytically active coatings [46]. Liquid feedstock alumina has also been deposited by plasma spraying with controlled coating density and with high levels of thermodynamically stable corundum (α-Al_2O_3); which is necessary for good wear resistance and electrical insulation [47].

The high velocity suspension flame spray (HVSFS) technique, based on existing HVOF technology, has depicted a great potential for the deposition of submicron and Nano-sized particles due to its controllable flame characteristics and high momentum throughput which can be utilized to improve the particle impact conditions. Consequently, dense TiO_2 coatings with good adhesion on steel substrate are formed [42]. Moreover, Al_2O_3 nanosized particles are utterly melted by this process, leading to extremely low interconnected porosity and little inter-lamellar defects [38].

When the suspension is made of water, poor coatings are obtained due to insufficient flame temperature. Much better results are obtained with ethanol, but even a low percentage of water in ethanol drastically cools the flame. Injecting combustible liquids raises the combustion chamber pressure, resulting in instabilities in the acetylene flow (acetylene–oxygen giving the highest combustion temperature). Thus propane and ethane are used [4] to achieve stable flames with the Top-Gun system while Oberste-Berghaus et al. [48] have chosen propylene with the DJ2700 system.

There are, however, very limited numbers of numerical studies in the literature about HVSFS process since most of the work undertaken to date in this field is mostly focused on plasma and HVOF spraying processes. This is merely due to the fact that

this process has been newly developed. To the best of our knowledge, there is only one numerical investigation of HVSFS process conducted by Dongmo et al. [11]. The work is 3D modelling and analysis of the combustion and gas dynamic phenomena of the HVSFS process, including the modelling of ethanol evaporation and analysis of the interaction mechanisms between gas and liquid as well as between gas and particles, performed at the example of an industrial TopGun-G torch. The computational domain is shown in Figure 2.5. An Eulerian approach is used to solve the thermal and flow fields of gas while the particle trajectory is modelled in a Lagrangian fashion. The turbulence model is the k-ε and the eddy dissipation and the finite rate chemistry models are used to solve pre-mixed propane/oxygen and non-premixed ethanol/oxygen combustions respectively. A liquid evaporation model is employed to predict heat and mass transfer between two phases. The model uses two mass transfer correlations depending on whether the droplet is above or below the boiling point. The boiling point is determined through the Antoine equation. Finally, it is mentioned that particle break up is modelled using the Blob method for disperse droplets and ETAP method for disperse solids according to Weber and Reynolds number of each particle.

The modelling results showed that the ethanol evaporation and combustion take place in the barrel of the gun lead to highly cooling the gas temperature and disturb the energy balance. Figure 2.6 illustrates the HVSFS flame temperature along with temperature of liquid fuel and particles in the computational domain. Ideally cooling of the gas temperature should be minimized to a very small amount and occur inside a combustion chamber. This will contribute the enthalpy of combustion and not imbalance the thermal and flow fields of HVSFS process. However, this study does not analyse the secondary break up of liquid droplets, which is found in this thesis play an important role. Furthermore the evaporation effects on the gas dynamics are not examined thoroughly. Compressibility effect and shock diamonds are not captured outside the gun and only axial injection scheme is used for the analysis of droplet injection.

HVSFS process compared to HVOF is more complex. The chemical, thermal, thermo-physical, and morphological states of the suspension and particles during the process ultimately determine the coating microstructure and its macroscopic properties. Parameters such as droplet size, injection velocity, the location of solution

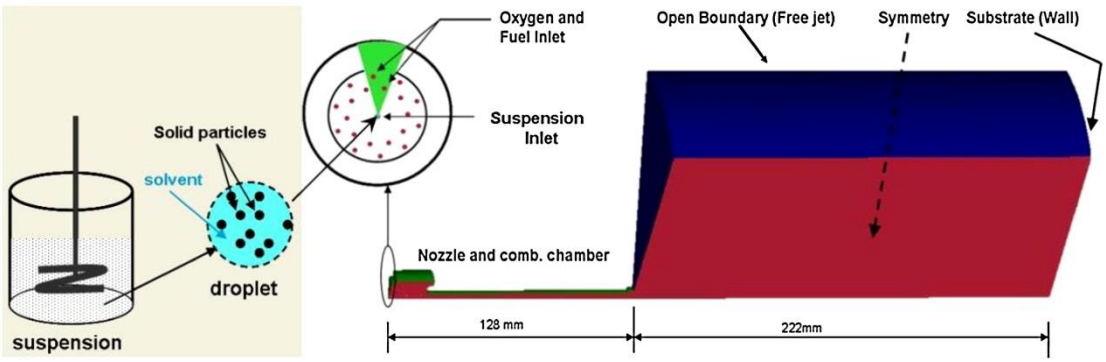

Figure 2-5: The computational domain of 3D symmetrical segment of the HVSFS process (TopGun-G torch) [11]

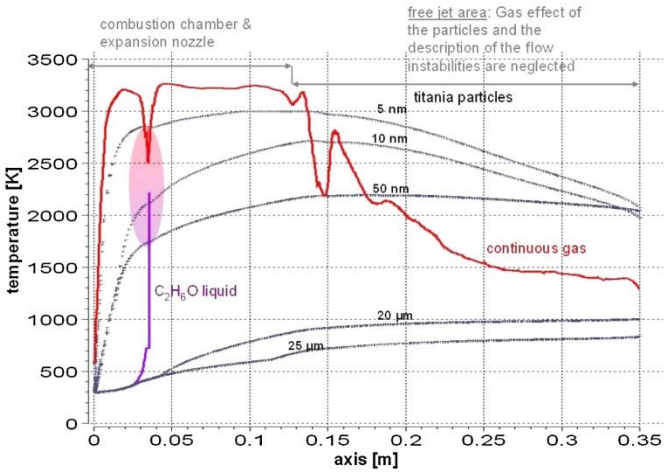

Figure 2-6: Temperature profiles of gas, ethanol and titania particles (with different particle size) along the centerline from the combustion chamber to the substrate [11]

evaporation and initial combustion, mass flow rate of liquid feedstock, location of injection point, flame temperature and velocity fields in the combustion chamber and expansion nozzle can all have significant influence on the final outcome in terms of the coating structure and its properties. Therefore, more numerical studies are required to be conducted to deepen knowledge on such complex process and to address current drawbacks mainly due to cooling effects and reduction of the overall performance of the spray torch.

The process characteristics, the microstructure, and phase composition of the coatings are significantly influenced by the liquid phase of the suspension which can be homogeneous or a mixture solvent. Depending on the desired application, different types of solvent or mixture ratio are used. Solvent mixtures are recently employed in most of the HVSFS experiments mainly for the effective control of the degree of

melting of nanoparticles or agglomerates and for modifying the physical properties of the solvent in order to achieve application-specific coatings [49-51]. Ethanol, isopropanol, water, and their mixture are the most commonly used solvents.

Only few research groups have systematically studied the effects of suspension or solution composition on the processes and the microstructural properties of the coatings [49, 3, 52-53]. These experimental studies are largely focused on the effects of powder size distribution and type of solvent on nanostructured coatings. Most of these works investigate the effects of suspension or solution composition on the final outcome of the coatings and the process. The underlying physics is not elaborated due to the experimental limitations. None of these studies examined the effects of solvent mixture ratio on the process and microstructure of the coatings, for example, how the solvent composition influences the gas dynamics of the HVSFS process or at what extent suspension fragmentation and evaporation will be altered with different ratios of solvent mixture in the liquid phase. In all techniques, the solvent breakup and evaporation are the initial steps for the droplets to undergo further physical and chemical transformations. Hence, understanding the liquid phase (homogenous and mixture solvent) breakup, evaporation, combustion, and its effects on the gas dynamics can further improve the process and coating structure. Moreover, no numerical investigation has been conducted on this matter.

In the HVSFS process the concentration of suspended solid nanoparticles in the solvent may vary from one case to another, depending on the application. The thermo-physical properties of suspension such as density, viscosity, specific heat, thermal conductivity and surface tension do not remain constant but differ according to nanoparticle concentration [54-60]. In addition, rate and final location of droplet evaporation in a thermal spray torch is critically governed by the physical properties of the solvent. This implies that assigning pure solvent properties or averaging solid and liquid properties in the suspension analysis may produce unrealistic results leading to a high level of errors in numerical simulations. Therefore, a substantial research is demanded to provide a quantitative comparison between the vaporization rate of a typical homogeneous liquid solvent (ethanol) and non-homogeneous liquid suspension (ethanol carrying nanoparticles).

In the HVSFS process, the nanoparticles thermal behaviour under different operating conditions is very important as eventually coating microstructure is determined by nanoparticles states in the process. Moreover, in the application of

HVSFS process for fabricating thermoelectric thin films, heat propagation in these low-dimensional materials is a key factor for device performance since the thermoelectric figure of merit is inversely proportional to thermal conductivity. Hence, understanding heat transfer in nanostructured materials is crucial for engineering high performance devices. It is essential to develop a numerical model to describe energy transport in nanoparticles, thin films and thermoelectric thin films. Thermal energy transport at scales comparable to phonon mean free path is a key factor to optimize the process and outcome of coating structure.

Fourier's law has usually been used to describe heat transfer process and predict temperature distribution in nanoparticle powders in thermal spray process [59-61]. Also, this law has been employed to model heat conduction problem in thermoelectric elements [62-63].This law, which implies that heat propagates at an infinite speed, is sufficiently accurate for engineering problems under regular conditions. However, for situations involving very high temperature gradients, very low temperatures near absolute zero, or extremely short times, heat is found to propagate at a finite speed and ballistic nature of the heat carriers becomes significant. As the characteristic dimension of the heat conduction medium decreases to Nano-size, Fourier's law leads to unreasonable results [64]. Heat conduction in micro- and Nano-scale deviates significantly from the predictions of the Fourier law, due to the boundary and interface scattering and the finite relaxation time of heat carriers [65]. To resolve this dilemma, the Cattaneo equation is used to account for the phenomena of heat propagation speed [66]. Recently, this equation has been applied across a thermoelectric thin film [67]. This wave type heat conduction equation, however, does not include the ballistic transport, which becomes significant as the characteristic length scales of a system are comparable to phonon mean free paths. Solution of the transient Boltzmann equations is required to describe the heat-conduction process in fast transient and Nano-scales. However, there exist inherent difficulties associated with the solution of the phonon BTE which makes it significantly limited the consideration of the transient and size effects in real engineering problems. This is due to the fact that the Boltzmann equation, even in its simplest form, is difficult to solve because it involves variables in both real and momentum spaces, as well as time.

Chen [68-69] derived the transient ballistic-diffusive heat conduction equations (BDE) from the phonon BTE under the relaxation time approximation. This approximation divides the heat flux into two components. One is contributed by the

excited and scattered carriers that are approximated as a diffusive transport process. The other originates from the boundaries and represents the ballistic nature of the transport. Advantage of the BDE over the Boltzmann equation is that only time and spatial coordinates are involved. Unlike the Cattaneo equation and the Fourier law, these equations capture both the nonlocal transport process and the time retardation, and thus can be applied to small structures and to fast heat-conduction processes.

In this work, we are interested in the study of energy and electric charge transport in thermoelectric materials at the nanometric length scale. This problem has attracted the attention of several researches [70], [71], [72] and [73] and excellent reviews have been reported [74], [75] and [76]. In [70] the authors were concerned with the assumptions made in the transport in silicon devices and their application in the case of small systems was critically examined. A small-size and column-type thermoelectric cooler was considered in [71]. It was analysed how the thermal and electrical transport through the interface between the thermoelectric element and metal connector is affected by the interface thickness. Its effect on the performance of the device was also investigated. In another study [72] the focus was on the effect of the Seebeck coefficient and the electrical conductivity on the performance of a micro thermoelectric cooler. Finally, in [73] it was proposed a set of non-local transport equations for the heat flux and electric current in nanowires including thermoelectric effects. It was obtained a dependence of the figure of merit on the transversal radius of the nanowire and some other parameters. The authors showed how to improve the figure of merit by controlling such parameters.

In this thesis, the transient ballistic-diffusive heat conduction equations (BDE),as an approximation to the phonon Boltzmann equation (BTE), and the hyperbolic heat equation (HHC) with constant and effective thermal conductivities are solved numerically and applied to the problem of transient heat conduction across thin films. Both the diffusive part of the BDE and HHC are solved with a stable and convergent finite difference method. The ballistic part of the BDE is solved with the Gauss-Legendre integration scheme. Finally, these equations are applied across a thermoelectric thin film to investigate the steady-state and the transient cooling mechanism at the cold side boundary. This is still on-going project and in the future the transient ballistic-diffusive heat conduction equations (BDE) will be applied to the nanoparticles moving inside thermal spray torches.

3 Modelling of High Velocity Suspension Flame Spraying

Description of a theoretical model for the HVSFS process is complex, because it involves turbulence mixing, combustion, compressible flow, subsonic/supersonic transition, multiphase interactions, including breakup, evaporation and combustion of solvent which can lead to cooling effect in the spray torch. Numerical modelling has become an important tool in the study of thermal spray systems. A well-developed model can provide insight into the underlying physics of the process by overcoming the technical constrains imposed by experiments. In this chapter HVSFS thermal spray system is computationally investigated in order to make a scientific assessment of the liquid droplet behaviour on injection. This includes modelling and analysis of premixed (propane/oxygen) combustion and gas flow dynamics of HVSFS process, modelling of secondary non-premixed (ethanol/oxygen) combustion, analysis of the interaction mechanism between gas and liquid droplet including fragmentation (secondary break-up), vaporization and finally analysis of the droplet injection point (axially, transversely, and externally), at the example of an industrial DJ2700 torch (Sulzer-Metco,Wohlen, Switzerland). The models are giving a detailed description of the relevant set of parameters and suggest a set of optimum spray conditions serving as a fundamental reference to further develop the technology.

3.1 Model Development

A schematic diagram and computational domain of the working DJ2700 gun is illustrated in Figure 3.1 highlighting the fuel-oxygen inlet, the combustion chamber, the convergent-divergent (CD) nozzle, and barrel. Premixed propane and oxygen are injected into the combustion chamber through surface of the annular inlet holes (as this is a 2D model), where the fuel burns and the combustion products are accelerated down through the convergent-divergent nozzle and the long parallel-sized barrel. The coating material in the form of particles of size 30 to 200 nm, which is dispersed in

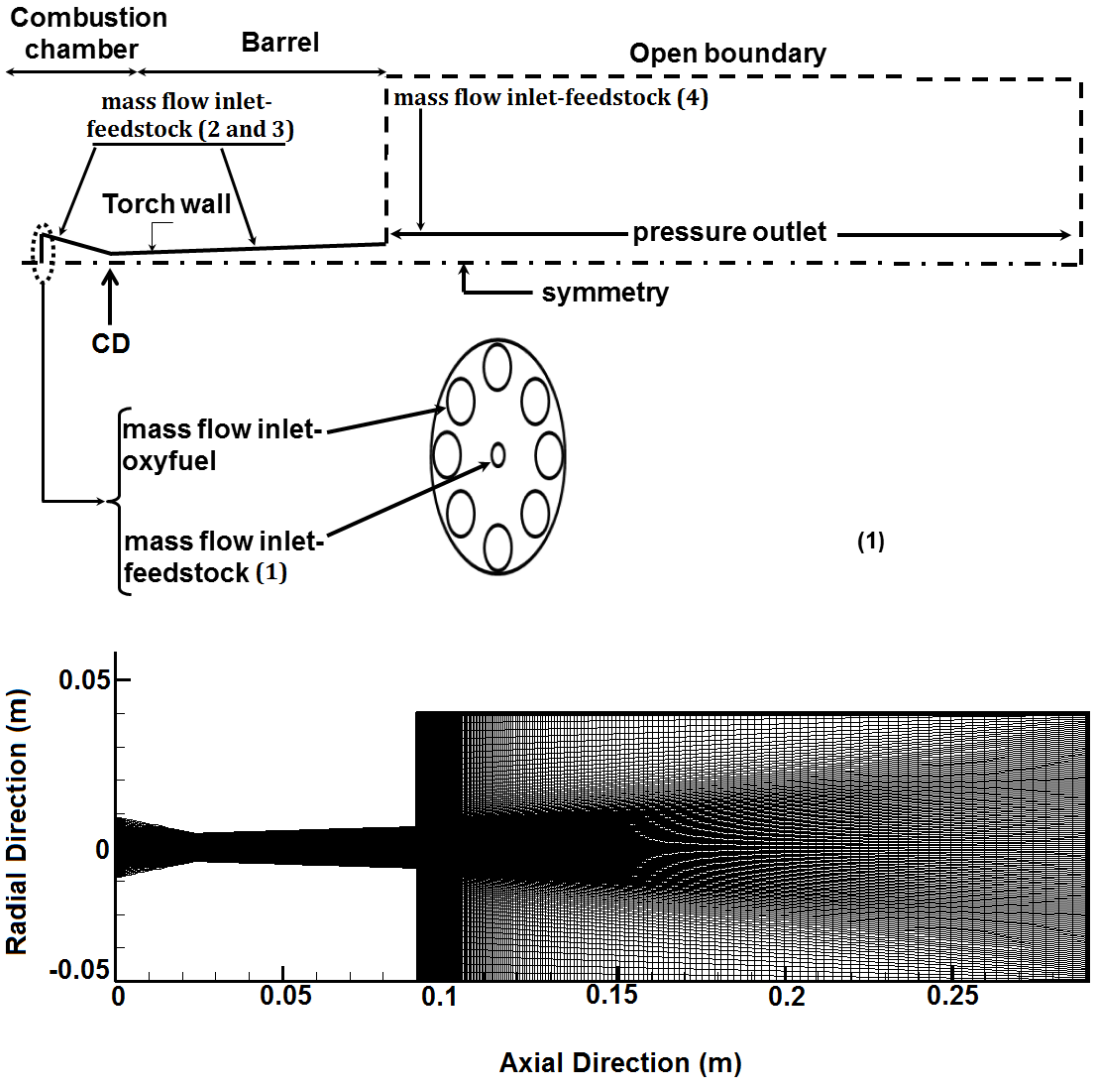

Figure 3-1: Schematic diagram and computational domain of the DJ2700 HVSFS thermal spray system

organic solvent (ethanol), is injected into the main gas flow. The suspension spray then travels in the high temperature flow region, and its liquid part, evaporates and combusts along its trajectory. The remaining solid part of the spray which usually appears as fine agglomerates of Nano-particles is accelerated and deposited on a substrate. The homogeneous liquid ethanol droplets are injected axially, transversely, and externally through an inlet as depicted in Figure 3.1. For barrel and external positions, droplets are injected vertically. The geometric parameters and working conditions for the simulation are summarized in Table 3.1. The commercial Finite volume code FLUENT 13 is used to model an unsteady compressible gas flow with discrete phase particles [116]. The inlet and exterior regions are modelled using pres-

Geometric Parameter (mm)	
Combustion chamber length	23.8
Combustion chamber radius	9.1
Nozzle throat radius	4.2
Barrel length	66.2
Barrel exit radius	6.22
Free jet length	200
Working Conditions	
Fuel Flow rate (propane)	0.003526 kg/s, Temperature: 300 K
Oxygen Flow rate	0.01197 kg/s, Temperature: 300 K
Atm. Pressure	101325 Pa, Temperature: 300 K
Wall boundary Temp.	Temperature: 300 K, Nonslip

Table 3-1: Summary of geometric parameters and working conditions for the DJ2700 HVOF thermal spray system

sure boundaries. A non-slip condition is applied at the nozzle wall surface, which is also treated as adiabatic. To avoid strong coupling between the pressure and velocity the pressure-based segregated solution algorithm [77] is applied, whereby the solution variables (velocity components, pressure, temperature, turbulence scalars) are solved one after another. The velocity and pressure are coupled using the semi-implicit method for pressure linked equations (SIMPLE) algorithm [78-79], which obtains an estimate of the pressure field using a guess and correct procedure. The transport equations are discretized using the Quick scheme. A description of the realizable k-ε turbulence model, applied for this investigation is given in the section 3.4. The discrete phase particle history is computed in a Lagrangian reference frame by coupling the properties of the fluid at the cell in which the particle resides with those of the instantaneous particle properties using the Discrete Phase Model (DPM).

The HVSFS gun has an axisymmetric design and a 2D model is adopted to decrease the complexity and computational time. The discrete ethanol droplets are the focus of this study, and are injected as single droplets to make particular assessment

of individual droplet behaviour. The discrete phase (droplets) and the continuous gas phase are coupled to each other (two-way coupling). Thus, while the continuous phase impacts the discrete phase, the effect of the discrete phase trajectories on the continuum phase is, also, incorporated. This two-way coupling is accomplished by alternately solving the discrete and continuous phase equations until the solutions in both phases have stopped changing.

The unsteady flow field of the continuous gas is calculated using the Reynolds averaged Navier-Stokes equations (RANS) and is assumed to behave as a compressible, ideal gas. The absolute pressure is equal to the sum of the static pressure of the flow and the continuity conservation equation operating pressure. To take into account the mass fraction of each species in the flow, the variable density is calculated as:

$$\rho = \frac{p+p_{op}}{RT\sum_i \frac{Y_i}{M_{\omega,I}}} \tag{3.1}$$

where p_{op} is the operating pressure, p is the local static pressure relative to the operating pressure, R is the universal gas constant, $M_{\omega,I}$ is the molecular weight, and Y_i local mass fraction of each species. The temperature, T, will be computed from the energy equation.

- the continuity conservation equation

$$\frac{\partial \rho}{\partial t} + \frac{\partial}{\partial x}(\rho v_x) + \frac{\partial}{\partial r}(\rho v_r) + \frac{\rho v_r}{r} = S_m \tag{3.2}$$

where x is the axial coordinate, r is the radial coordinate, v_x is the axial velocity, and v_r is the radial velocity. The source term S_m is the additional mass contribution from the vaporizing ethanol fuel droplets.

- the axial and radial momentum conservation equations

$$\frac{\partial}{\partial t}(\rho v_x) + \frac{1}{r}\frac{\partial}{\partial x}(r\rho v_x v_x) + \frac{1}{r}\frac{\partial}{\partial r}(r\rho v_r v_x) = -\frac{\partial p}{\partial x} + \frac{1}{r}\frac{\partial}{\partial x}\left[r\mu_{eff}\left(2\frac{\partial v_x}{\partial x} - \frac{2}{3}(\nabla.\vec{v})\right)\right] + \frac{1}{r}\frac{\partial}{\partial r}\left[r\mu_{eff}\left(\frac{\partial v_x}{\partial r} + \frac{\partial v_r}{\partial x}\right)\right] + F_x \tag{3.3}$$

$$\frac{\partial}{\partial t}(\rho v_r) + \frac{1}{r}\frac{\partial}{\partial x}(r\rho v_x v_r) + \frac{1}{r}\frac{\partial}{\partial r}(r\rho v_r v_r) = -\frac{\partial p}{\partial r} + \frac{1}{r}\frac{\partial}{\partial x}\left[r\mu_{eff}\left(\frac{\partial v_r}{\partial x} + \frac{\partial v_x}{\partial r}\right)\right] + \frac{1}{r}\frac{\partial}{\partial r}\left[r\mu_{eff}\left(2\frac{\partial v_r}{\partial r} - \frac{2}{3}(\nabla.\vec{v})\right)\right] - 2\mu_{eff}\frac{v_r}{r^2} + \frac{2}{3}\frac{\mu_{eff}}{r}(\nabla.\vec{v}) + F_r \quad (3.4)$$

where,

$$\nabla.\vec{v} = \frac{\partial v_x}{\partial x} + \frac{\partial v_r}{\partial r} + \frac{v_r}{r} \quad (3.5)$$

The effective viscosity, μ_{eff}, is represented by the sum of the artificial turbulent viscosity and the physical dynamic viscosity, which is employed to account for the enhanced mixing due to turbulent fluctuations within the mean flow. The axial and radial sources F_x and F_r are the body forces which arise from interaction with the dispersed ethanol fuel droplets. The momentum equations are Favre averaged as the flow is considered to be compressible.

- the energy conservation equation

$$\frac{\partial}{\partial t}(\rho E) + \frac{\partial}{\partial x}[v_x(\rho E + p)] + \frac{\partial}{\partial r}[v_r(\rho E + p)] = \frac{\partial}{\partial x}\left(v_x\sigma_{xx} + v_r\tau_{xr} + K_{eff}\frac{\partial T}{\partial x}\right) + \frac{\partial}{\partial x}\left(v_x\tau_{xr} + v_r\sigma_{rr} + K_{eff}\frac{\partial T}{\partial r}\right) + S_h \quad (3.6)$$

where,

$$\tau_{xr} = \tau_{rx=}\mu_{eff}\left(\frac{\partial v_x}{\partial r} + \frac{\partial v_r}{\partial x}\right) \quad (3.7)$$

$$\sigma_{rr} = 2\mu_{eff}\frac{\partial v_r}{\partial r} - \frac{2}{3}\mu_{eff}(\nabla.\vec{v}) \quad (3.8)$$

$$\sigma_{xx} = 2\mu_{eff}\frac{\partial v_x}{\partial x} - \frac{2}{3}\mu_{eff}(\nabla.\vec{v}) \quad (3.9)$$

The conservation of mass and momentum equations are linked to the energy conservation equation through the multispecies ideal gas law (Equation 3.1). The energy dissipated and received by the gas phase during the evaporation and combustion of the ethanol fuel droplets is represented by S_h.

3.2 Model Grid and Computational Domain

A structured grid is adopted in this study due to the following reasons: i) optimisation of computing cost; ii) a relatively simple geometry; iii) easy generation of fine local grid by varying nodal point; iv) effective convergence control at higher order discretization schemes. The gun and external free jet region are the computational domain of this axisymmetric flow (Figure 3.1). The mesh within the gun consists of 70 axial nodes, 30 radial nodes in the combustion chamber, and 170 and 200 axial nodes are present for the CD nozzle and barrel respectively. The external domain covers a practical stand of distance of 300 mm from the nozzle exit in axial direction, with 27,000 cells. The grid around the nozzle entrance and exit, the barrel exit and the free-jet centreline has been successively refined with various aspect ratios. This is due to fact that in these areas high gradients are expected due to steep variations in flow properties, therefore, great accuracy is required in order to accurately capture the effects of compressibility. External pressure boundary is applied to the atmospheric pressure and ambient temperature of 300 K, where the gas exhausts from the gun to air. The interior surfaces of the gun are defined as no-slip wall with a constant temperature 300 K.

3.3 Numerical Schemes

The numerical scheme applied in this study is a segregated solution algorithm [77] with a control volume-based technique. This numerical method is selected over the alternative approach of strong coupling between the velocities and pressure in order to avoid oscillations in the pressure and velocity fields and aid convergence. This approach is comprised of integrating of the conservation equation of continuity, momentum, energy, species, and turbulence on the individual cells with the computational domain to make algebraic equations for each unknown dependent variable. The SIMPLE (semi-implicit method for pressure linked equations) algorithm [78-79] is used to link the pressure and velocity fields as it is more stable and computationally economical in comparison with other schemes.

The QUICK (quadratic upwind interpolation) scheme [26] is employed to discretize the transport equations. The QUICK method is a higher order scheme and can minimize false diffusion errors but it is less computationally stable. In contrast,

although a first/second order upwind scheme gives stability for the discretization of the pressure-correction equation and is always bounded; if the flow is not aligned with the grid lines the upwind scheme will produce erroneous results. A comparison of these schemes is well discussed in [35].

3.4 Turbulence Model

It is possible to subdivide the entire turbulence models in three main groups: the so called first order closure (algebraic, one equation and multiple equations), second order closure (Reynolds-stress model, RSM) and Large eddy simulation (LES). The closure is the main drawback of statistical description: the equations derived for this method contain some additional terms so they need to be modelled. The first order closure models are based on the linear eddy viscosity hypothesis introduced by Boussinesq or the non linear extension proposed by Lumley. Boussinesq hypothesis is not generally valid. It is not accurate in cases like sudden variation in the mean strain rate, secondary flows, separated flow, rotating and stratified flows. The limit of this approach relies on the assumptions of local equilibrium between turbulence and main strain and of system rotation independence.

RSM models employ the exact equations for the Reynolds-stresses while the closure is necessary for higher order correlation terms. Those two classes of model belong to a more general approach, called RANS (Reynolds Averaged Navier Stokes equations). The most used 2 equations model is the $k-\varepsilon$ and a detailed description can be found in [80]. It relies on the solution of two additional transport equations, one for the turbulent kinetic energy k and the other for its dissipation rate ε. Finally the Large Eddy Simulation solves the large structure (vortex with high energy content) while model the influence of small structure (based on the observation they have more homogeneous and universal character).

The standard $k-\varepsilon$ model [80] can be used to compute a wide variety of flow problems, which is based on the presumption that the flow is fully turbulent and the turbulent viscosity of the flow is isotropic. However, the standard $k-\varepsilon$ model gives inaccurate predictions for complex flows due to turbulent-viscosity hypothesis which originate within the equation of turbulence dissipation. Thus, a modified transport equation is adopted to describe the rate of turbulence dissipation in the realizable $K-\varepsilon$ model [81]. The transport equations for the realizable $K-\varepsilon$ model are:

- turbulent kinetic transport equations

$$\frac{\partial}{\partial t}(\rho k)+\frac{\partial}{\partial x}(r\rho k v_x)+\frac{\partial}{\partial r}(r\rho k v_r)=\frac{\partial}{\partial x}\left(r\left(\mu+\frac{\mu_t}{\sigma_k}\right)\frac{\partial k}{\partial x}\right)+\frac{\partial}{\partial r}\left(r\left(\mu+\frac{\mu_t}{\sigma_k}\right)\frac{\partial k}{\partial r}\right)$$
$$+r(G_k+G_b-\rho\varepsilon-Y_M) \quad (3.10)$$

- rate of dissipation of energy from the turbulent flow

$$\frac{\partial}{\partial t}(\rho\varepsilon)+\frac{\partial}{\partial x}(r\rho\varepsilon v_x)+\frac{\partial}{\partial r}(r\rho\varepsilon v_r)=\frac{\partial}{\partial x}\left(r\left(\mu+\frac{\mu_t}{\sigma_\varepsilon}\right)\frac{\partial\varepsilon}{\partial x}\right)+\frac{\partial}{\partial r}\left(r\left(\mu+\frac{\mu_t}{\sigma_\varepsilon}\right)\frac{\partial\varepsilon}{\partial r}\right)$$
$$+r\left(\rho C_1 S\varepsilon-\rho C_2\frac{\varepsilon^2}{k+\sqrt{v\varepsilon}}+\rho C_{1\varepsilon}\frac{\varepsilon}{k}C_{2\varepsilon}G_b\right) \quad (3.11)$$

where the turbulent viscosity and its coefficient of dynamic viscosity, respectively, are:

$$\mu_t=\rho C_\mu\frac{K^2}{\varepsilon} \quad (3.12)$$

$$C_\mu=\frac{1}{A_0+A_s(kU^*/\varepsilon)} \quad (3.13)$$

where

$$U^*=\sqrt{S_{ij}S_{ij}} \quad (3.14)$$

with the mean strain rate S_{ij} is defined by:

$$S_{ij}=\frac{1}{2}\left(\frac{\partial u_j}{\partial x_i}+\frac{\partial u_i}{\partial x_j}\right) \quad (3.15)$$

The model constants A_0 and A_s are given by:

$$A_0=4.04,\quad A_s=\sqrt{6}cos\emptyset \quad (3.16)$$

$$\emptyset=\frac{1}{3}cos^{-1}(\sqrt{6}W),\quad W=\frac{S_{ij}S_{jk}S_{ki}}{\tilde{S}^3},\quad \tilde{S}=\sqrt{S_{ij}S_{ij}} \quad (3.17)$$

It can be seen that C_μ is a function of the mean strain and the turbulence fields (K and ε). This model is physically more complete as it considers the requirement of a more complete description of the normal stresses. In this new formulation, C_μ is made variable in relation to the turbulence and the mean flow to satisfy the requirement of normal stress being positive by definition. Then the turbulent viscosity μ_t is estimated

by direct values of C_μ. Background information about the turbulence-compressible flow can be found in the appendix of this thesis.

3.5 Combustion Model

The propane gas fuel C_3H_8 is used to represent the average size of the propane hydrocarbon chain in this study. Carbon dioxide and water can be regarded as the end products of propane combustion in an ideal reaction at stoichiometric ratio.

$$C_3H_8 + 5O_2 \rightarrow 3CO_2 + 4H_2O \tag{3.18}$$

However, CO_2 and H_2O will dissociate into a number of species with light molecular weight when temperature is in excess of 2000 K and this is because of strong thermal atomic vibration. In this study an equilibrium formulation is considered in order to take into account the effects of dissociations and intermediate reactions:

$$n_1C_3H_8 + n_2O_2 \rightarrow n_3CO_2 + n_4H_2O + n_5CO + n_6OH + n_7O_2 + n_8O + n_9H_2 + n_{10}H \tag{3.19}$$

The eddy dissipation model [82] is employed to solve this combustion reaction. This model is based on a turbulence-chemistry interaction model. The net rate of production of species *i* due to reaction *r*, $R_{i,r}$, is given by the smaller (that is, limiting value) of the two expressions below:

$$R_{i,r} = v'_{i,r} M_{\omega,i} A \rho \frac{\varepsilon}{K} min_R \left(\frac{Y_R}{v'_{R,r} M_{\omega,R}} \right) \tag{3.20}$$

$$R_{i,r} = v'_{i,r} M_{\omega,i} AB \rho \frac{\varepsilon}{K} \left(\frac{\sum_P Y_P}{\sum_J^N v''_{j,r} M_{\omega,j}} \right) \tag{3.21}$$

In Equations 3.20 and 3.21, the chemical reaction rate is governed by the large eddy mixing time scale, $\frac{K}{\varepsilon}$, where combustion proceeds whenever turbulence is present $\left(\frac{K}{\varepsilon} > 0\right)$.

There are two more combustion models, namely the laminar finite rate model which computes the chemical source terms using the Arrhenius expressions without the effects of turbulent fluctuations, and the finite rate eddy dissipation model which

computes both the Arrhenius rate and mixing rate, and uses the smaller of the two with the effects of turbulence. These models are in detail compared in [35].

3.6 Modelling of Discrete Phase Liquid Droplet

The ethanol droplets after being injected into the HVSFS flame jet undergo several processes taking place simultaneously. The first is the aerodynamic break-up as the slowly moving droplets are entrained into the high velocity jet and as they accelerate in the high velocity gas stream. Depending on their size and thermo-physical properties of the liquid and the surrounding gas, droplets can undergo severe deformation and eventually break up into smaller droplets. To have a good understanding of the liquid spraying process, it is of fundamental importance to examine the physical break-up process instead of correlating the gas dynamics with droplet fragmentation indirectly. Although this study is intended to shed light on the importance of ethanol atomization process, the resulted droplet diameter distribution prior to injection are out of scope of this thesis (primary break-up). The history of suspension droplets is computed with a Lagrangian formulation where the finite inter-phase transport rates and effects of turbulence interactions between the droplet and gas phases are considered. By using this treatment the evaporation history and temperature change for droplets can be calculated during the second process of heat exchange between the gaseous and liquid phases. The third process is the two phase combustion where ethanol vapours chemically react with the remaining oxygen from the primary propane-oxygen combustion. Finally, the subsequent gas flow pattern is detailed from the coupled set of equations described in the following section.

The conditions under which each droplet has a set of equations are:

1. The liquid droplet and gas phases have their own initial continuous velocity and temperature and co-exist at each location,
2. Liquid phase has its own turbulent fluctuations that result in turbulent droplet transport of mass, momentum and energy. The random effects of turbulence on the particle motion are counted by integrating the individual particle trajectory with the instantaneous fluid velocity,
3. The dissolved powder content is not included in this thesis and will be examined in future. Although, the rate of evaporation and break of

homogeneous ethanol spray might be different from the evaporation of suspension spray, it is assumed that the nano-particle loading is relatively low for this particular process.

The first part of model simulates the temperature and velocity fields of an HVSFS flame jet. The realizable *k*- ε model was used for modelling the turbulence in the jet, including compressibility effects. Both pre-mixed (oxygen-propane) and non-premixed (oxygen-ethanol) were solved by eddy dissipation model with hyper-stoichiometric oxygen mass fraction. Having solved the gas phase, the injection of liquid ethanol droplets into the high pressure combustion chamber is modelled by a discrete phase model. Since the Ohnesorge number remains very below 0.1 ($Oh \ll 0.1$) in the computational domain, the main parameter related to break up physics is the Weber number. The secondary breakup of droplets to smaller ones was modelled by Taylor Analysis Breakup (TAB) model for axial injections (Weber number<100) and wave model for radial injections (Weber number>100). Finally, the droplets heat and mass transfer with continuous phase were modelled based on three laws which will be described in detail in the following section.

3.6.1 Heat, Mass, and Momentum Transport

The Lagrangian discrete phase model follows the Euler-Lagrange approach, where the dispersed phase is solved by tracking injected droplets through the calculated flow field. The trajectory of a discrete phase droplet is calculated by integrating the force balance on the droplet. The forces acting on the droplet can be force due to pressure gradient and added mass, Basset history term, external potential forces and drag force. However, the major acting force on the droplet during the HVSFS/HVOF spraying process is the drag force and other forces can be neglected [14]. Hence, the equation of droplet motion for this process is described as:

$$\frac{du_d}{dt} = F_D(u_g - u_d) \tag{3.22}$$

Where u_g is gas phase velocity and u_d is droplet velocity. F_D is the drag force and can be expressed as follows:

$$F_D = \frac{18\mu_g}{\rho_d d_d^2}\frac{C_D Re}{24} \tag{3.23}$$

Where μ_g is gas viscosity. d_d and ρ_d are droplet diameter and density respectively.

For non-spherical droplets Haider and Levenspiel [83] developed the following correlation. Drag coefficient is different for smooth droplets.

$$C_D = \frac{24}{Re_d}\left(1 + b_1 Re_d^{b_2}\right) + \frac{b_3 Re_d}{b_4 + Re_d} \tag{3.24}$$

$$b_1 = exp(2.3288 - 6.4581\emptyset + 2.4486\emptyset^2) \tag{3.25}$$

$$b_2 = 0.0964 + 0.5565\emptyset \tag{3.26}$$

$$b_3 = exp(4.905 - 13.8944\emptyset + 18.4222\emptyset^2 - 10.2599\emptyset^3) \tag{3.27}$$

$$b_4 = exp(1.4681 + 12.2584\emptyset - 20.7322\emptyset^2 + 15.8855\emptyset^3) \tag{3.28}$$

The shape factor, $\emptyset$, and the Reynolds number, Re, are defined as:

$$\emptyset = \frac{s}{S} \tag{3.29}$$

$$Re = \frac{\rho_g |u_g - u_d| d_d}{\mu_g} \tag{3.30}$$

where s is the surface area of a sphere having the same volume as the droplet, and S is the actual surface area of the particle.

Droplets heat and mass transfer with continuous phase are modelled based on three laws and at each tracking time relevant law is applied based on droplet conditions. The inert heating (law 1) is applied when the droplet temperature is less than the vaporization temperature, T_{vap}, which is an arbitrary modeling constant used to define the onset of vaporization/boiling laws and has got no physical significance. T_{vap} is 271 K for liquid ethanol.

Law 1:

$$T_d < T_{vap}$$

When using law 1, a simple heat balance (Equation 3.31) is used to relate the droplet temperature, T_d, to the convective heat transfer and the heat gained or lost by the droplets as it traverses each computational cell appears as a source or sink of heat in subsequent calculations of the continuous phase energy equation. During law 1, droplets do not exchange mass with continuous phase and do not participate in any chemical reaction.

$$m_d c_d \frac{dT_d}{dt} = hA_d(T_\infty - T_d) \tag{3.31}$$

Equation 3.31 assumes the droplet is at uniform temperature, that is, there is negligible internal resistance to heat transfer. The heat transfer coefficient, h, is calculated using the Ranz-Marshall correlation [84-85]:

$$Nu = \frac{hd_d}{K_\infty} = 2.0 + 0.6Re_d^{1/2}Pr^{1/3} \tag{3.32}$$

Law 2 is applied to predict the vaporization from a discrete phase droplet. Law 2 is initiated when droplet temperature reaches the vaporization temperature, T_{vap}, and continues until the droplet reaches the boiling point (boiling temperature).

Law 2:

$$T_{vap} \leq T_d < T_{boil}$$

During law 2, the rate of evaporation is determined by gradient diffusion, with the flux of droplet vapour into the gas phase related to the difference in vapour concentration at the droplet surface and the bulk gas:

$$N_i = k_c\left(C_{i,s} - C_{i,\infty}\right) \tag{3.33}$$

The concentration of vapour at the droplet surface is evaluated by assuming that the partial pressure of vapour at the interface is equal to saturated vapour pressure, P_{sat}, which is combination of gas pressure and recoil pressure of evaporated material, at the droplet temperature, T_d:

$$C_{i,s} = \frac{P_{sat}(T_d)}{RT_d} \tag{3.34}$$

Saturation vapour pressure is defined as a piecewise linear function of temperature and added to solver. The concentration of vapour in the bulk gas is known from solution of the transport equation for species *i* as:

$$C_{i,\infty} = x_i \frac{p}{RT_\infty} \tag{3.35}$$

The mass transfer coefficient, k_c, in Equation 3.33 is calculated from the Sherwood number correlation:

$$Sh = \frac{k_c d_d}{D_{i,m}} = 2 + 0.6Re_d^{0.5}Sc^{1/3} \tag{3.36}$$

where $D_{i,m}$ is diffusion coefficient of vapour in the bulk. Sc is the Schmidt number and defined as:

$$Sc = \frac{\mu}{\rho D_{i,m}} \tag{3.37}$$

The droplet mass is reduced according to

$$m_d(t + \Delta t) = m_d(t) - N_i A_d M_w \Delta t \tag{3.38}$$

The droplet temperature during heating and vaporization is updated according:

$$m_d c_d \frac{dT_d}{dt} = hA_d(T_\infty - T_d) - \frac{dm_d}{dt} h_{fg} \tag{3.39}$$

where h_{fg} is latent heat.

Law 3:

$$T_d \geq T_{boil}$$

During law 3, a boiling rate equation is applied [86]:

$$\frac{d(d_d)}{dt} = \frac{4K_\infty}{\rho_d \, c_{d,\infty} \, d_d}\left(1 + 0.23\sqrt{Re_d}\right) ln\left[1 + \frac{c_{d,\infty}(T_\infty - T_d)}{h_{fg}}\right] \tag{3.40}$$

The droplet is assumed to stay at constant temperature while the boiling rate is applied. Once the boiling law is entered is applied for the duration of the droplet trajectory. The energy required for vaporization appears as a negative source term in the energy equation for the gas phase. The evaporated liquid enters the gas phase as species i.

It should be noted droplet initial temperature is assumed to be 300 K. Once droplets are injected into the hot combustion chamber they start gradually evaporating and combusting with remnant oxygen left from pre-mixed propane/oxygen combustion. Additionally, the Knudsen number, ratio of gas mean free path, λ, to droplet diameter, d_d, is far less than the transition number 0.01 thereby non-continous effect is not considered in this study [38]. The gas Reynolds numbers are around 2.09×10^5 to 1.18×10^5 , varying in the computation domain based on the characteristics of the gas dynamics.

3.6.2 Breakup Model

The Weber number is defined as:

$$We = \frac{\rho_l u_{rel}^2 d_d}{\sigma} \tag{3.41}$$

In the above equation, u_{rel} is the relative velocity between the droplet and the gas phase and We is the droplet Weber number, a dimensionless parameter defined as the ratio of aerodynamic forces to surface tension forces.

The TAB model is based on an analogy between the oscillation of distorting droplets and a spring-mass system. The external force is represented by aerodynamic force while the restoring force of the spring is replaced by the surface tension. The damping forces are represented by the liquid viscosity. In this model, Breakup occurs and several smaller droplets are created when the oscillation of the parent droplet grows to a critical value. The distortion ratio is the criterion for droplet breakup. Assuming $y = x/C_b r$ the governing equation becomes:

$$\frac{d^2y}{dt^2} = \frac{C_F}{C_b}\frac{\rho_g}{\rho_l}\frac{u^2}{r_d^2} - \frac{C_k \sigma}{\rho_l r_d^3} y - \frac{C_d \mu_l}{\rho_l r_d^2}\frac{dy}{dt} \tag{3.42}$$

Breakup occurs for $y > 1$. The constants values are selected based on experiments and theory ($C_F = \frac{1}{3}, C_b = \frac{1}{2}, C_k = 8, C_d = 5$). The undamped oscillation amplitudes and droplet oscillation frequency are determined as follow:

$$A = \sqrt{(y^n - We_c)^2 + \left(\frac{(dy/dt)^n}{\omega}\right)^2} \tag{3.43}$$

$$\omega^2 = \frac{C_k \sigma}{\rho_l r_d^3} - \frac{1}{t_d^2} \tag{3.44}$$

The breakup is only possible if the following condition is met:

$$We_c + A > 1 \tag{3.45}$$

Displacement of the droplet equator from its spherical position is the distortion, which can be nondimensionalized by 0.5 times the radius of the droplet [87]. The minimum and maximum values for the nondimensionalized distortion are 0 and 1, respectively. The initial distortion of droplets is considered to be a low value ($y_0 = 0.1$), in this thesis, in order to facilitate the condition for the droplets to breakup or remain unbroken.

The wave model [88] considers the breakup of droplets to be created by the relative velocity between the liquid and gas phase. This model is based on the presumption that the resulting droplet sizes and the time of breakup are related to the fastest growing Kelvin-Helmholtz instabilities on the parent droplet. This means that

the wavelength of the fastest growing unstable surface wave on the parent droplet is proportional to the radius of the child droplet (Equation 3.46). The maximum growth rate, Ω, and the corresponding wavelength, Λ, are calculated by equations 3.47 and 3.48, respectively.

$$r_d = B_0 \Lambda \tag{3.46}$$

$$\Omega \sqrt{\frac{\rho_l a^3}{\sigma}} = \frac{\left(0.34+0.38We_2^{1.5}\right)}{(1+Oh)(1+1.4Ta^{0.6})} \tag{3.47}$$

$$\frac{\Lambda}{a} = 9.02 \frac{\left(1+0.45Oh^{0.5}\right)\left(1+0.4Ta^{0.7}\right)}{\left(1+0.8We_2^{1.67}\right)^{0.6}} \tag{3.48}$$

where B_0 is a model constant set equal to 0.61 [88]. The rate of change of droplet radius in the parent parcel is predicted by equation 3.45, where the breakup time, τ, is calculated by equation 3.46.

$$\frac{da}{dt} = -\frac{(a-r_d)}{\tau} \tag{3.49}$$

$$\tau = \frac{3.726 B_1 a}{\Lambda \Omega} \tag{3.50}$$

The breakup time constant, B_1, is set to a value of 1.73 [89].

3.7 Numerical Results and Discussion

Liquid ethanol droplet or suspension mass flow rate (amount of liquid mass per second injected into the gun), initial injection velocity, droplet size and location of the injection point are very important parameters governing the process and operating conditions in real experiments and industry. Therefore, this work explores effects of these parameters on the process in a wide range in order to suggest optimum values for experimental and industry uses. The values for each parameter are carefully selected after many numerical simulations in order to illustrate their impacts on the process. Some suspension feed rates (mass flow rate) used in experimental studies of HVSFS process are 0.86, 0.17, 0.33, 1.11 and 1.9 g/s. Moreover, Without DPM case in the text and figures refers to the case in which no droplets are injected into the gun and denotes the HVOF gas dynamics

This research work is based on and continues the numerical analysis of the conventional HVOF thermal spray process as described somewhere else [35-36, 90-91], where extensive validation of the combustion, discrete phase and flow and

turbulence models have been vigorously tested against experimental data in the open literature and have demonstrated accurate predictions.

3.7.1 Gas Flow Dynamics

The unsteady, compressible flow field through the HVSFS thermal spray system prior to injection of the discrete phase is calculated based on hyper-stoichiometric oxygen mass fraction and the conditions as listed in Table 3.1. The process is initialized by injecting pre-mixed gas propane and pure oxygen into the combustion chamber where they exothermically combust, creating a highly pressurized gaseous mixture at a maximum flame temperature of above 3200 K. The dissociated gas species CO_2, H_2O, CO, OH, O_2, O, H_2, and H exits the combustion chamber. The gas is rapidly accelerated at the convergent-divergent nozzle and its throat the flow is choked at Mach number 1. As the gas expands and accelerates through the divergent section two small discontinuities follow, marked by slight increases in velocity along the centreline. These flow dynamics are quantitatively described along the centreline by Figure 3.2 (a-c). Upon entering the flow into the barrel, a series of shock waves are developed on further expansion of supersonic flow and then becomes stabilized. The gas flow immediately expands upon entering the ambient environment and is accelerated up to Mach 2. The fluctuation in flow properties are created by a series of periodic flow compression and expansion, where several shock diamonds are captured. The pressure remains high within the combustion chamber, decreases sharply in the convergent-divergent nozzle and reaches near atmospheric level in the barrel.

3.7.2 Parameters Investigation on Axial Injection

3.7.2.1 Droplet Mass Flow Rate Effects

First the droplet mass flow rate effects were studied by considering 0.01, 0.1 and 1 g/s droplet mass flow rate with oxygen/ethanol equivalence ratio of 0.1, 5 and 630 injected axially into the gun respectively, while keeping constant the droplet size and velocity. These values for the mas flow rate are selected after many trial and error numerical calculations and based on commonly used values in experimental studies. In all three cases, the droplets were injected with a nominal initial velocity 15 m/s and size 50 μm. The initial droplet temperature was assumed to be 300 K. A comparison

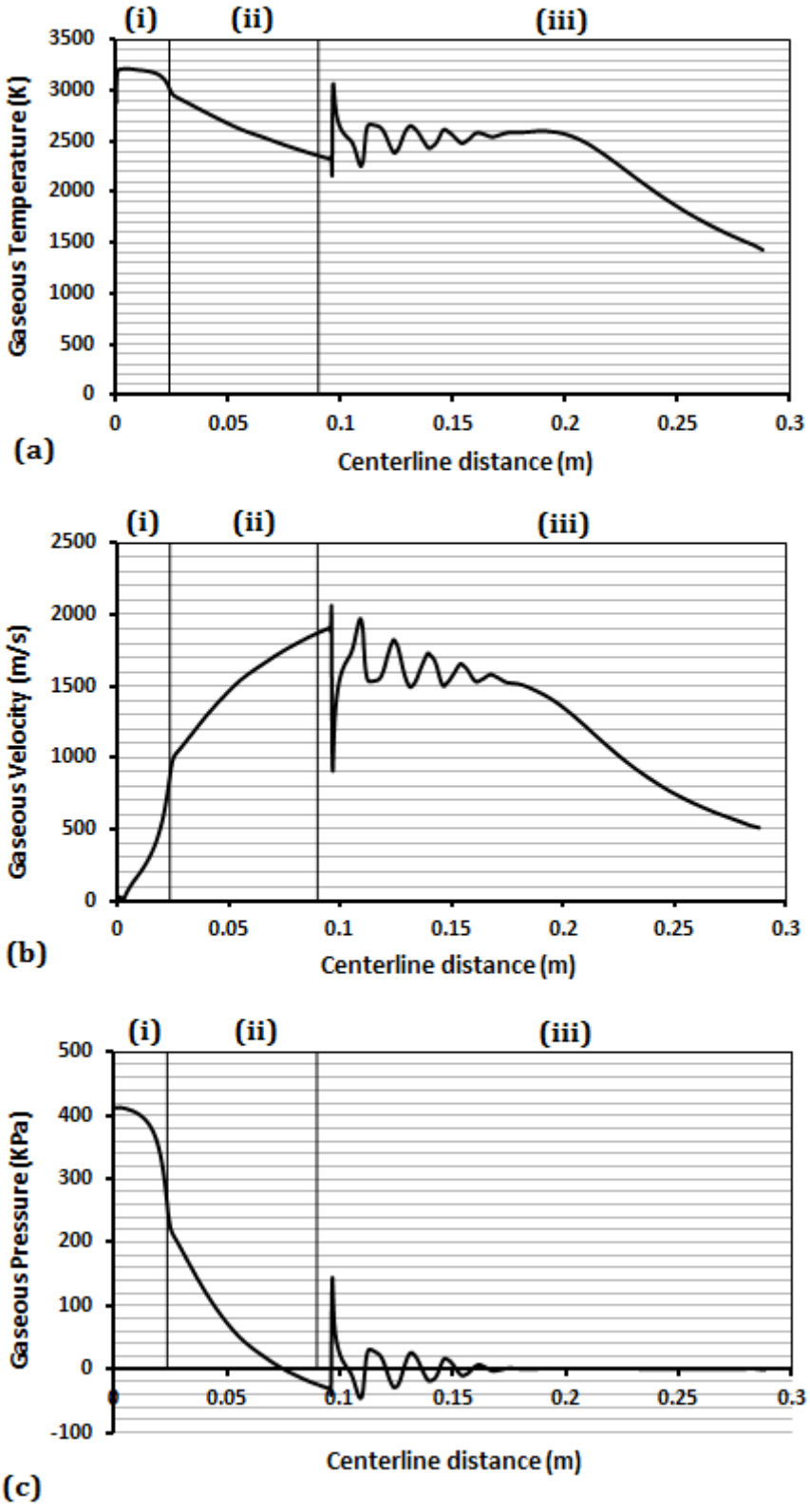

Figure 3-2: Variation in gaseous temperature (a), velocity (b), and pressure (c) along the centerline of the simulated HVSFS torch.

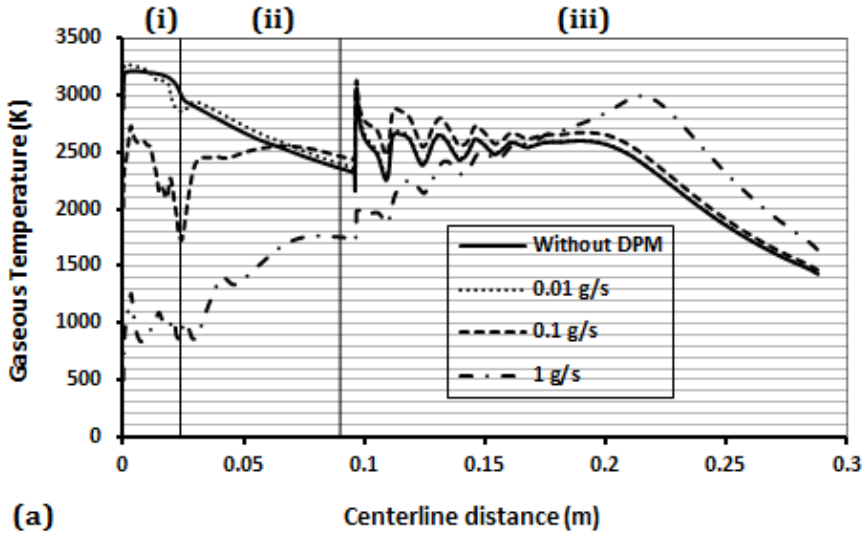

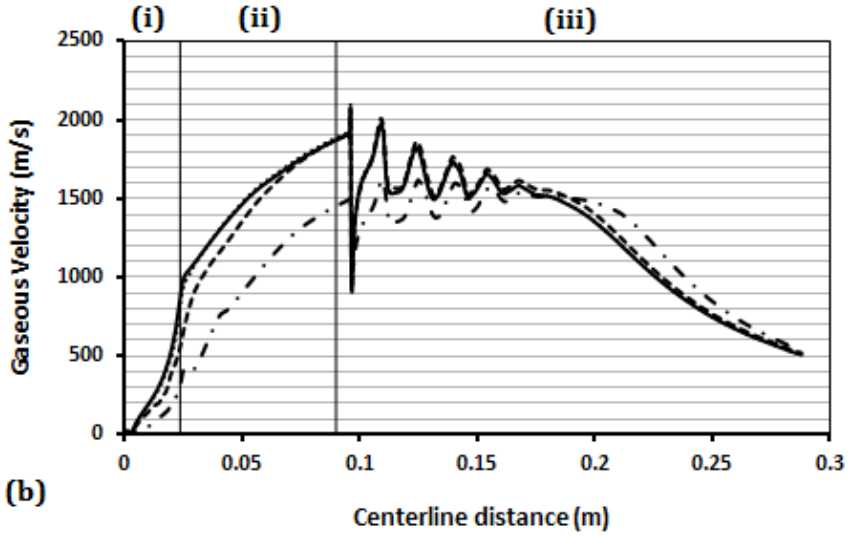

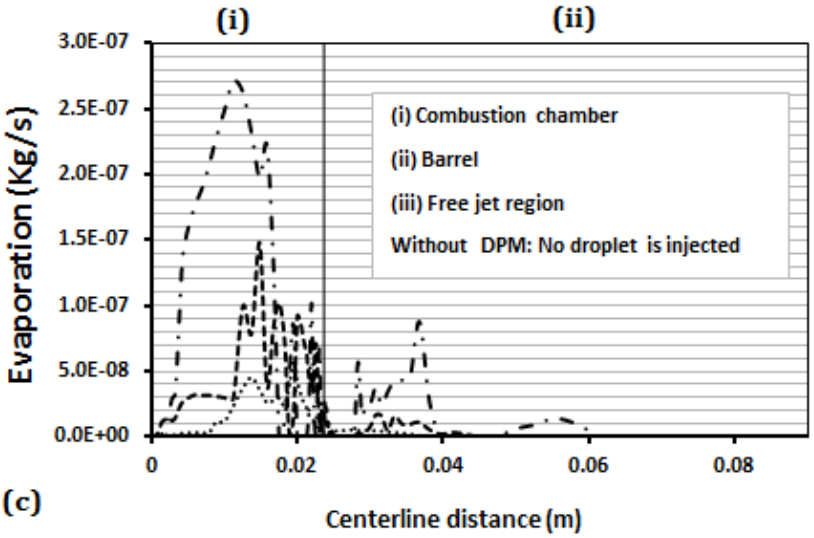

Figure 3-3: Comparison of (a) HVSFS temperature (b) velocity fields, and, (c) rate of evaporation experienced by droplets injected axially with 0.01, 0.1, 1 g/s initial mass flow rate

of the HVSFS temperatures, velocities and rate of evaporation experienced by these amounts of droplets along the centreline is shown in Figure 3.3 (a-c). Without DPM in the figures refers to a case in which droplets are not injected and it only shows flow characteristics in HVOF process. In cases where the droplets are injected with low mass flow rate 0.01 g/s, the gaseous temperature along the centreline does not experience considerable changes. Conversely, it decreases drastically near the combustion chamber back wall from approximately 3200 to 2000 and 500 K as droplet injected with mass flow rates 0.1 and 1 g/s respectively. Then it quickly rises to about 2700 K, but again sharply fall to 1700 K before the convergent-divergent nozzle, followed by gradual increase so that in the middle of the barrel exceeds the gas temperature to which droplets are not injected. Therefore, cooling occurs mainly inside the combustion chamber when droplets injected with mass flow rate of 0.1 g/s. However, as droplets injected with mass flow rate 1 g/s highly cool down the gas temperature which remains below 1300 and 1800 K inside the combustion chamber and barrel respectively and rise to almost 3000 K at far distance from gun exit. This is likely due to the fact that some droplets leave the torch and combust outside the gun increasing in this way the free jet gas temperature. Similarly, the velocity field remains almost unchanged as droplets injected with low mass flow rates. However, with higher mass injection it decreases from 1000 to 400 m/s and 1900 to 1500 m/s in the convergent-divergent nozzle and gun exit respectively.

Moreover, even though injecting higher liquid mass flow rate increases the rate of evaporation from 2.3×10^{-8} to 7×10^{-7} kg/s, Figure 3.3-c, as already discussed the more mass is injected the higher will be the cooling effect and it may transfer the location of evaporation area from combustion chamber to barrel which is not desirable. Thereby, since droplets with mass flow rates higher than 0.1 g/s cool down the flame temperature highly and results in less flow velocity, late investigation will be conducted by specifying 0.1 g/s mass flow rate for injected droplets.

3.7.2.2 Droplet Velocity Effects

Injection velocity is also considered to be one of the factors likely affecting the droplet heat up and evaporation in HVSFS process. In order to analyse the effects of injection velocity, three cases of axial injection are considered. For this investigation, droplet initial injection velocities 15, 30 and 50 m/s were selected. The initial droplet

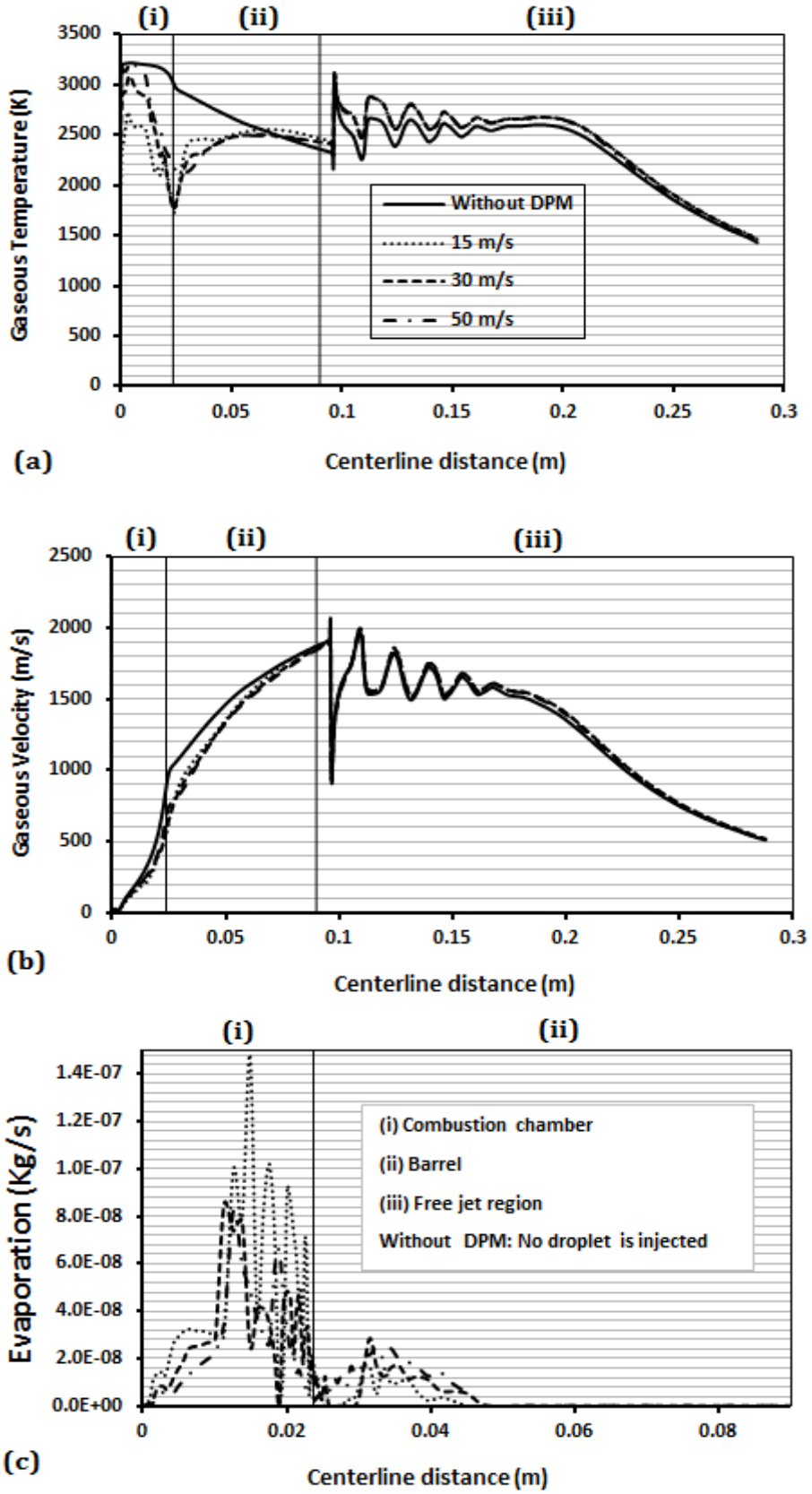

Figure 3-4: Comparison of (a) HVSFS temperature (b) velocity fields, and, (c) rate of evaporation experienced by droplets injected axially with 15, 30, 50 m/s velocity

size and mass flow rate were 50 µm and 0.1 g/s in all cases respectively. In Figure 3.4 (a-c), the HVSFS temperatures, velocities and rate of evaporation experienced by the droplets along the centreline are shown. HVSFS temperature shows less cooling in the immediate access of combustion chamber for the droplets that are injected at higher velocities. This is expected since residence time in the high temperature core of the HVSFS for droplets with higher initial velocities would be shorter, and these droplets would travel faster towards the cooler downstream regions. However, gas velocities in all three cases show similar trend with maximum loss of 250 m/s in convergent-divergent nozzle compared to Without DPM case. Moreover, it can be seen from Fig.3-c the rate of evaporation is highest in the middle of combustion chamber as droplets injected with initial velocity of 15 m/s but the location of evaporation moves towards the barrel with higher initial velocities. As a result, it can be concluded that droplets initial velocity does not affect highly the gas dynamics in HVSFS process as far as droplet initial mass flow rate is controlled.

3.7.2.3 Droplet Size Effects

Finally the droplets size effects were studied by considering 50, 150 and 300 µm initial size droplets injected into the HVSFS field axially. All of the droplets were injected with a nominal initial velocity and mass flow rate of 30 m/s and 0.1 g/s respectively. A comparison of the HVSFS temperatures, velocities and rate of evaporation experienced by these droplets is shown in Figure 3.5 (a-c). In all cases as droplets introduced into the combustion chamber, HVSFS temperatures witness dramatic decrease both before convergent-divergent nozzle and in barrel due to liquid ethanol phase change, then start rising almost in middle of barrel and reach the same level as of without DPM case. However, slightly higher cooling is observed as droplet size shrunk to 50 µm. Furthermore, maximum rates of evaporation are calculated to be 8×10^{-8}, 1.1×10^{-7} and 1.5×10^{-7} kg/s for droplets with initial size 50, 150 and 300 µm respectively.

Overall, HVSFS velocity fields are not disrupted with these droplet sizes because the optimum mass flow rate discovered from previous study is considered for droplet size analysis. For example, if more mass flow rate with droplet size of 300 µm is injected to the system, the higher will be the cooling effect and it will reduce flow velocity highly. The location of evaporation in all cases mainly occurs in combustion

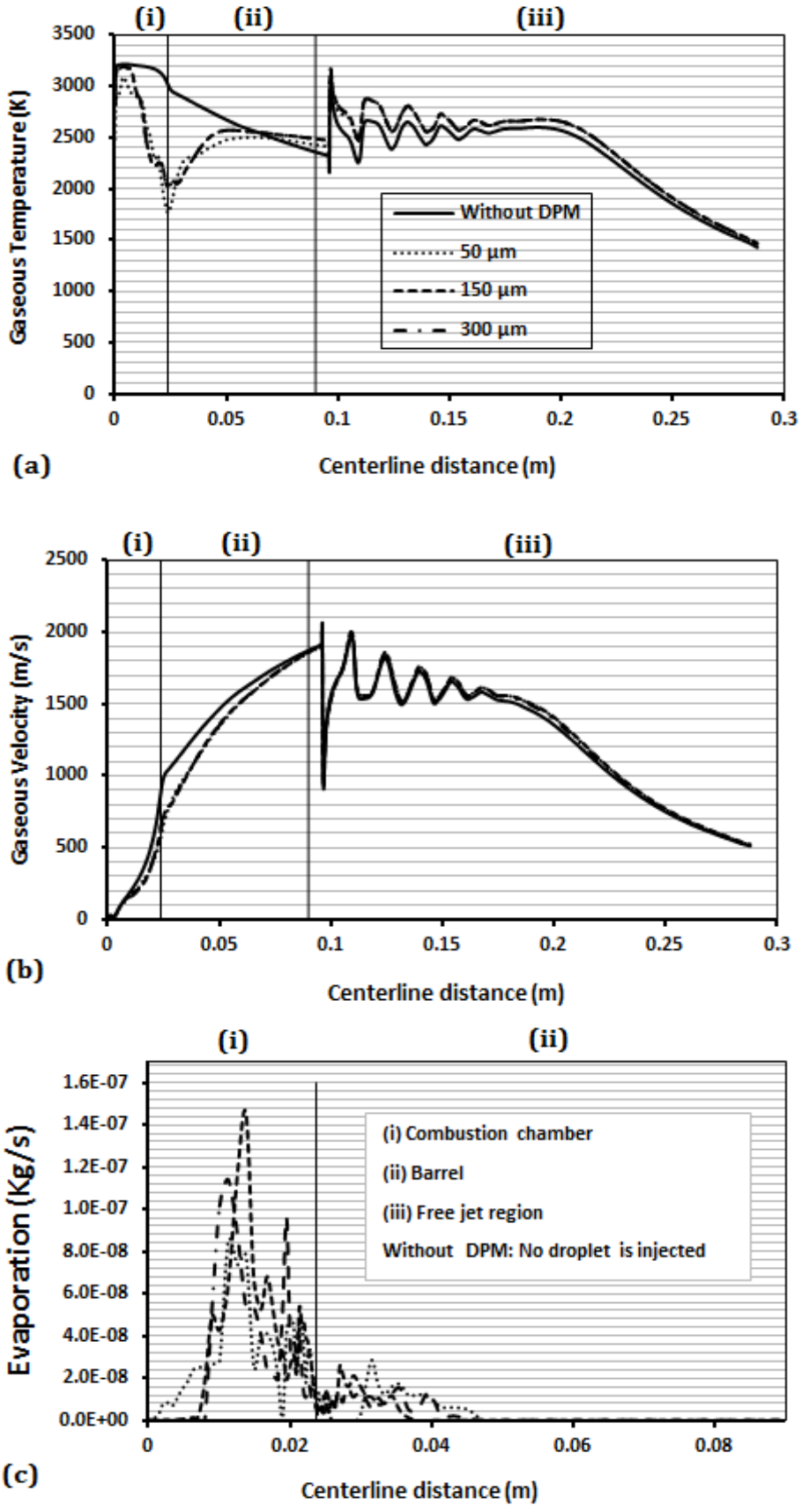

Figure 3-5: Comparison of (a) HVSFS temperature (b) velocity fields, and, (c) rate of evaporation experienced by 50, 150 and 300 µm droplets injected axially

chamber because, as discussed earlier, less mass is introduced to the gun with relatively low initial velocities. Thereby, from these three parametric studies can be concluded that the location of droplet evaporation and flame cooling can be adjusted by selecting the optimum liquid droplet mass flow rate and droplet size and applying required amount of velocity as such to give enough inertia for them to travel through the gun. However, among these parameters, only the amount of initial mass flow rate plays a crucial role in determining the overall performance of HVSFS gas dynamics.

3.7.3 Effects of Injection Location

In this radial injection scheme, the droplets are injected normally inward from three different positions namely: middle of combustion chamber (0.006, 0.008 m), middle of barrel (0.05, 0.005 m) and at a distance downstream from the barrel exit (0.12, 0.008 m) which is summarized in Table 3.2. The values inside braces show the coordinate specification of injection positions. In all three cases, droplets were inject-

Injection Location	Location Coordinates	
	X-Direction	Y-Direction
Combustion Chamber	0.006 m	0.008 m
Barrel	0.05 m	0.005 m
External	0.12 m	0.008 m

Table 3-2: Summary of radial injection location

ed at initial velocity of 45 m/s and initial temperature of 300 K. It should be noted droplets would immediately after injection stick the wall with initial velocities less 45 m/s and are not likely able to move toward the core area, thereby this amount of velocity is selected to appropriately investigate their evaporation, break up and their effects on HVSFS gas dynamics. Moreover, since droplets Weber number in the computational domain goes above 100 for radial injection scheme due to very high relative velocities between droplets and gas phase, wave model is used to solve droplets fragmentation.

A comparison of HVSFS temperatures and velocities experienced by these three different injection locations is shown in Figure 3.6 (a-b) which clearly shows that

droplets injected from barrel and outside the gun has got no effect on HVSFS temperature and velocity along the centreline. As can be seen from Figure 3.7 (b and

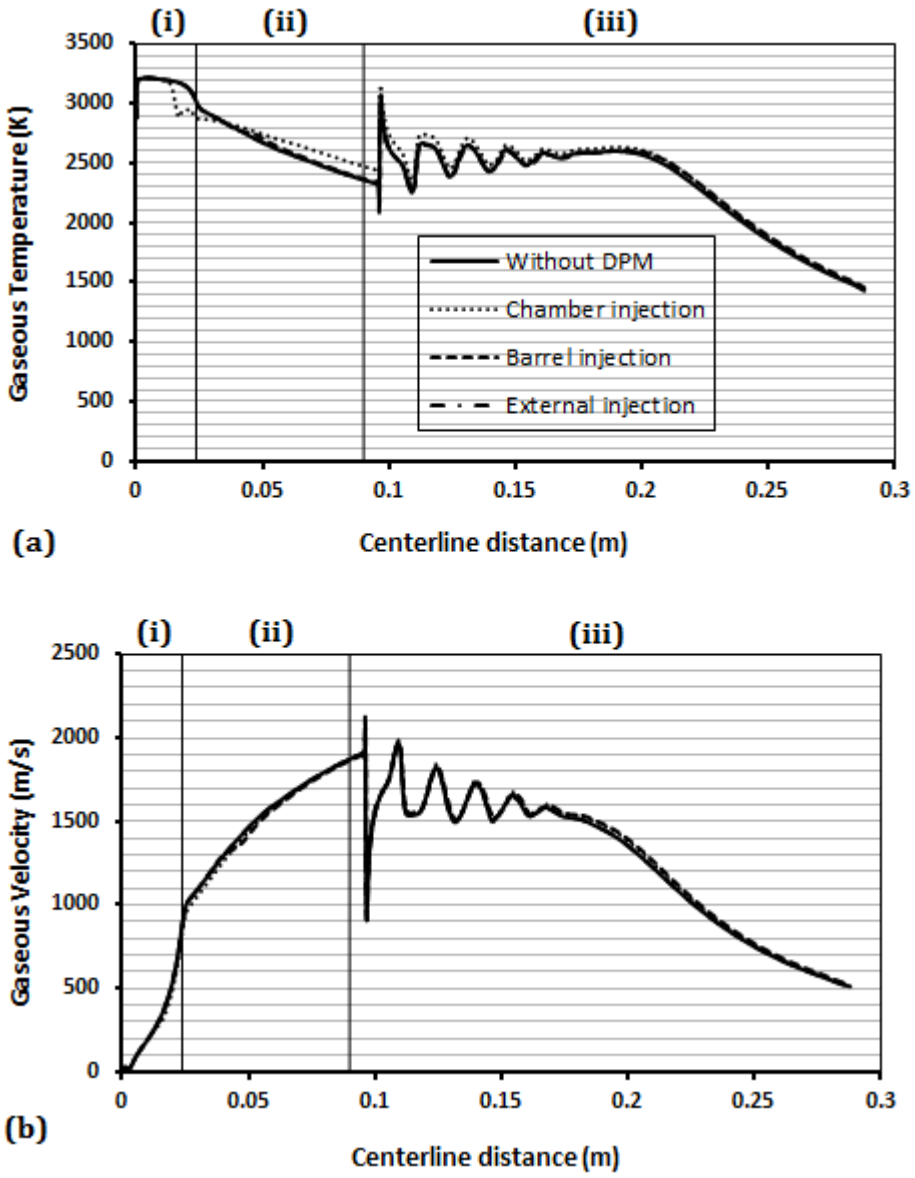

Figure 3-6: Comparison of (a) HVSFS temperature, and, (b) velocity fields experienced by droplets injected from combustion chamber, barrel, and free jet area

d), in injections from barrel and outside gun droplets are not able to penetrate into the core area of nozzle and starts quickly to breakup and evaporate very close to wall (for Barrel injection case) and spreading (for External injection) as they are subjected to high shear stress from gas velocity. For these two cases, another investigation was performed by increasing initial droplet velocity to 100 m/s. It is seen from Figure 3.7 (c and e) droplets traversed some distance vertically towards the core area of nozzle

for Barrel injection and spreading is reduced for External injection. Also it is observed being sent droplets into the core area, the droplets initial velocity must be specified to

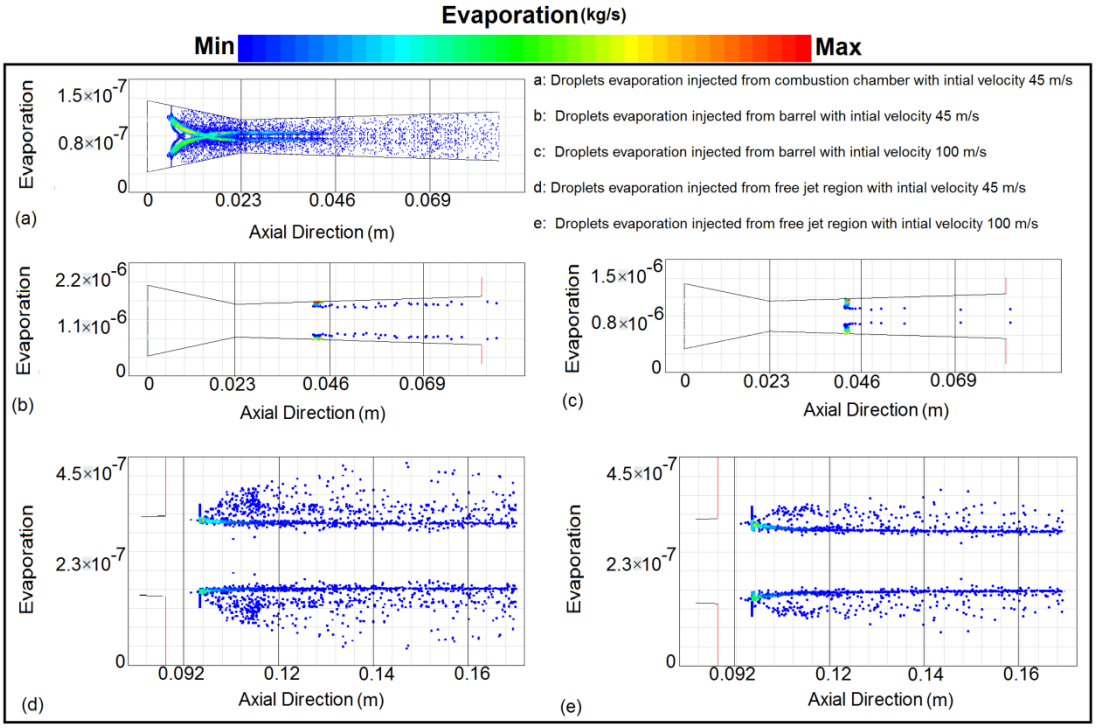

Figure 3-7: Comparison of droplets evaporation injected from (a) combustion chamber (b) and (c), barrel, and, (d and e) free jet region with initial velocity 45 and 100 m/s, respectively

a value of higher than 150 m/s, which is not applicable in practice. In contrast, droplets were injected from Combustion chamber shows good trend comparably with other radial and even axial injection positions see Figure 3.7 (a). It is evident that in this case droplets evaporate and subsequently cool gas temperature before convergent-divergent nozzle and right after that gas temperature exceeds the one to which droplets are not injected, see Figure 3.6 (a). In this case, the droplets initially travel through the cold part of the flame then start breaking up and evaporating. Importantly the length of evaporation area stretched in the combustion chamber, allowing droplets more residence time to evaporate before passing through the convergent-divergent nozzle. However, this type of injection is not commonly used in HVOF process because there is a pipe in outer part of gun in which cold water flows to cool it down. In summary, very high injection force is required to penetrate liquid droplets into the core of area of the gas stream as droplets injected from barrel and outside the gun. However, combustion chamber injection scheme can be considered for future HVSFS

gun design as it shows relatively good trend compared with axial and other radial injections.

3.7.4 Droplet Break-up Investigation

The droplets break up were studied by considering 50, 150 and 300 μm initial size droplets injected axially into the combustion chamber. Based on the previous parametric studies the droplet mass flow rate and initial velocity were selected 0.1 g/s and 30 m/s respectively. Initial temperature for droplets is assumed to be 300 K. Since droplets Weber number in the computational domain remains below 100 for axial injection scheme, TAB model was employed to model droplets break up (see previous sections for details). Figure 3.8 shows the comparison of droplets diameter distribution inside the combustion chamber and barrel where they reach the minimum size. Since, optimally, in HVSFS process droplets should break up and evaporate before they leave the combustion chamber, thus droplets were zoomed in inside the combustion chamber and partly in the barrel. It is evident that in all three cases, some droplets which are not fully evaporated leave the convergent-divergent nozzle with size less than 5 μm. Also a common phenomenon among all the cases is that in middle of combustion chamber, where relative velocity between gas and droplets is getting high, child droplet starts shedding from parent droplets and intensity of that is function of droplet diameter size as it can be seen from Figure 3.8: the larger the droplet diameter size, the higher is the shedding.

For instance, droplets with initial size 300 μm shrink to 80 μm 0.0075m away from back wall chamber where relative velocity and droplets Weber number reaches about 140 m/s and 45 respectively, thus droplets break up is more intense. In contrast, as droplets injected with initial size 50 μm the maximum Weber number attained was 14, therefore breakup intensity is reduced.

It should be noted that in the original design of the DJ 2700 gun the gas carrier tube is located at the centre of the back wall and that is surrounded by annular O/F inlets. That means there is a recirculation zone close to the back wall at the injection area. For this reason the particles start to spread out close to the nozzle throat where the flame reaches the axis of the torch and interacts with the droplets.

Overall, it can be concluded that a remarkable decrease in droplets diameter happens for both axial and radial injections as a consequence of droplet fragmentation

in HVSFS jet. However, in axial injection scheme, droplet breakup is highly influenced by its size. Moreover, severe droplets break up occurs outside the gun as droplets injected from barrel or free region area. Nevertheless, it should be mention

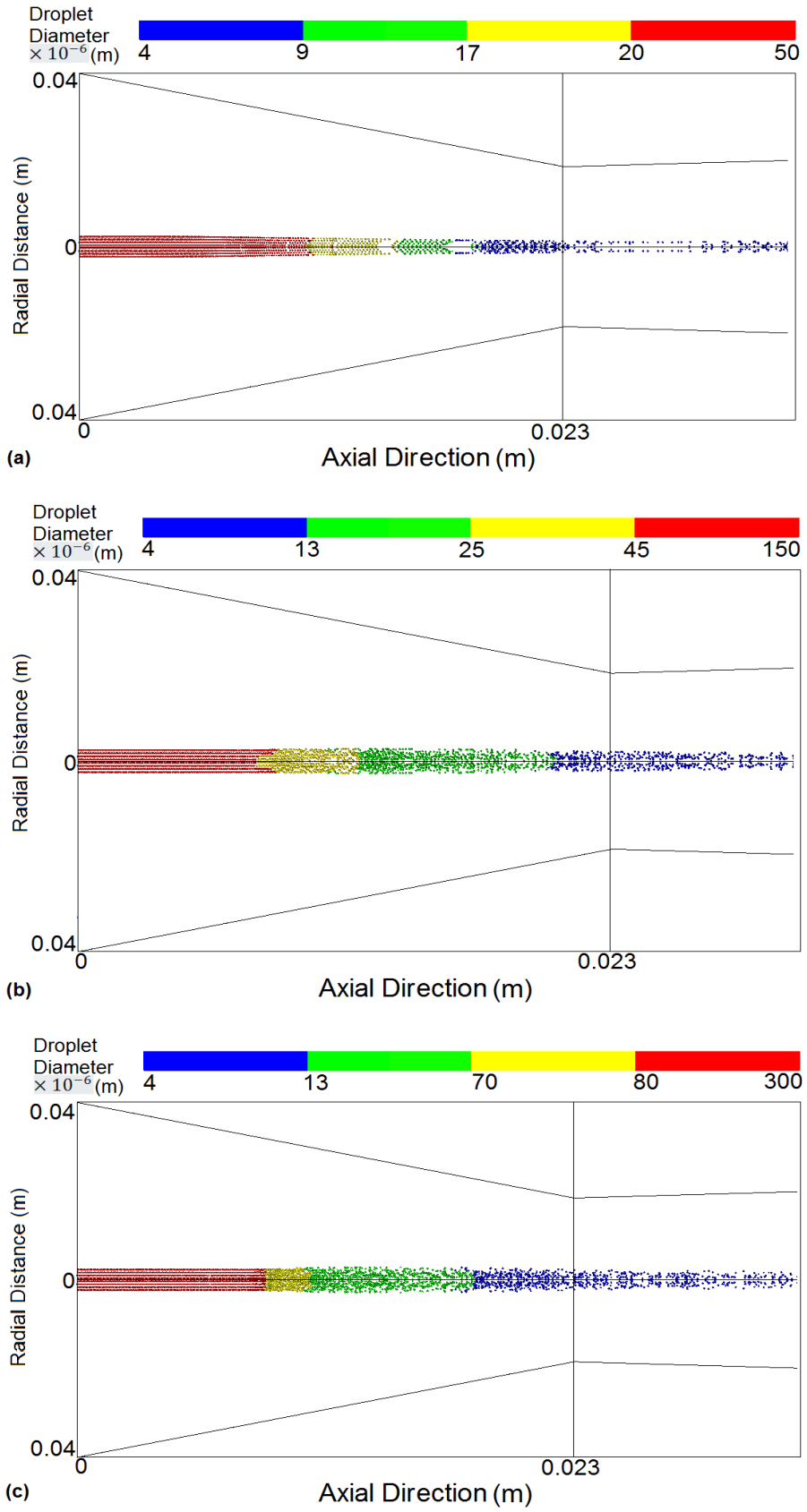

Figure 3-8: Comparison of droplet diameter distribution injected axially with initial diameter (a) 50, (b) 150 and (c) 300 µm

that validity of these results only remains for a uniform droplets diameter distribution introduced to the HVSFS jet axially or radially. Practically, since a spray cone with a variety of droplet diameters is injected to a thermal spray gun and velocity oscillations occurred due to the unsteady nature of HVSFS jet, these may create droplets any part of domain from sub-microns to tens of microns in diameter. Due to the fluctuations of velocity field jet, droplets with bigger diameter can be taken towards the low velocity jet area and may not experience aerodynamic fragmentation. Moreover, some amount of bigger droplets may not be fragmented as effectively as other, resulting in existence of bigger droplets tens of microns in size.

3.7.5 Combustion Analysis

There take place two kind of combustions in HVSFS process both of which are modelled by eddy dissipation model. First premixed combustion occurs by injecting gas propane into combustion chamber which combusts exothermically with pure hyper-stoichiometric oxygen, creating highly pressurized gaseous mixture at a maximum temperature of above 3200 K. The simulated exhaust gas mixture consisting of O, O_2, H_2, H, OH, H_2O, CO_2, and CO exits the combustion chamber (Figure 3-9). Then liquid ethanol droplets are injected into hot combustion chamber, where they heat, evaporate and again exothermically combust with remnant oxygen left from pre-mixed combustion (oxygen-propane). It should be noted that mass fraction of propane and oxygen should be fixed such that to attain maximum temperature (3200 K) in the combustion chamber before introducing liquid fuel droplets into the gun. This is clearly illustrated in Figure 3.10 which shows that supplying excessive oxygen in case2 disrupt the gas dynamics and reduce considerably the flame temperature. Figure 3.9 illustrates mass fraction of major species existing in the premixed combustion of propane with an excess of oxygen and non-premixed combustion of ethanol with oxygen left after complete propane combustion along centreline. From these figures it can be realized that even though supplying more oxygen during HVSFS process might lead to fully consumption of ethanol droplets, gas velocity and temperature are reduced in free jet region remarkably.

It is important to analyse oxygen, propane and ethanol mass fractions trend in HVSFS process because any unbalancing can lead to HVSFS gas and velocity field

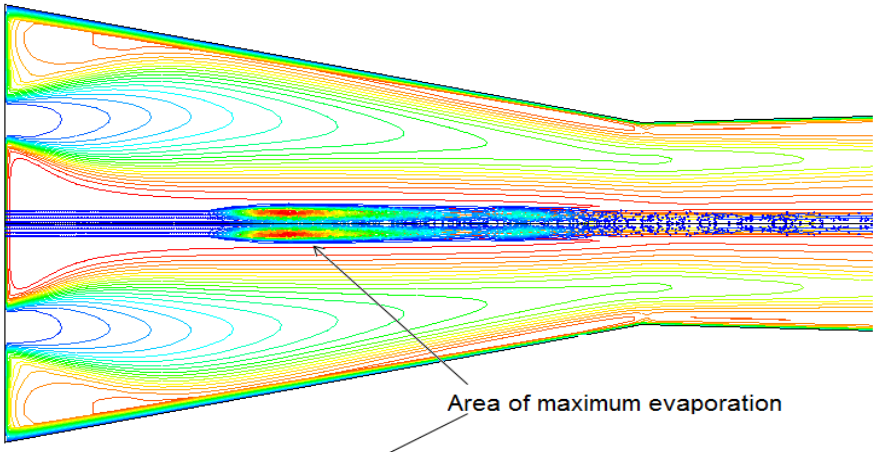

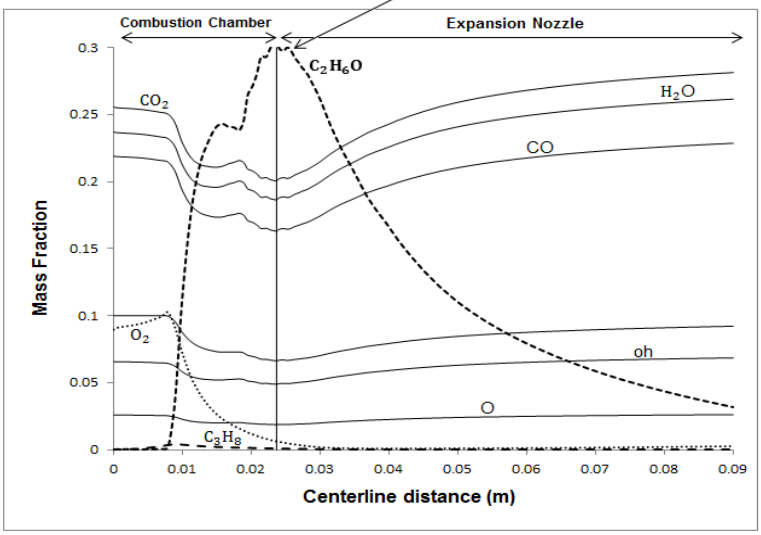

(Case 1)

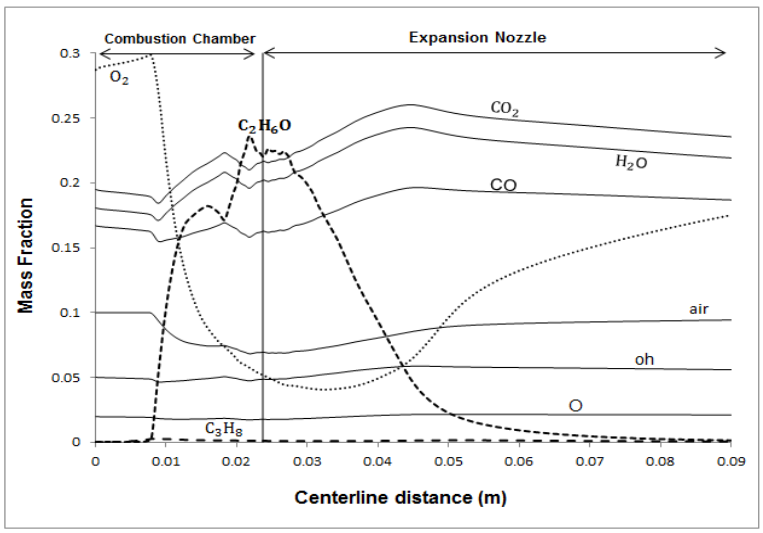

(Case 2)

Figure 3-10: Mass fraction of propane, oxygen, ethanol, and reaction products created from propane and gaseous ethanol oxidation (case 1) with oxygen/propane equivalence ratio of one, and, (case 2) oxygen/propane equivalence ratio of 0.73 in the HVSFS gun

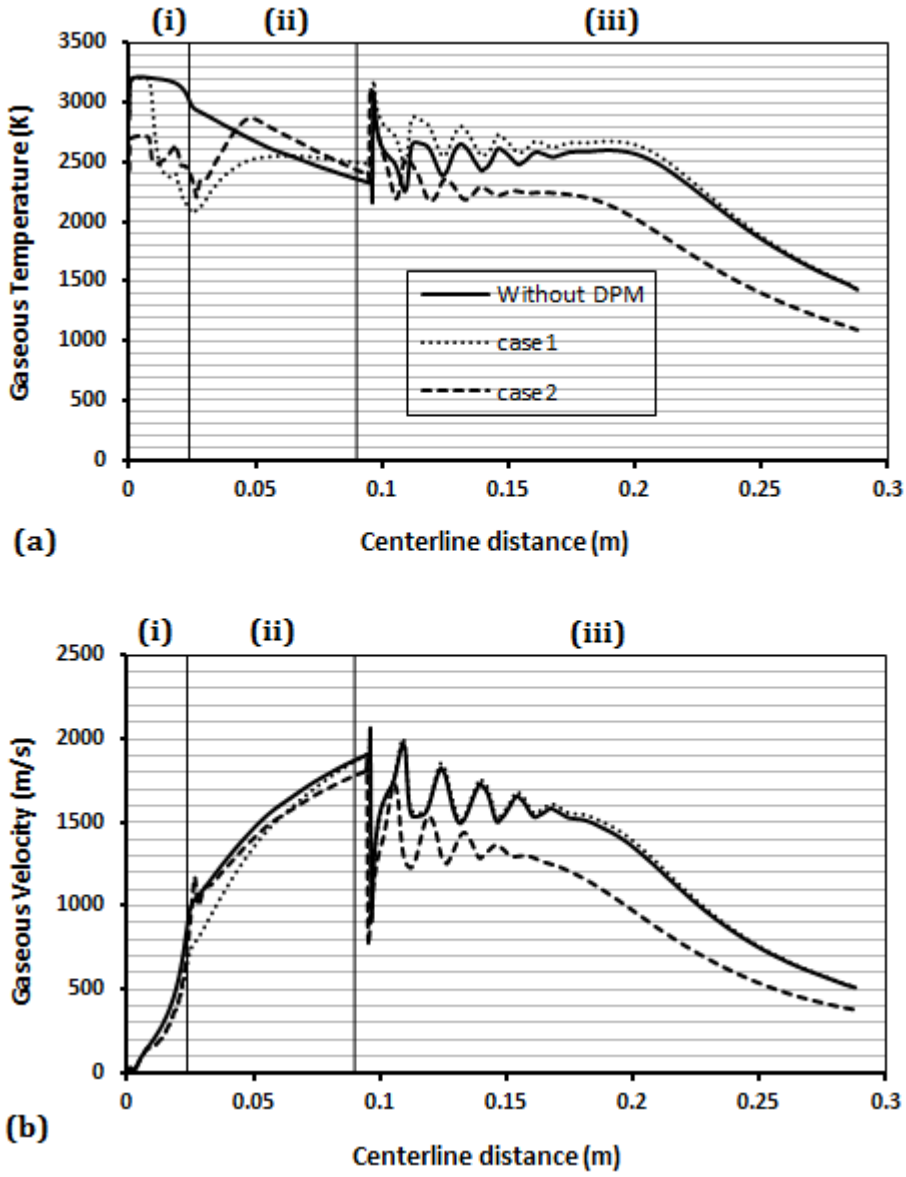

Figure 3-11: Comparison of (a) HVSFS temperature, and, (b) velocity fields along the centerline depicted for oxygen/propane equivalence ratio of 1 (case1) and 0.73 (case2)

disruption. Upon injection, gas ethanol mass fraction is zero and increase slightly until middle of combustion chamber, where child droplets begin to shed from parent droplets, and reach a peak at nozzle throat which corresponds to maximum area of evaporation and droplets diameter almost shrunk to less than 5 µm. Then it fell gradually and reached to lowest amount at barrel exit. In contrast, oxygen mass fraction remains constant and on its highest value until middle of combustion chamber and decreases steadily and reaches its minimum value where ethanol mass fraction is highest (nozzle throat). Comparison of ethanol and oxygen mass fraction shows that ethanol starts evaporating in middle of combustion chamber and reacts with remnant

oxygen left from pre-mixed combustion (propane-oxygen) and corresponding peaks in nozzle throat (maximum for ethanol and minimum for oxygen), where take place maximum reaction between ethanol and oxygen. Propane mass fraction along the centreline shows that it is completely consumed inside the combustion chamber.

3.8 Conclusion

A detailed modelling and analysis of liquid ethanol droplets processed in an HVSFS flame jet has been presented in this chapter. The presented model encompasses parametric investigation and effects of location injection on HVSFS process. Summary of findings are listed below:

- Parametric investigation revealed that initial mass flow rate of liquid feedstock mainly controls the HVSFS process. If optimum amount of liquid mass is injected to a gun, the area of maximum evaporation will occur inside combustion chamber, leading to less cooling of the gas temperature and less reduction of gas velocity. However, if more amount of liquid mass injection is demanded, design of a conventional HVOF gun should be modified such that its combustion chamber accommodates the area of maximum evaporation of suspension.
- Barrel and external injection schemes are not likely suitable for HVSFS process as high injection force is required to penetrate liquid droplets into the core area of the gas dynamics. However, as droplet injected from combustion chamber vertically inward, relatively good output is observed e.g. the gas dynamics is less disrupted and area of maximum evaporation occurs inside the combustion chamber.
- Droplet break-up analysis showed that neglecting modelling droplet secondary break-up in numerical analysis of HVSFS process can lead to high order of errors, since liquid droplets undergo considerable fragmentation in middle of combustion chamber due to large relative velocity between gas and liquid phases in axial injection scheme in which fragmentation intensity is function of droplet size: the larger are the droplets, the more intensive is the break up. Quantifying the error involved in neglecting modelling fragmentation is out of scope this research work.

- Combustion analysis illustrated that being achieved maximum gas temperature and velocity in the HVSFS process, oxygen and propane mass fraction should be fixed before introducing liquid feed stock into the gun. Nevertheless, liquid ethanol droplets may not fully combust inside the nozzle due to the lack of oxygen.

4 Multicomponent Suspension Droplets

The process characteristics, the microstructure and phase composition of the coatings are significantly influenced by the liquid phase of the suspension or solution which can be homogeneous or mixture solvent. Depending on a desired application, different types of solvent or mixture ratio can be used. In this chapter, it is aimed to analyse the effects of type of solvent and mixture of solvent with different ratios, as liquid phase of the suspension, on the liquid droplets fragmentation, evaporation and combustion, and on the HVSFS gas dynamics. In this study, solvent mixture is treated as a multicomponent droplet of ethanol and water with various ratios. It should be noted that modelling solvent as a multicomponent droplet is not yet addressed in the thermal spray literature. This work, thus, takes initiation to give an insight into the underlying physics and depicts mixture solvent behaviour in the HVSFS process. For this, a convection/diffusion model is employed to simulate multicomponent droplet evaporation which considers the convective flow of evaporating material from droplet surface (Stefan Flow). The model consists of several sub-models that include modelling HVSFS flame jet turbulence by taking into account the compressibility effects, premixed combustion of propane-oxygen, non-premixed combustion of ethanol-oxygen, modelling aerodynamic of single and multicomponent droplets breakup, evaporation, heat and mass transfer between liquid and gas phases, at the example of an industrial DJ2700 torch (Sulzer-Metco, Wohlen, Switzerland).

4.1 Numerical Schemes and Governing Equations

A schematic diagram of the DJ2700 thermal spray system along with the computational domain, boundary conditions, and refinement regions are given in Chapter 3. The inlet fuel conditions and the geometric parameters are the same as those listed in Chapter 3 [92]. The governing equations of the gas flow as well as turbulence and combustion models are in detail described in Chapter3. Both pre-mixed (oxygen-propane) and non-premixed (oxygen-ethanol) combustion reactions

were solved by eddy dissipation model with hyper-stoichiometric oxygen mass fraction, which is outlined in the previous chapter. Since the axial injection is only considered in this chapter, the secondary breakup of droplets to smaller one is modelled by Taylor Analysis Breakup (TAB) model and its description is provided in the previous chapter. There has been done some modification to the single droplet heating and mass transfer to the continuous phase which will be explained in the following section along with modelling of the multicomponent droplets.

4.1.1 Single Droplet Heat up and Vaporization

Homogenous droplets heat and mass transfer with continuous phase are modelled based on three laws and at each tracking time relevant law is applied based on droplet conditions. Details of the laws, equations of motion and droplets secondary breakup are described in Chapter 3; however, a modification has been done to the second law of the vaporization, which takes into account the effects of the convective flow of the evaporating material from the droplet surface to the bulk phase as this model is more complete than the previous one. The law 2 or convection/diffusion controlled model has been adopted following the work of Miller [93] and Sazhin [94]:

$$\frac{dm_d}{dt} = A_d k_c \rho_\infty ln(1 + B_m) \tag{4.1}$$

Where B_m is the Spalding mass number given by:

$$B_m = \frac{(Y_s - Y_\infty)}{1 - Y_s} \tag{4.2}$$

where Y_s is vapour mass fraction at the droplet surface and Y_∞ vapour mass fraction in the bulk gas.

And k_c is calculated from the Sherwood number correlation as:

$$Sh_{AB} = \frac{k_{c,i} d_d}{D_{i,m}} \left(2 + 0.6 Re_d^{0.5} Sc^{1/3}\right) \tag{4.3}$$

The droplet temperature during this law is updated according to Equation 3.39, however, the convective heat transfer coefficient, h, is calculated with a modified Nu number as follows [94]:

$$Nu = \frac{h d_d}{K_\infty} = \frac{ln(1 + B_T)}{B_T} \left(2.0 + 0.6 Re_d^{1/2} Pr^{1/3}\right) \tag{4.4}$$

where B_T is the Spalding heat transfer number and assumed to be equal to the Spalding mass transfer number, B_m, calculated for Equation 4.1:

$$B_T = B_m \tag{4.5}$$

4.1.2 Multicomponent Droplet Heat up and Vaporization

A multicomponent particle is a droplet particle containing a mixture of several components or species (ethanol and water in this study). The conservation equations of all components, the energy equation, and vapour-liquid-equilibrium at the multicomponent particle surface form a coupled system of differential equations. A multicomponent law is developed for such systems described in this section.

The volume weighted mixing law is used to define the particle mixture density. The particle mass 'm' is the sum of the masses of the components:

$$m_{mix} = \sum_i mi \tag{4.6}$$

The density of the particle ρ_{mix} is volume-averaged:

$$\rho_{mix} = \left(\sum_i \frac{m_i}{m\rho_i}\right)^{-1} \tag{4.7}$$

The other properties of multicomponent droplet such as viscosity, specific heat, and surface tension are defined as mass weighted mixing law, which is computed based on a simple mass fraction average of pure species properties:

$$\emptyset_{mix} = \sum_i Y_i \emptyset_i \tag{4.8}$$

where Y_i and $\emptyset_i$ are mass fraction and properties of species respectively.

The complete droplets properties are listed in Table 4.1. Saturation vapour pressure and diffusion coefficient of one-component droplets are input as function of temperature. A film-averaged temperature is defined based on droplet and gas phase temperatures for accurately computing diffusion coefficient of single-component droplets:

$$T_f = T_d + a(T_\infty - T_d) \tag{4.9}$$

where a is averaging coefficient and set to 0.5.

The evaporation rate of multicomponent droplet is calculated as the sum of the vaporization rates of the individual components and the vaporization rate of each component (water and ethanol) is calculated as follows [93-94]:

$$\frac{dm_i}{dt} = A_d\, k_{c,i}\, \rho_\infty\, ln(1 + B_{m,i}) \tag{4.10}$$

where A_d is droplet surface area, ρ_∞ is density of gas, and $B_{m,i}$ is Spalding mass number for species *i.*

When the total vapour pressure at the droplet surface exceeds the cell pressure, the multicomponent droplet is in the boiling regime and boiling rate Equation 4.11 is applied. The total vapour pressure is computed as $P_t = \sum P_i$ where P_i is the partial pressure of component *'i'*.

$$\frac{dm_i}{dt} = x_i \frac{\pi k_\infty d_d}{C_{p,\infty}} \left(2 + 0.6 Re_d^{0.5} Pr^{1/3}\right) ln(1 + B_{T,i}) \tag{4.11}$$

Where k_∞ and $C_{p,\infty}$ are thermal conductivity and specific heat of bulk gas.

$$B_{T,i} = \frac{C_{p,\infty}(T_\infty - T_d)}{h_{vap,i}} \tag{4.12}$$

where T_∞ and T_d are gas and droplet temperatures respectively. $h_{vap,i}$ is latent heat for species *i.*

Properties	Water (liquid)	Ethanol (Liquid)	Mixture
Density (Kg/m^3)	998.2	790	Volume-weighted-mixing-law
Specific Heat $(J/Kg-K)$	4182	2470	Mass-weighted-mixing-law
Viscosity (kg/m-s)	0.001003	0.0012	Mass-weighted-mixing-law
Latent Heat (J/Kg)	2263073	855237	-
Vaporization Temperature (K)	284	271	-
Boiling Point (K)	373	351	-
Binary Diffusivity (m^2/s)	Film-averaged	Film-averaged	-
Saturation Vapour Pressure (Pa)	Piecewise-linear	Piecewise-linear	-
Surface Tension (N/m)	0.0719404	0.022348	Mass-weighted-mixing-law
Vaporization Model	-	-	Convection/diffusion-controlled
Vapour-Particle-Equilibrium	-	-	Raoults- law

Table 4-1: Properties are taken from Perry's Chemical Engineering Handbook [95] and curve-fitted in their temperature range

The equation for the multicomponent droplet temperature T contains terms for convective heating and evaporation, and is cast similarly to the one component droplet energy equation. The energy equation for the multicomponent particle is written as follows:

$$m_d c_d \frac{dT}{dt} = hA_d(T_\infty - T_d) + \sum_i \frac{m_i}{dt}(h_{vap,i}) \quad (4.13)$$

where $\frac{dm_i}{dt}$ is computed from Equation 4.10 and the heat transfer coefficient h is computed similar to Equation 4.4:

$$Nu = \frac{hd_d}{k_\infty} = \frac{ln(1+B_{T,i})}{B_T}\left(2 + 0.6Re_d^{0.5}Pr^{1/3}\right) \quad (4.14)$$

4.2 Results and Discussion

With the assumption that nanoparticle loading is very low (less than 5%), the suspension is treated as homogenous droplet particles either in the form of single or multicomponent droplets, representing pure and mixture solvent respectively. Since the results of gas phase modelling and parameters controlling the HVSFS process such as droplets mass flow rate, droplets size and initial velocity are extensively described in the previous chapter, only illustration of solvent fragmentation, evaporation, and cooling effect is adequate to highlight the effects of solvent type or mixture ratio on the HVSFS process. Therefore, those results will not be further analysed here. It should be noted that mixture of solvent with different ratios are commonly used in the HVSFS process and their ratio in practice is found by performing costly trial and error experiments. The mixture ratios, in this study, are selected according to the commonly used ratios in experimental studies in order to illustrate their impact on the process. Without Droplet case in the text and graphs refers to the case in which no droplets are injected into the gun and denotes the HVOF gas dynamics. Droplets are injected through gas carrier tube inlet at the centre of the O/F mixer and it is surface injection.

4.2.1 Effects of Solvent Mixture Ratio on its Vaporization

Different ratios of ethanol and water mixture (multicomponent droplet) are injected into the DJ2700 gun and their trajectories are numerically studied. Among them, four

ratios are selected, namely: pure ethanol, 90% ethanol-10% water, 50% ethanol-50 % water, and pure water as critical changes happen in these ratios. Both single and multicomponent droplets mass flow rates, diameters and initial velocities are selected to be 0.1 g/s, 300 μm, and 30 m/s respectively. These initial injection parameters are selected based on the previous parametric study [92]. The initial droplets temperature is assumed to be 300 K. Figure 4.1 shows the rate of evaporation of these mixtures in HVSFS process along the axis of the computational domain. It is evidently shown that maximum evaporation occurs inside the combustion chamber for the cases with high

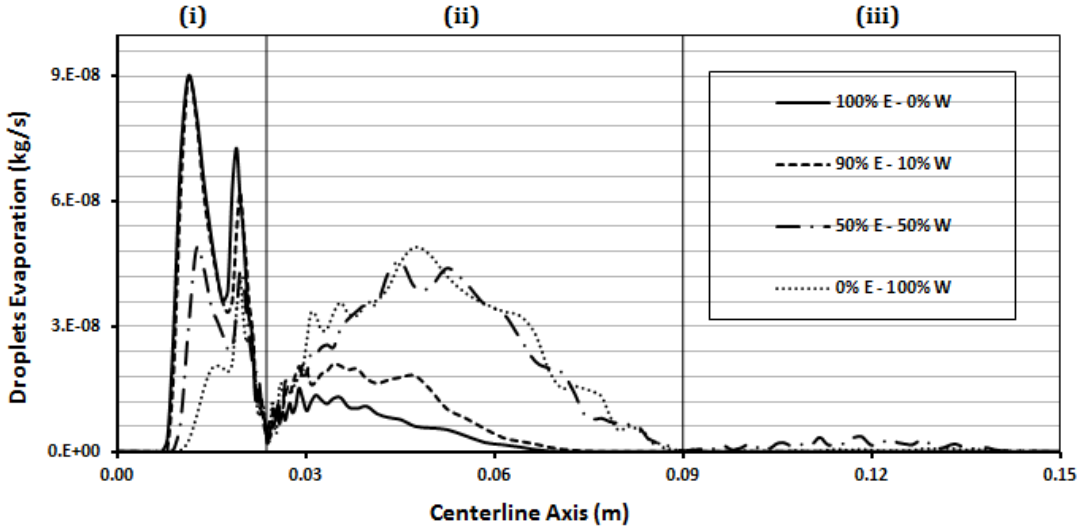

Figure 4-1: Rate of Evaporation of droplets carrying four different percentage of Ethanol-Water in Solvent along the centerline

ethanol content in the solvent. All droplets evaporate well before the gun exit. In contrast, for multicomponent droplets with high percentage of water (more than 50%), the evaporation is significantly delayed and takes place in all internal regions of the gun including the external jet region in some cases. The longest distance of complete evaporation in free jet region is observed for pure water (57 mm away from gun's barrel exit). Monitoring the vaporization rate of droplets inside the nozzle and the free jet region (Figure 4.2), it can be realized that adding small quantities of water (almost 10%) to ethanol solvent does not affect considerably the evaporation rate. In this case all liquid droplets evaporate completely before the gun exit. However, the area of maximum evaporation shifts to the barrel and the final location of evaporation moves to the free jet region when the solvent is pure water. It should be noted that droplets are mainly concentrated on the gun axis due to its injection structure that located at

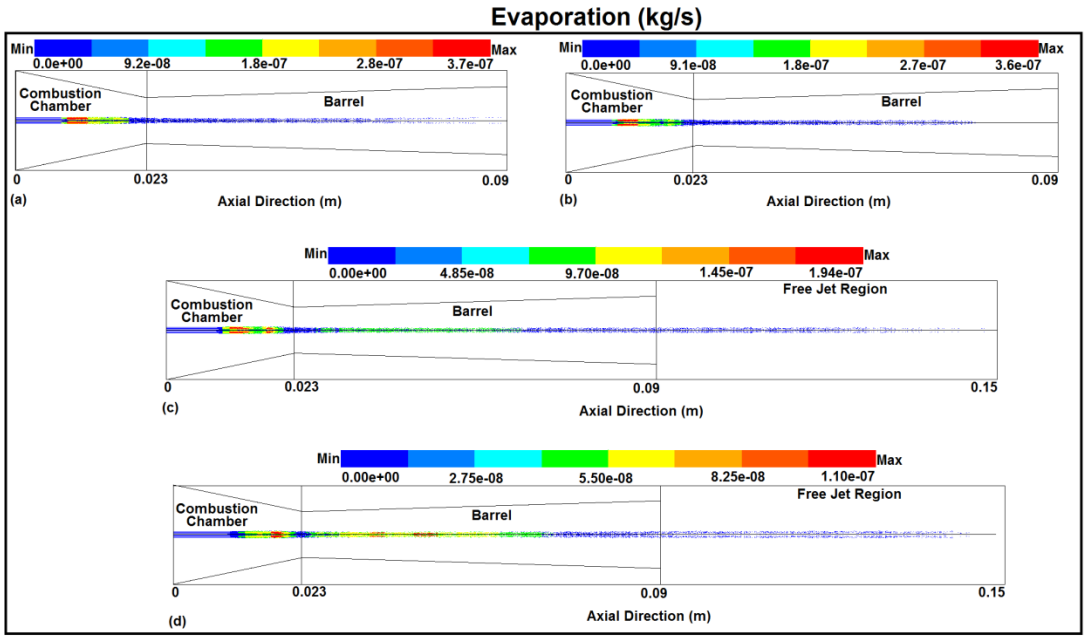

Figure 4-2: Rate of Evaporation of droplets carrying (a) 100% E – 0% W, (b) 90% E – 10% W, (c) 50% E – 50% W, and (d) 0% E – 100% W, Ethanol-Water in Solvent inside the nozzle

the centre of O/F mixer. For this reason the centreline axis can be well representation of droplets evaporation and breakup and other phenomena. Droplets severe fragmentation especially in the middle of the combustion chamber along with the gas temperature and velocity profiles and turbulence can be main reasons for oscillations in droplets evaporation rate in the Figures 4.1 and 4.2, which illustrate the vaporization rate of drops along the gun centreline axis and whole computational domain respectively.

A physical property that has a significant influence on the vaporization rate is the solvent boiling point. Figure 4.3 shows the variation of the boiling temperature of these mixtures along the centreline. A comparison between Figure 4.3 and previous ones (Figures 4.1 and 4.2) reveals that the lower is the solvent boiling temperature, the higher is the vaporization rate. In fact, solvent with high content of ethanol possess lower boiling temperature and requires less heat for full evaporation; whereas increasing the mass fraction of water in the solvent leads to rise in boiling temperature and in turn the evaporation rate becomes smaller. Also it should be noted that the boiling temperature in all cases varies inside the nozzle due to the changes in the pressure. The ethanol boiling temperature is 351 K in atmospheric pressure while it is approximately 400 K inside the combustion chamber that operates under high pressure of almost 4 bar and decreases along the centreline as pressure is falling.

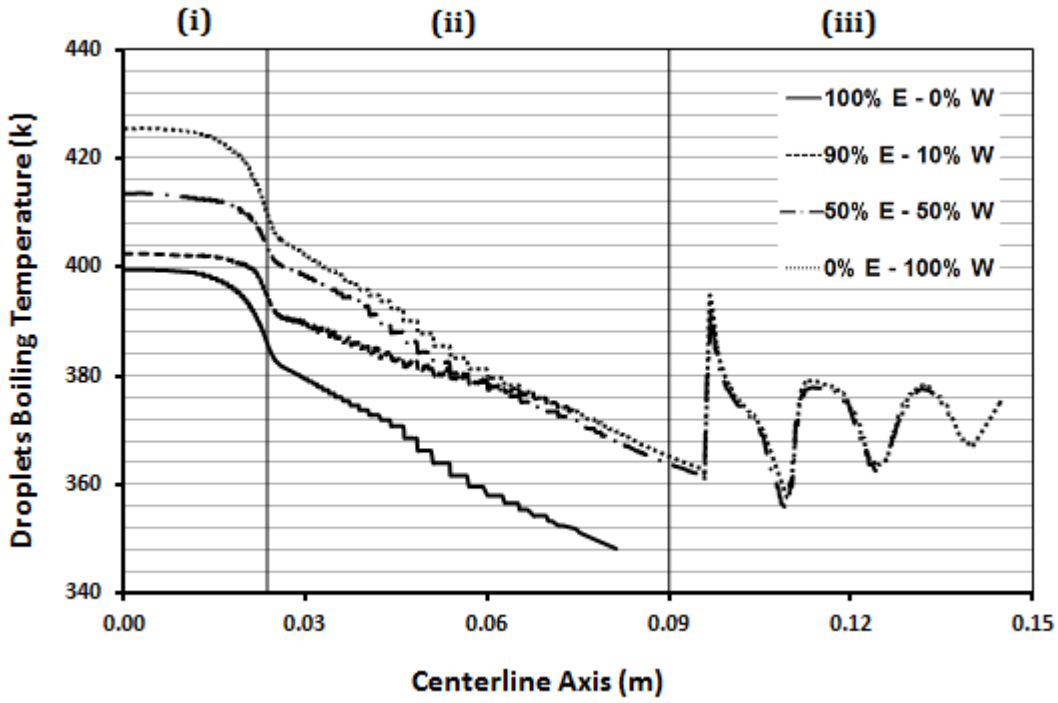

Figure 4-3: Boiling temperature of droplets carrying different percentages of Ethanol-Water in solvent along the centerline

These results are consistent with experimental studies in the literature [3 and 50-51]. In the suspension plasma spray, which is a process similar to the HVSFS, Fauchais et al. [3] conducted experimental studies on the effects of ethanol and water solvent on the zirconia splat formation. They found under the same plasma and processing conditions, water droplets evaporate later than ethanol droplets and the zirconia particles contained in ethanol were melted while those in water were partially melted. In solution precursor plasma spray, which is again a similar process to the HVSFS, Chen et al. [51] studied experimentally the influence of solvent type on splat formation and coating microstructure. They found that droplets with a high surface tension and high boiling point undergo incomplete evaporation in the plasma jet resulting in porous coatings. In contrast, droplets with low surface tension and low boiling point experience rapid solvent evaporation followed by fully molten splat microstructure and high density coatings. The numerical results in this study are fully aligned with major experimental outcomes in literature. Organic solvent (ethanol) or solvent mixture with low percentage of water undergoes fast evaporation and subsequent early release of nanoparticles. The exact location where the particle heating is initiated (above the carrier liquid boiling point) can be controlled by

increasing the water content of the mixture. In this way the particle in-flight time in the high temperature gas regions can be adjusted for controlling the undesirable surface chemical transformations. Numerical modelling is the only direct method which can provide such information overcoming the technical constrains imposed by the experiments.

4.2.2 Effects of Solvent Mixture Ratio on Droplet Fragmentation

Droplet fragmentation is another important phenomenon in the HVSFS process which can be influenced by the solvent type and solvent mixture ratio. As long as the Ohnesorge number remains well below 0.1 in the computational domain, viscous forces are negligible and aerodynamic and surface tension forces are the only dominant parameters affecting the droplet fragmentation. Therefore the only parameter or non-dimensional number related to droplets breakup is the Weber number, which remains below 100 in the computational domain that's why TAB model is selected to simulate droplets secondary breakup.

Figure 4.4 illustrates the Weber number of droplets injected into the DJ2700 gun under various ethanol-water ratios in the solvent along the centreline. Maximum Weber number of about 44 is observed for the solvent with pure ethanol (Figure 4.4a) and the maximum Weber number decreases by rising the water mass fraction in the solvent (Figure 4.4b and 4.4c). Weber number reaches the lowest value of almost 22 (Figure 4.4d) when the solvent is pure water. The reason is that the value of surface tension for ethanol ($\sigma_{\mathrm{eth}} = 22 \times 10^{-3}\ \mathrm{N/m}$) is three times less than that of water($\sigma_{\mathrm{W}} = 72 \times 10^{-3}\ \mathrm{N/m}$). Hence, solvent with high percentage of ethanol has higher Weber number. Furthermore, the reason for Weber number oscillation in the Figure 4.4 is that fast developing relative velocity between droplets and gas phase and increasing Weber number lead to consecutive breakups inside the gun especially inside the combustion chamber and oscillation in the Weber number.

In all cases, the value of Weber number stays well above 14 inside the combustion chamber, which indicates relatively high fragmentation. This can be clearly seen in Figures 4.5 and 4.6 that display the reduction of droplets diameter with varying ethanol-water ratios in the solvent along the axis. For all cases, droplets undergo severe fragmentation at two subsequent locations inside the combustion chamber. First fragmentation occurs in the middle of combustion chamber causing a

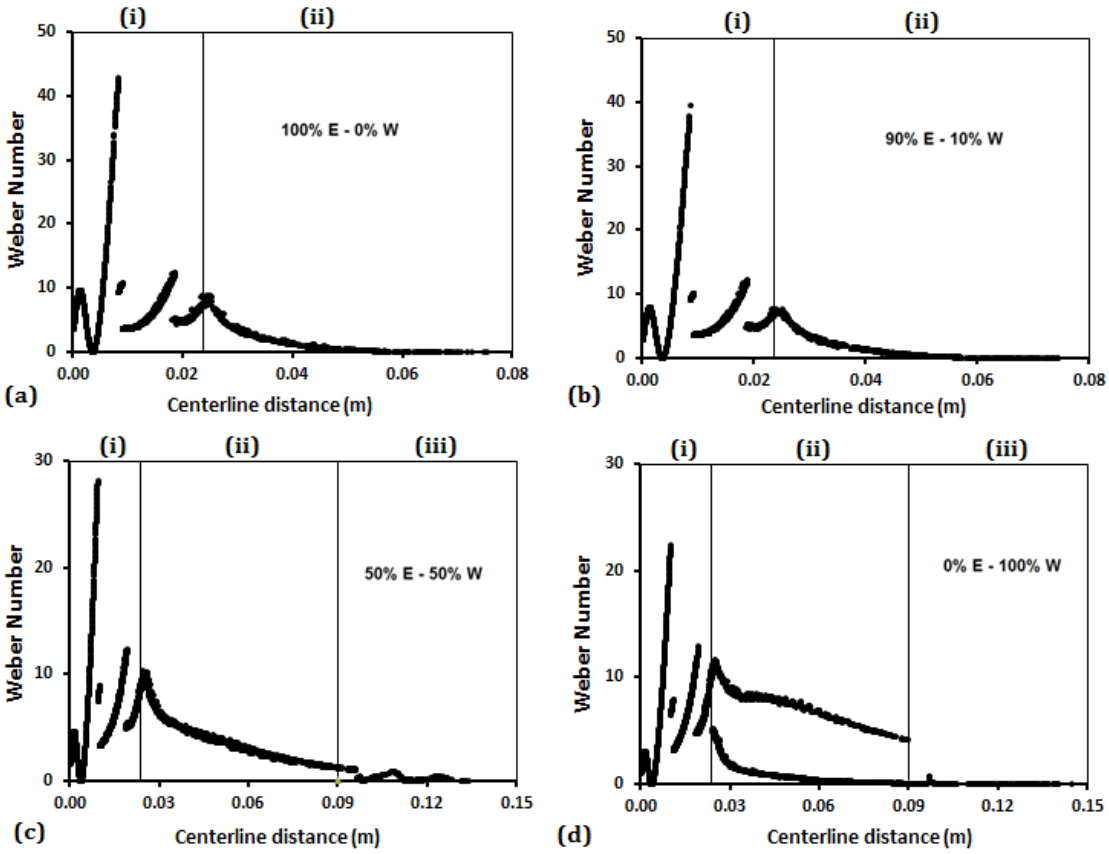

Figure 4-4: Weber number of droplets carrying (a) 100% E – 0% W, (b) 90% E – 10% W, (c) 50% E – 50% W, and (d) 0% E – 100% W, Ethanol-Water in solvent along the centerline

sharp decrease in the droplets size from 300 µm to 66, 71, 82 and 88 µm, for 100% E – 0% W, 90% E – 10% W, 50% E – 50% W, and 0% E – 100% W cases, respectively.

The second fragmentation occurs some distance away from the first location (shown in Figure 4.6) and results in a considerable reduction of droplets diameter from 66 to 23, 71 to 25, 82 to 30 and 88 to 35 µm. Then the droplets leave the combustion chamber with 5, 5, 9, and 13 µm, for the above mentioned cases respectively. The maximum reduction of droplets diameter is attributed to the corresponding maximum Weber number inside the combustion chamber for each case. However, having left the combustion chamber, it is evident that droplets experience much less effective breakup in the barrel and outside the gun. The reason is that the Weber number lies under 10, while vaporization dominates the droplet size reduction process. In some cases, the escaping larger droplets experience late evaporation due to their high travelling speed meaning that their dwell time is low (Figure 4.6 c and d).

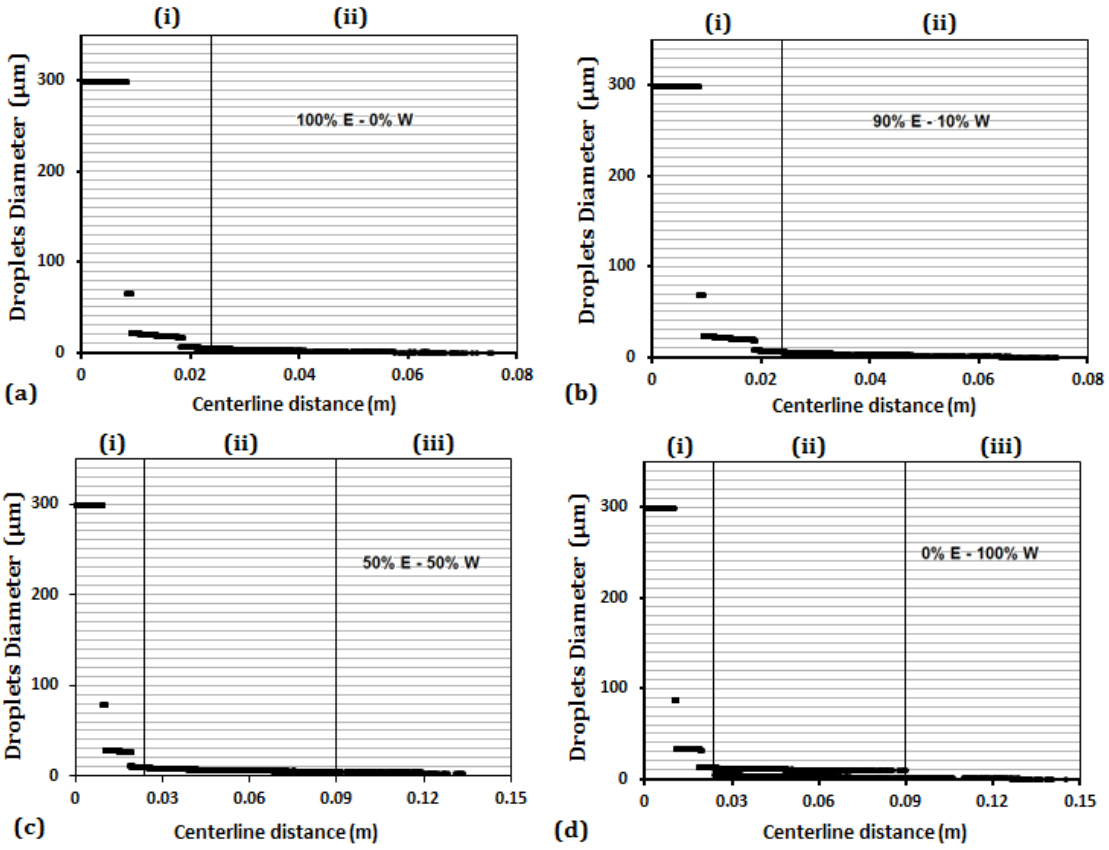

Figure 4-5: Variation of droplets diameter containing (a) 100% E – 0% W, (b) 90% E – 10% W, (c) 50% E – 50% W, and (d) 0% E – 100% W, ratios of ethanol and water in solvent along the centerline

In summary, liquid droplets experience severe fragmentation two times inside the combustion chamber in the HVSFS gun owning to the large relative velocities. The intensity of the breakup depends mainly on the type of solvent and solvent mixture ratio: the lower is the solvent surface tension, the more intense is the breakup. Also, the reason for choosing the centreline for studying the droplet fragmentation and vaporization is that the main emphasize is the location of breakup and evaporation rather than time. However, time of breakup and evaporation can be considered for further investigation of these physical phenomena.

4.2.3 Effects of Solvent Mixture Ratio on the HVSFS Gas Dynamics

Four different ratios of ethanol and water mixture (100% E + 0% W, 90% E + 10% W, 50% E + 50% W, and 0% E + 100%W) as solvent are selected and their evaporation and corresponding cooling on the HVSFS gas temperature and velocity are investigat-

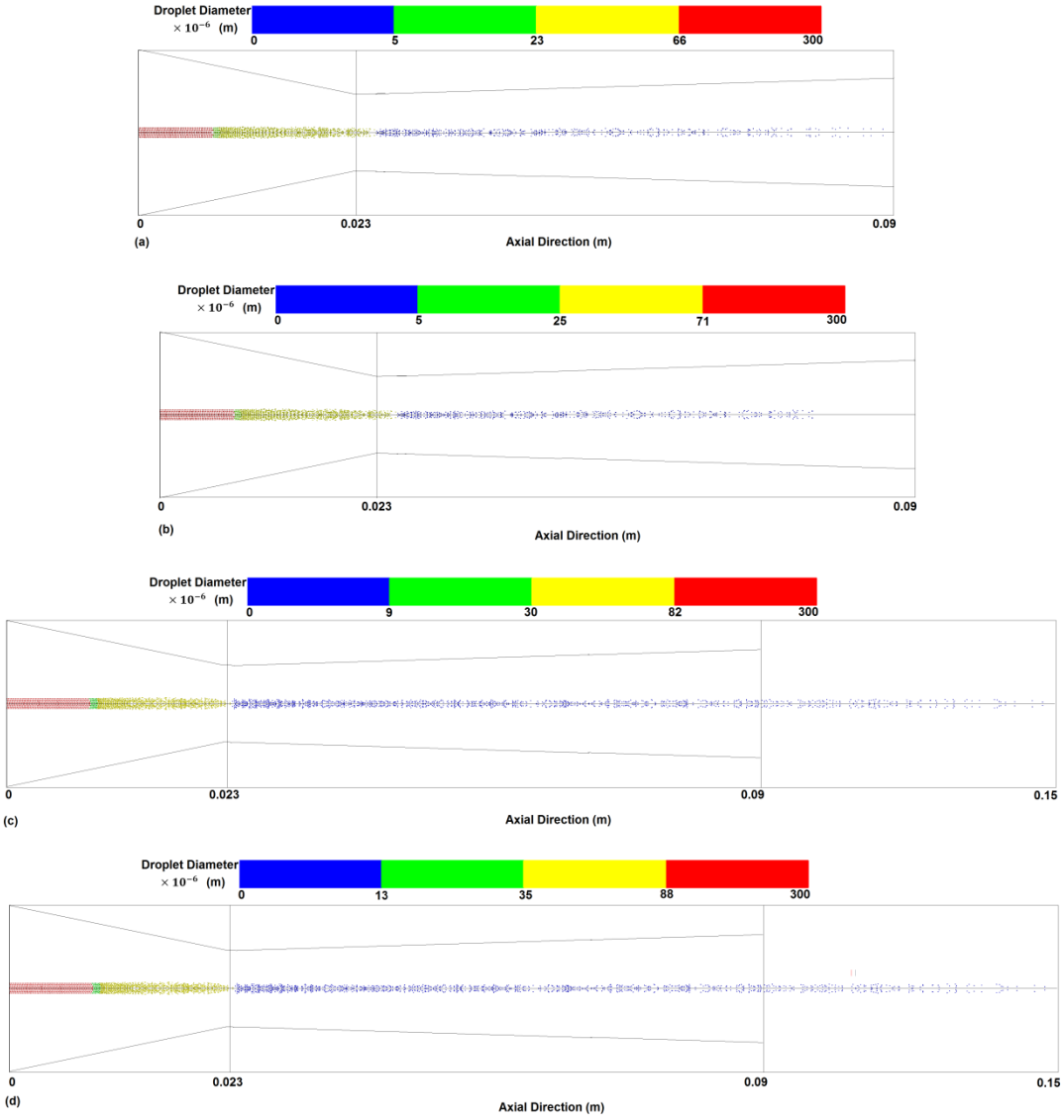

Figure 4-6: Variation of droplets diameter containing (a) 100% E – 0% W, (b) 90% E – 10% W, (c) 50% E – 50% W, and (d) 0% E – 100% W, ratios of ethanol and water in solvent inside the nozzle

ed, as illustrated in Figures 4.7 (a-b). It is clear from Figure 4.7 (a) that for all solvent compositions the gas temperature drops to some extend along the axis. However, the cooling intensity depends on the type of solvent and solvent mixture ratio: combustible ethanol droplets have the lowest cooling effect on the gas temperature which mainly takes place inside the combustion chamber and moderately in the barrel. This means the evaporation is completed earlier and discharged nanoparticles have enough time to melt and leave the gun with high velocities. In contrast, adding a small amount of water into the solvent mixture results in highly reduced gas temperature both inside the combustion chamber and the barrel. The extreme gas cooling of appr-

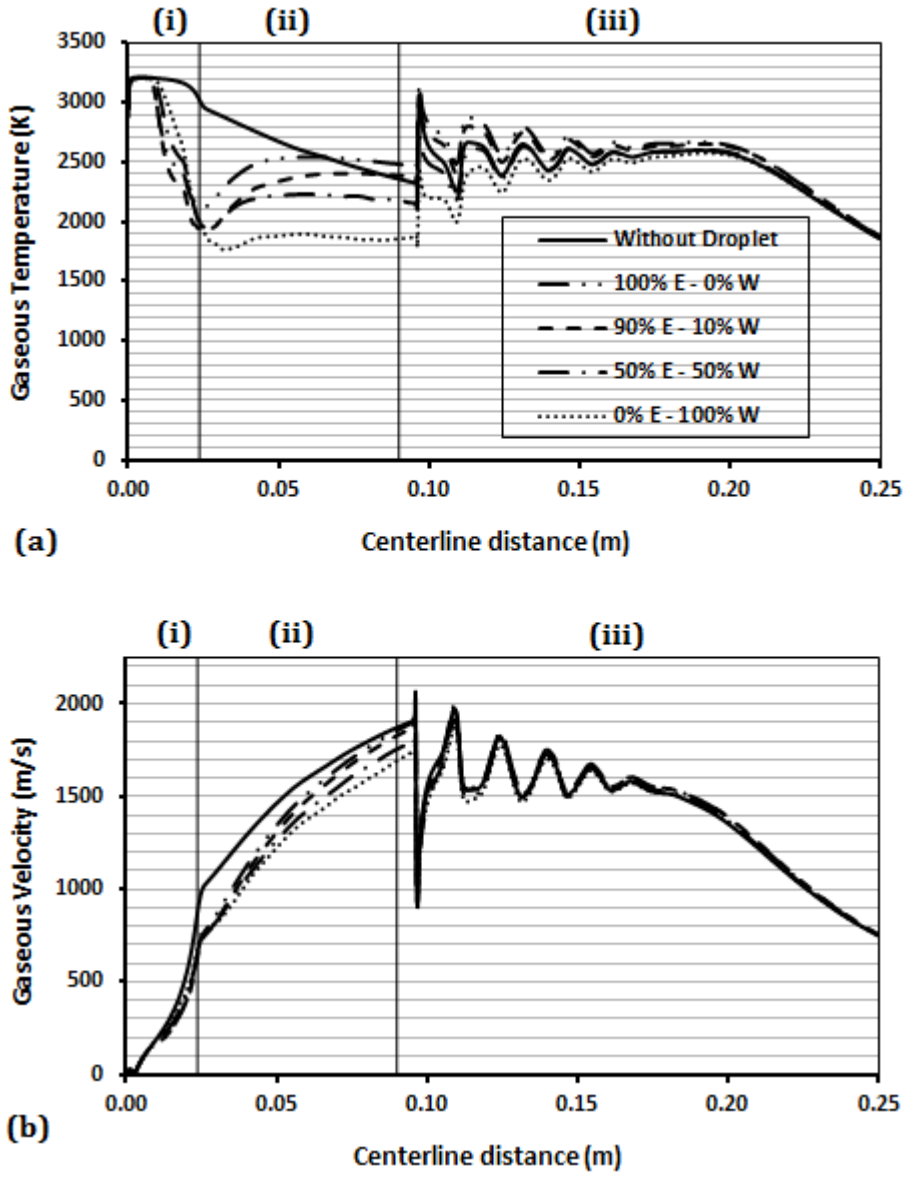

Figure 4-7: Profile of (a) gaseous temperature (b) gaseous velocity for Without Droplet case and cases with droplets carrying different percentages of Ethanol-Water in solvent along the centerline

oximately 1200 K, mainly in the barrel, is reasonably observed for pure water solvent (Figure 4.7-a). This is due to the fact that water droplets are less sensitive to aerodynamic break up compared to ethanol droplets. Gradual evaporation occurs along the nozzle and free jet region leading to gas phase cooling. High cooling of the gas temperature can cause flame stretching which can trigger instabilities within the gun and eventually reduction of the gas velocity. The effects of solvent evaporation on the gas velocity can be seen in the Figure 4.8. Similarly the gas velocity is highly

influenced by droplets evaporation and gas cooling as such the maximum reduction of about 250 m/s in the barrel is observed for the case with pure water, which corresponds to the maximum gas cooling. The influence of the solvent composition in the aerodynamic and thermal performance of the gun, opens a new window for active flow control of the HVOF process by adjusting the solvent mixture ratio to the desired levels. Overall, the results suggest that any liquid solvent considerably cools down the gas temperature and influences the gas velocity. However, the amount of cooling, location of the cooling and consequent reduction in the gas velocity depend heavily on the type of solvent and solvent mixture ratio: organic solvent or mixture with high percentage of that has less effect on the gas dynamics, whereas aqueous solution has a higher impact on the gas temperature and velocity.

Another important phenomenon that might be affected by the droplets injection is the gas Mach number. The coating particle velocity can be directly affected by the gas Mach number. Figure 4.8 shows the gas Mach number before and after injection along the gun centreline axis. The numerical results indicate that the gas Mach number after injection is almost identical to single phase simulation especially after the throat, where there exist sock diamonds. This means that droplets injection either in the forms of single or multicomponent has no effect on the gas Mach number.

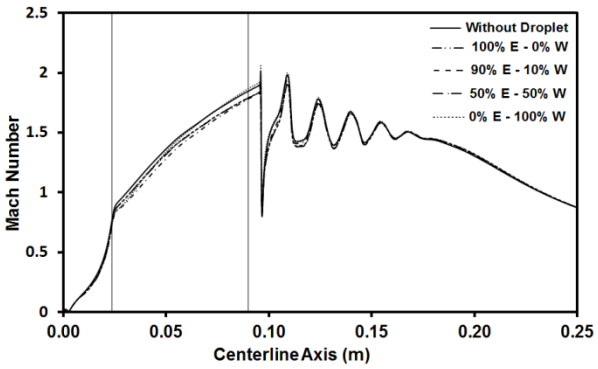

Figure 4-8: Profile of gas Mach number for Without Droplet case and cases with droplets carrying different percentages of Ethanol-Water in solvent along the centerline

It should be noted that in the original design of the DJ 2700 gun the gas carrier tube is located at the centre of the O/F mixer surrounded by annular O/F inlets. That means there is a recirculation zone close to the back wall at the injection area. For this reason the particles start to spread out near the nozzle throat where the flame front converges towards the axis of the torch and interacts with the droplets. Moreover, it

should be mentioned that the validity of these results stands only for a uniform diameter droplets distribution injected into the HVSFS jet. In practice, droplets are injected in a spray cone with an extensive range of droplet diameters. This along with the velocity oscillations of the unsteady HVSFS jet, may create droplets anywhere in the domain from sub-microns to tens of microns in diameter. Also these results are only valid for droplets with diameter 300 μm, as smaller droplet may evaporate faster but resistive to breakup.

4.3 Conclusion

In this numerical investigation three types of solvent in the HVSFS process were investigated, namely: pure ethanol, mixed ethanol and water, and pure water. The solvent fragmentation, evaporation and HVSFS gas dynamics are methodically analysed. The results of this work can be used as a reference for avoiding extraneous trial and error experimentations. It can assist in adjusting the spraying parameters for different powder materials and it can provide a means of visualization of the phenomena taking place during liquid spray. The particle in-flight heating can be effectively controlled by altering the solvent composition, while the temperature and velocity of the exhaust gases can be pitched at the appropriate level in the same way.

Organic solvent or mixture with high percentage of combustible species experience rapid evaporation due to the lower boiling point, while solvent containing aqueous solution or mixture with high aqueous percentage undergoes slower evaporation. Since large relative velocities between liquid droplets and gas phase are developed in the combustion chamber, the aerodynamic break up of particles is more pronounced. Pure ethanol solvent or multicomponent droplets with higher percentage of ethanol leave the combustion chamber with an average size of (5 μm) due to lower surface tension. Full evaporation is achieved before the gun exit. In contrast, those droplets with high surface tension pass through the convergent-divergent section with a diameter larger than 10 μm. When the relative liquid/gas velocity becomes smaller the droplets evaporate and release the nanoparticles far from the gun exit.

The process of droplet evaporation and breakup has a significant influence on the HVSFS gas dynamics. In cases of multicomponent droplets of high percentage of organic solvent less cooling is observed. The spontaneous temperature drop upon injection is effectively recovered after secondary (solvent/oxygen) combustion. Large

disruption of the gas velocity is prevented mainly due to the limiting cooling effect which allows for high pressure build-up in the combustion chamber.

5 Effects of Nanoparticles on Liquid Feedstock Behaviour

The HVOF suspension spraying process involves complex stages of droplet fragmentation, liquid droplet evaporation, nanoparticle agglomeration and nanoparticle/gas heat transfer coupling. The lack of experimental data and quantitative analyses of the internal regions of the torch makes modelling and numerical methods valuable tools for understanding the overall physics of the process by overcoming the technical constraints imposed by the experiments. Most importantly, in such a multidisciplinary process chemico-physical parameters are closely linked and make effective control of the process very challenging [85-86]. Composition of suspension feedstock, for example percentage of nanoparticles in the liquid solvent, is one of the most important parameters that affect the system outcome. In the HVOF suspension spraying process the concentration of suspended solid nanoparticles in the solvent may vary from one case to another, depending on the application. The thermo-physical properties of suspension such as density, viscosity, specific heat, thermal conductivity and surface tension do not remain constant but differ according to nanoparticle concentration [55-60]. In addition, rate and final location of droplet evaporation in a thermal spray torch is critically governed by the physical properties of the solvent. The aim of this work is to analyse the influence of nanoparticle concentration and droplet diameter on the vaporization rate, the secondary breakup of the liquid phase, and the HVOF suspension spraying gas dynamics. The numerical analysis for this study consists of modelling pre-mixed (oxygen/propane) and non-premixed (oxygen/ethanol) combustions, interaction between gas and liquid phases (two-way coupling), secondary break-up and vaporization of droplets. Moreover, for modelling the suspension, the thermo-physical properties are calculated from the theoretical models.

5.1 Model Description

5.1.1 Effect of suspension

To model the suspension, the effect of Nano-size particles on the liquid phase is considered as the change in the liquid bulk density, viscosity, specific heat, thermal conductivity, and surface tension. The density of suspension is defined as (Equation 5.1) [54]:

$$\rho_{susp} = (1 - C)\rho_l + C\rho_d \tag{5.1}$$

where ρ_l and ρ_d are densities of liquid and solid particles respectively. C is solid nanoparticle concentration.

In this study the titania powders are considered to have a density of 4230 kg/m^3. Since the dissolved powder content is not charged into the suspension and instead its thermo-physical properties are calculated by the theoretical models, discussing the type and size distribution of the nanoparticles is of less significance and it will be neglected in this work.

For modelling the viscosity of suspension, Einstein's formula is restricted for the low volume concentrations (up to 3% by weight) { $\mu_{susp} = \mu_l(1 + 2.5C)$} and it was modified by Brinkman for higher concentrations (>10 wt. %) [96]:

$$\mu_{susp} = \frac{\mu_l}{(1-C)^{2.5}}, \tag{5.2}$$

where μ_l is viscosity of liquid.

Specific heat is defined as [56]:

$$c_{susp} = Cc_p + (1 - C)c_l, \tag{5.3}$$

where c_p and c_l are specific heat of particles and liquid respectively.

Experimental analyses have shown that thermal conductivity (k_{susp}) of nano-fluids increases with nanoparticle concentration. This also depends on size, shape and temperature of suspended particles [56, 60]. For thermal conductivity of spherical nanoparticles the Bruggeman model gives better prediction [97] than other models with no limitation on the concentration.

$$k_{susp} = \frac{1}{4}\left[(3C - 1)k_p + (2 - 3C)k_l\right] + \frac{k_l}{4}\sqrt{\Delta}, \tag{5.4}$$

$$\Delta = \left[(3C-1)^2\left(\frac{k_d}{k_l}\right)^2 + (2-3C)^2 + 2(2+9C+9C^2)\left(\frac{k_d}{k_l}\right)\right], \quad (5.5)$$

where k_p and k_l are thermal conductivities of particles and liquid respectively.

It has been reported [58-59] that surface tension of an ethanol based suspension is almost the same as pure ethanol for low particle concentrations (up to 3 wt. %). However, a ten percent increase was observed for a suspension with higher volume concentrations (>10 wt. %). This is due to an augmentation in the Van der Waals forces between nanoparticles at the interface of liquid and gas, which leads to higher surface tension in the suspension. In this study, a ten percent increase in surface tension is considered for suspension with high concentrations (15 and 25 wt. %).

The suspension properties are calculated from commonly used theoretical models and temperature dependent pure liquid properties are incorporated [95] and curve-fitted procedure is applied in their temperature range as shown in Table 5.1.

5.2 Numerical Results and Discussion

This section addresses how the HVOF suspension spraying gas dynamics, rate of evaporation and secondary break up of liquid droplets are affected by the addition of nanoparticles into the liquid feedstock. A uniform surface type injection scheme is used in this study. For this scheme, three different constant diameters and Rosin-Rammler distribution are considered, where each case (liquid droplet) is investigated with four different nanoparticle concentrations (0, 5, 15, and 25wt. %). In this scheme, streams of liquid droplets are released axially from a surface and the solver simulates the interaction of droplets with the combustion gases along the central axis of the torch as droplets move along the axis. In the Rosin-Rammler size distribution, the mass fraction of droplets diameter greater than 'd' is given by:

$$Y_d = e^{-(d/\bar{d})^n}, \quad (5.6)$$

where $\bar{d}$ is the size constant 'Mean Diameter' and n is the size distribution parameter 'Spread Parameter' [98]. Without Droplets (Case-1) in the text and figures refers to a case in which droplets are not injected and only the gas dynamics of the HVOF suspension spraying process is analysed.

Property	Mass Fraction				Temper-ature range K
	0 wt%	**5 wt%**	**15 wt%**	**25 wt%**	
Density kg/m³	$\rho_{susp} = aT + b$ $a = -0.97$ $b = 1077$	$\rho_{susp} = aT + b$ $a = -0.92$ $b = 1234$	$\rho_{susp} = aT + b$ $a = -0.83$ $b = 1550$	$\rho_{susp} = aT + b$ $a = -0.73$ $b = 1865$	300-360
Viscosity kg/m-s	$\mu_{susp} = aT + b$ $a = -1.72 \times 10^{-5}$ $b = 6.36 \times 10^{-3}$	$\mu_{susp} = aT + b$ $a = -1.96 \times 10^{-5}$ $b = 7.23 \times 10^{-3}$	$\mu_{susp} = aT + b$ $a = -2.59 \times 10^{-5}$ $b = 9.55 * 10^{-3}$	$\mu_{susp} = aT + b$ $a = -3.54 \times 10^{-5}$ $b = 1.31 \times 10^{-2}$	273-348
Specific heat J/kg-K	$c_{susp} = aT + b$ $a = 11.02$ $b = -873.8$	$c_{susp} = aT + b$ $a = 10.47$ $b = -641.1$	$c_{susp} = aT + b$ $a = 9.37$ $b = -175.7$	$c_{susp} = aT + b$ $a = 8.27$ $b = 289.7$	300-360
Thermal conductivity W/m-K	$k_{susp} = aT + b$ $a = -2.64 \times 10^{-4}$ $b = 2.46 \times 10^{-1}$	$k_{susp} = aT + b$ $a = -3.04 \times 10^{-4}$ $b = 2.85 \times 10^{-1}$	$k_{susp} = aT + b$ $a = -4.27 \times 10^{-4}$ $b = 4.15 \times 10^{-1}$	$k_{susp} = aT + b$ $a = -6.07 \times 10^{-4}$ $b = 6.90 \times 10^{-1}$	273-373
Surface tension N/m	$\sigma_{susp} = aT + b$ $a = -8.32 \times 10^{-5}$ $b = 4.68 \times 10^{-2}$	$\sigma_{susp} = aT + b$ $a = -8.32 \times 10^{-5}$ $b = 4.68 \times 10^{-2}$	$\sigma_{susp} = aT + b$ $a = -9.16 \times 10^{-5}$ $b = 5.15 \times 10^{-2}$	$\sigma_{susp} = aT + b$ $a = -9.16 \times 10^{-5}$ $b = 5.15 \times 10^{-2}$	283-323

Table 5-1: Thermo-physical properties of pure liquid and suspension

5.2.1 Gas Dynamics and Vaporization Rate of Droplets

5.2.1.1 Injection of Droplets of Constant Sizes

Three cases (Case-2.1, Case-2.2, and Case-2.3) with diameters of 50, 150, and 300 µm, respectively, are selected to analyse the HVOF suspension spraying gas dynamics and vaporization rate of the suspension, see Table 5.2. Droplets in Case-2.1 are inject-

	Injection Diameters		
Constant diameters	50 µm. *Case-2.1*	150 µm. *Case-2.2*	300 µm. *Case-2.3*
Rosin-Rammler distribution	30 µm, 40 µm, 50 µm, 60 µm, 70 µm. *Case-2.4*	130 µm, 140 µm, 150 µm, 160 µm, 170 µm, *Case-2.5*	280 µm, 290 µm, 300 µm, 310 µm, 320 µm, *Case-2.6*

Table 5-2: Injection Diameters for the HVOF suspension spraying process

ed into the HVOF suspension spraying flow at a velocity of 15 m/s, whereas in the two latter cases the injection velocity is 30 m/s. The initial mass flow rate for all cases is specified to be 0.1 g/s. These values for injection velocity and initial mas flow rate are selected based on our previous parametric investigation which was aimed to explore optimum operating parameters for the HVOF suspension spraying process

[92]. The numerical results revealed that injection velocity increases to some extent with droplet diameter and this is probably due to fact that higher injection force is required for larger droplets in order to penetrate them into the HVOF jet. The initial temperature of the droplets is assumed to be 300 K. Each case is simulated with four different solid particle concentrations; namely 0, 5, 15, and 25wt. %.

Figure 5.1(a-c) shows the temperature and velocity profile of the HVOF suspension spraying flow including the vaporization rate of the suspension with a diameter of 50 micron along the centreline axis. From this figure, the maximum cooling effect or temperature difference due to the liquid ethanol droplet evaporation for the cases at the ends: 0wt. % and 25wt. % are found to be approximately 1400K and 1050K in the CD section, respectively, compared to Without Droplet Case-1 (Figure 5.1-a). Thus the maximum temperature difference between the cases is 350 K. This, also, occurs after convergent-divergent section but with opposite trend. However, the velocity difference between the cases is not considerable because the amount of cooling is not high enough to change the pressure and the velocity. Figure 5.1-c shows that the gas temperature cooling in the HVOF suspension spraying process is directly related to the droplet vaporization rate, which means the lower the evaporation rate, the less gas temperature cooling and vice versa. Moreover, Figure 5.1-c shows the highest vaporization rate of 1.83×10^{-7} Kg/s for the homogenous droplets, while the addition of 25 wt. % nanoparticles into the base fluid (ethanol) reduces it by 20%. As can be seen from the aforementioned figure, the maximum rate of evaporation occurs inside the combustion chamber for all the cases, while the final location of evaporation stretches to the gun exit when droplets are loaded with higher concentrations. The reason for this is that at the beginning dense droplets with higher specific heat are slow to vaporize, then due to the growing higher relative velocities between the phases they disintegrate and evaporate with delay compared to those with less density and lower specific heat. This can be supported with the vaporization laws which are used to model droplets evaporation and mass transfer to the continuous phase.

However, when droplets are injected with a diameter of 150 µm and, again, four different nanoparticle concentrations, the maximum temperature difference between the cases at the ends: 0wt. % and 25wt. % is almost 250 K before the convergent-divergent section, see Figure 5.2-a. A significant difference in the evaporation rate of droplets is observed inside the combustion chamber for the studied cases. The highest

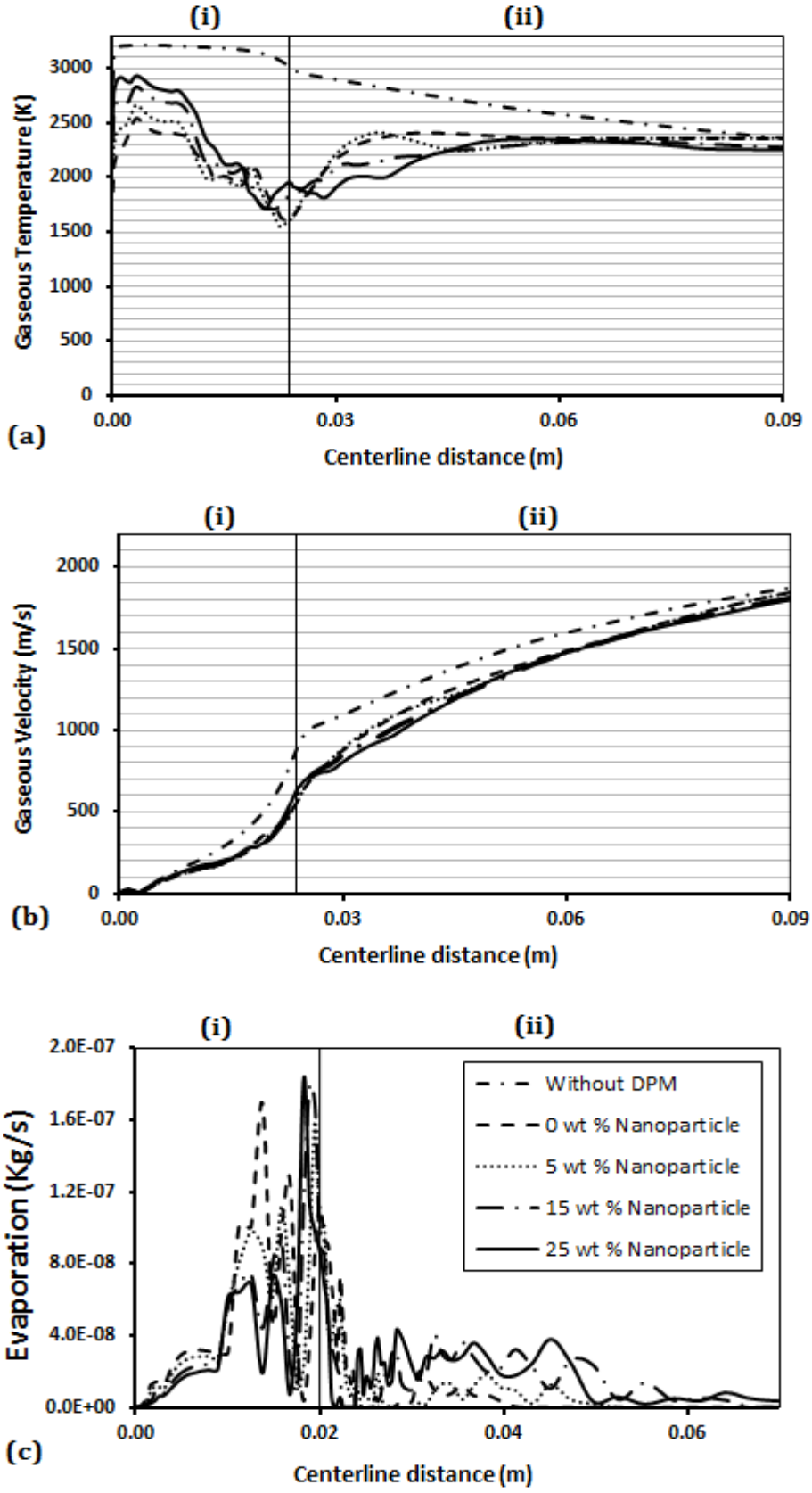

Figure 5-1: Comparison of the (a) gas temperature, (b) velocity fields, and (c) rate of evaporation experienced by the droplets injected from a surface with constant diameters of 50 µm and having various solid nanoparticle concentrations

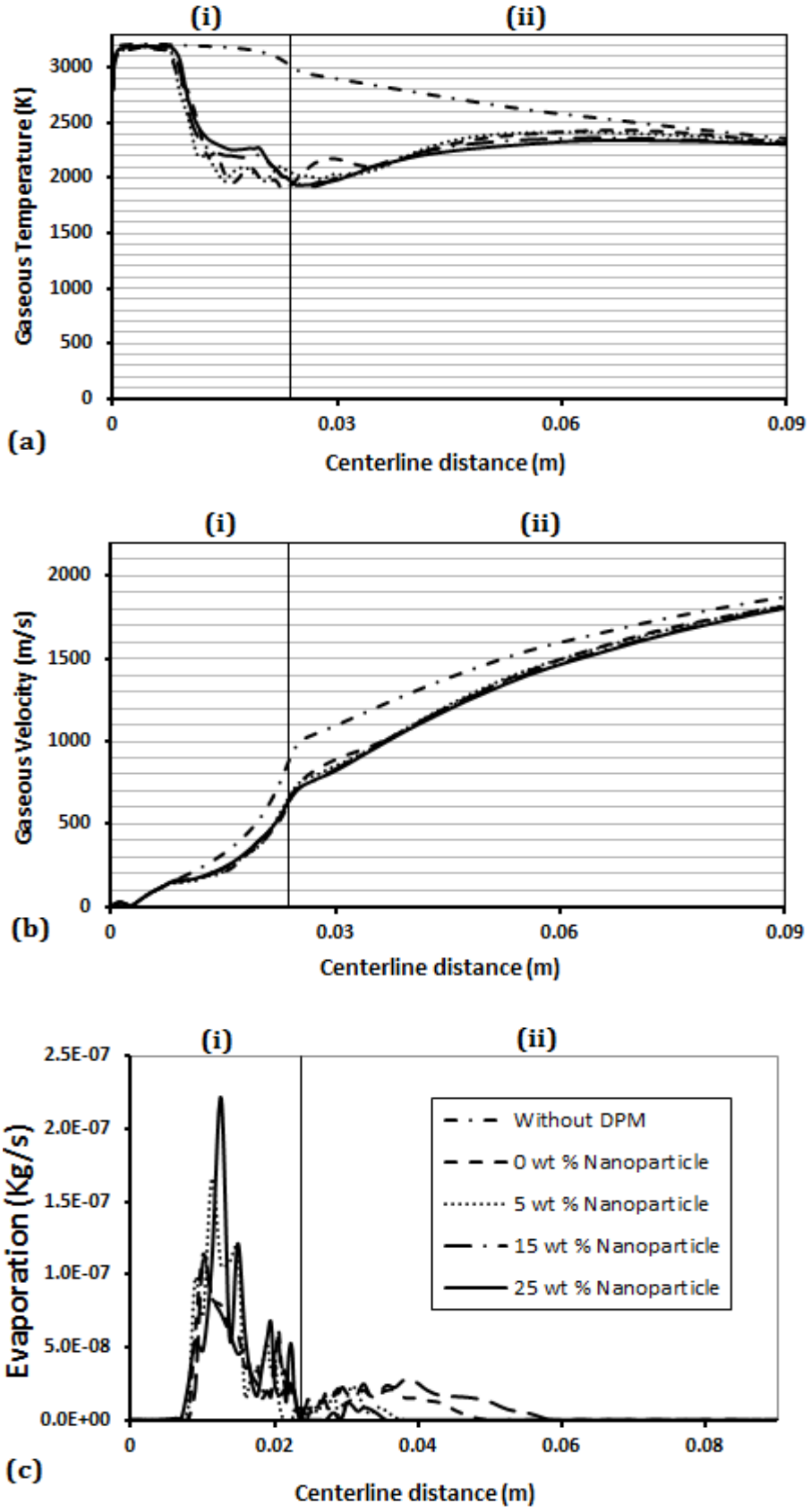

Figure 5-2: Comparison of the (a) gas temperature, (b) velocity fields, and (c) rate of evaporation experienced by the droplets injected from a surface with constant diameters of 150 µm and having various solid nanoparticle concentrations

and lowest rates $1.54 \times 10^{-7}$and 9.52×10^{-8} Kg/s stand for droplets with 0wt. % and 25wt. % concentrations respectively (see Figure 5.2-c). Compared to Case-2.1, 15% decrease in the evaporation rate of droplets is noted for the Case-2.2 which shows that increasing the size of injection droplets can reduce vaporization of liquid feedstock.

In the last case (Case-2.3) where the droplet diameter is raised to 300 µm, the maximum gas temperature difference along the centreline between the cases (0 wt. % and 25 wt. %) reaches 460 K in the combustion chamber, while it reaches almost 100 K inside the barrel, and at the gun exit the temperature difference among all cases is negligible. The velocity difference for different concentrations is not considerable in Case-2.3. A similar trend is observed for droplet vaporization rate compared to the above case (Case-2.2) but the difference in the evaporation rate for varied nanoparticle loadings is further reduced. This is due to the increase in droplets Weber number which intensifies droplets deformation and leads to severe atomization and decreases the vaporization process. These results are not illustrated in any Figure to avoid repeating.

5.2.1.2 Injection of Droplets of Various Sizes Distribution

In this section, droplets with Rosin-Rammler diameter distribution and four different nanoparticle concentrations (0, 5, 15, and 25wt. %) are injected into the HVOF suspension spraying flow from an inlet surface (see Table 5.2). In Case-2.4, five streams of droplets with varied diameters 30, 40, 50, 60, and 70 µm are injected at the same time from an inlet surface. The case is examined with four different nanoparticle concentrations. Figure 5.3-a shows a comparison of temperature difference between Without Droplets (Case-1) and Case-2.4. As can be seen, the temperature difference between (Case-1) and Case-2.4 with high nanoparticle loading (25wt. %) is 145 K, while this is 850 K close to the nozzle entrance for Case-2.4 with low particle loading (0wt. %). This is a further temperature loss for droplets with low particle loading as compared with Case-2.1 which confirms that the cooling effect for varied diameter droplets is higher than for the constant diameter droplets. Figure 5.3-b shows that the reduction in the gas velocity is more for this case as compared with Case-2.1. This is 165 and 220 m/s for the cases at the ends (0 and 25 wt. %) compared to Case-1 and Case-2.4. The reason for this is the higher cooling effect and the variation in droplet size from 30 µm to 70 µm. In this case every droplet has a different evaporation rate

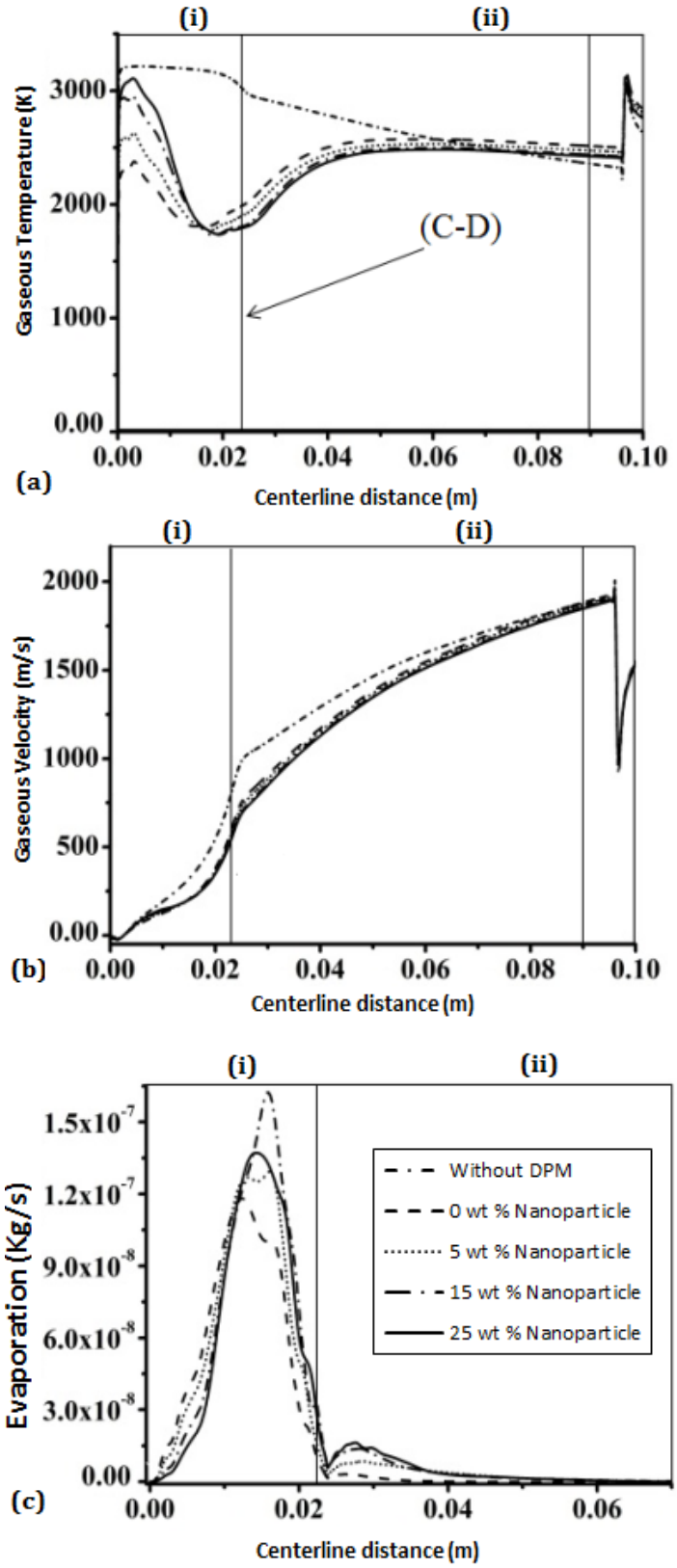

Figure 5-3: Comparison of the (a) gas temperature, (b) velocity fields, and (c) rate of evaporation experienced by the droplets injected from a surface with various diameters of 30 µm, 40 µm, 50 µm, 60 µm, 70 µm and having various solid nanoparticle concentrations

and moves with different relative velocity inside the torch. The evaporation rate for the ends cases (0 and 25 wt. %) is calculated to be 1.2×10^{-7} and 1.36×10^{-7}Kg/s along the centreline axis. The cause of fluctuation in the rate of evaporation is due to different sizes of droplets carrying different masses. The extra loss or cooling of the gas temperature, as droplets of various diameters are injected, reveals that the rate of vaporization is also dependent on the droplets injection diameter. For smaller droplets (30 µm, 40 µm), higher evaporation occurs inside the combustion chamber while larger diameter droplets (60 µm, 70 µm) are evaporated in the barrel.

When droplets are injected with diameters 130, 140, 150, 160 and 170 µm (Case-2.5), the trend for the gas temperature cooling is changed. Here the temperature difference between 0wt. % and 25wt. % nanoparticles loading is 550K in the middle of the combustion chamber and it decreases to 100K along the barrel centreline axis (Figure 5.4-a). In Figure 5.4-b the velocity field does not experience any significant changes and shows the same pattern as observed for the Case-2.2. Calculated vaporization rate for the sub cases (0 and 25 wt. %) of Case-2.5 is $1.40 \times 10^{-7}$and 7.67×10^{-8} Kg/s respectively (Figure 5.4-c). Further analysis reveals that there is a decrease in the overall evaporation rate along the gun axis by 9% for 0wt. % nanoparticle-loading and 19% for 25wt. % concentration compared with Case-2.2 (constant diameter). The final location of droplets evaporation moves from the C-D nozzle toward the middle of barrel as the nanoparticle concentration is increased from 0, to 5 wt. %. Furthermore, the droplets leave the gun without complete evaporation when the concentration of nanoparticles increases from 15 to 25 wt. % (Figure 5.4-c).
In Case-2.6, when a range of droplets diameters from 280, 290, 300, 310, and 320 µm are injected into the HVOF suspension spraying flow, no significant variations are observed as compare with constant diameter injection (300 µm) Case-2.3 which confirms that all these droplets have a similar trend of gas cooling and rate of evaporation.

In summary, droplet evaporation depends principally on two parameters i.e. nanoparticles concentration, and droplets diameter. As the droplets size and nanoparticles concentration increase, the rate of evaporation decreases. Also an increase of vaporization rate is observed for varied diameters 30 to 70 µm (Case 2.4) compared to constant diameter 50 µm (Case-2.1). However, for the second and third set of varied diameters 130 to 170 and 280 to 320 µm, the effect is opposite due to

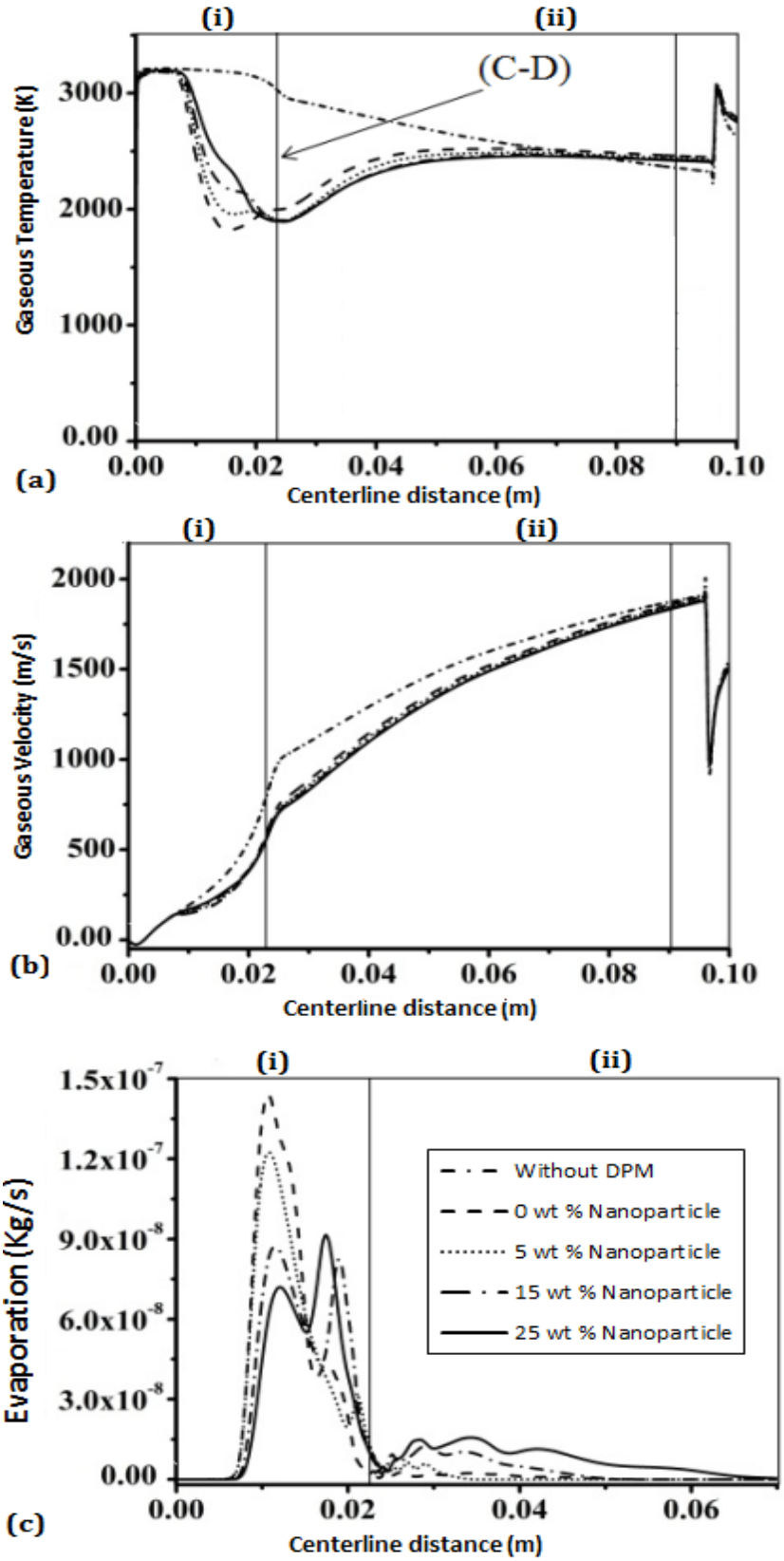

Figure 5-4: Comparison of the (a) gas temperature, (b) velocity fields, and (c) rate of evaporation experienced by the droplets injected from a surface with various diameters of 130 µm, 140 µm, 150 µm, 160 µm, 170 µm, and having various solid nanoparticle concentrations

increased droplet size. It can be concluded that increasing nanoparticle concentration in suspension droplets with various and large diameters would decrease the amount of droplets evaporation.

5.2.2 Secondary Break-up

For this analysis, droplet streams with constant diameters are selected and their diameter reduction and final location of evaporation are highlighted. Furthermore, for Rosin-Rammler distribution, a set of five streams (only one case) is investigated.

5.2.2.1 Injection of Droplets of Constant Sizes

A comparison of droplets diameter reduction is shown in Figure 5.5 (a-b) for the two sub cases of the Case-2.1. This demonstrates secondary break up and reduction in diameter of 50 µm droplets with two different solid nanoparticles concentrations. It shows that droplets experience a sharp decrease in their diameter from 46 to 19 and 12 to 8 micro-meters approximately for all nanoparticles concentration variations. In Case-2.1, We reach a peak value of almost 12 due to the growing relative velocities between the droplets and gas phase in the combustion chamber, where the main atomization occurs. However, the value of We remains below 14 for all the Nano-loadings. Hence the break up type is vibrational. In this case, even the addition of the solid nanoparticles into the droplets does not affect the disintegration process. Therefore, the vaporization of the droplets is the dominant factor and controls the process when droplets are injected with small and constant diameter of 50 µm.

In contrast, as the diameter of the droplets is raised to 150 µm (Case-2.2), the We varies between 25 and 30 based on the nanoparticle concentration in the droplets and severe fragmentation occurs in the middle of the combustion chamber. This is also reflected by the reduction of droplets diameter from 150 to 35 and 32 to 15 inside the combustion chamber, see Figure 5.5(c-d). For all the studied concentrations, droplets are evaporated in the middle of barrel and release solid nanoparticles, but with the highest concentration (25wt. %) a delay occurs in the rate of evaporation and cause the droplets to reach the nozzle outlet. Similar results are observed for larger droplets (300 µm) while the We increases from 50 to 70 for Case-2.3. The above analysis indicates that the fragmentation process is dominant for large droplets (150 and 300

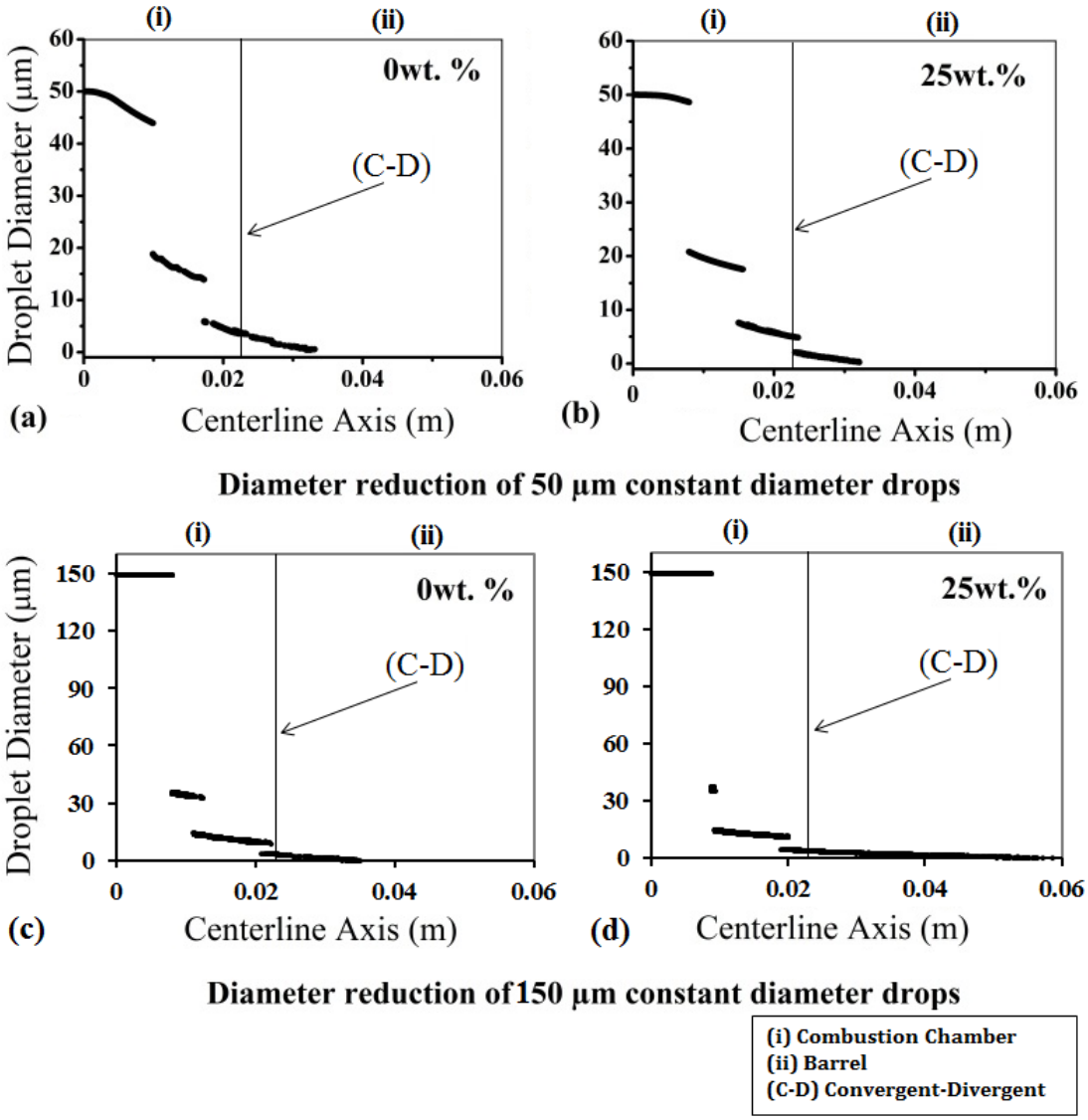

Figure 5-5: Comparison of the droplets diameter reduction with a constant diameter of (a-) 50 µm, and (c-d) 150 µm and having 0 and 25wt. % nanoparticle concentrations

µm) while the rate of evaporation is higher for small droplets (50 µm).

Finally, Figure 5.6(a-d) compares the evaporation rate of droplets with diameters of 50 and 150 µm, and with 0 and 25wt. % nanoparticle concentrations as they are injected from an inlet surface. In this figure, significance of fragmentation and evaporation in the HVOF suspension spraying process is evident. It shows that larger droplets (150 µm) with high concentration (25wt. %) leave the gun without complete vaporization, which can lead to serious consequences in real applications and can create defects in coatings. It can be inferred that by increasing the concentration of nanoparticles in the base fluid, the rate of evaporation decreases causing the delay in

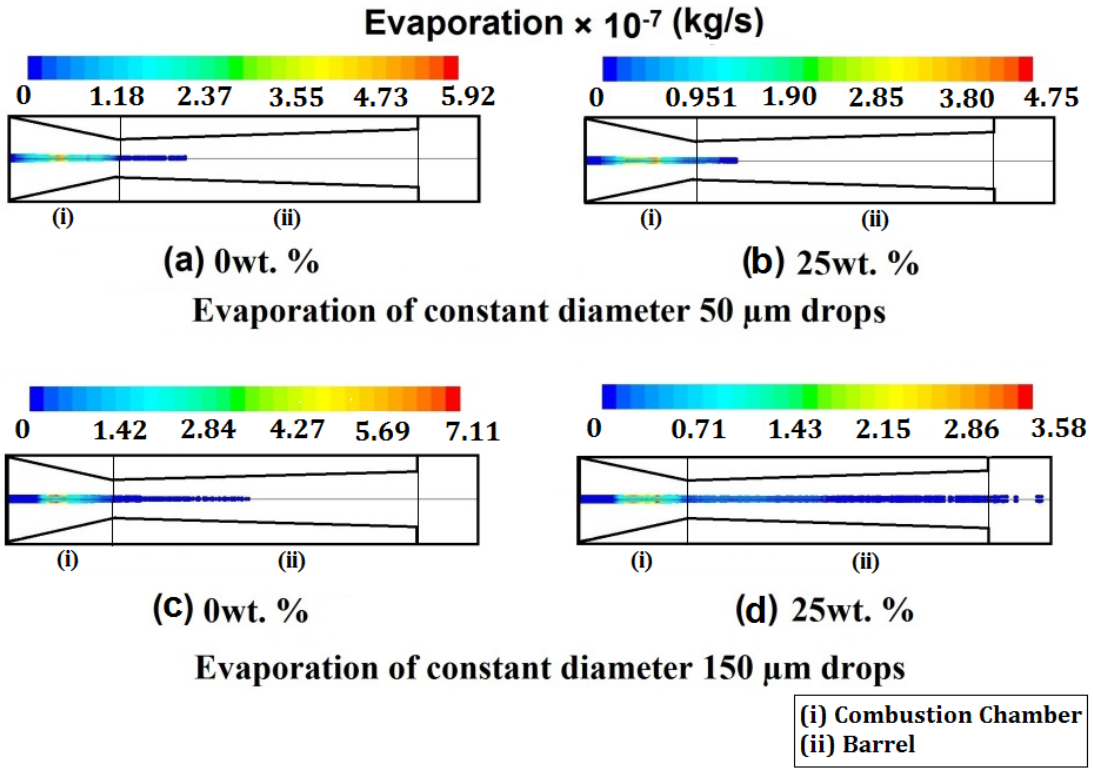

Figure 5-6: Comparison of evaporation rate of the droplets with constant diameters of (a-b) 50 µm and (c-d) 150 µm, each with 0 and 25 wt. % nanoparticle concentrations

the complete vaporization of the droplets. However, simulation results reveal that droplets with the smaller diameter are evaporated in the middle of the barrel and consequently release nanoparticles. This may suggest that smaller droplets can be used in applications where nanoparticles with a high melting point are required for coatings. It should be noted in the present work only the employed models are validated with experimental data and the results are predicted by the models [35-36, 90-91]. Therefore, experimental studies are demanded to validate the findings.

5.2.2.2 Injection of Droplets of Various Sizes Distribution

Considerable reduction in diameter is observed for Case-2.4, when droplet streams with five different diameter distribution (30, 40, 50, 60 and 70 µm) and four different concentrations are injected into the gun (Figure 5.7(a-b)). The degree of disintegration is dependent on the initial size of droplets. For example, the breakup in the small droplets of 30 µm leads to a reduction from 20 to 14 and 14 to 7 micro-meters, while in the large droplets of 70 µm the reduction is from 66 to 30 and 30 to 24 micrometers. In this case, the fragmentation is higher for the droplets greater than 50 micron and

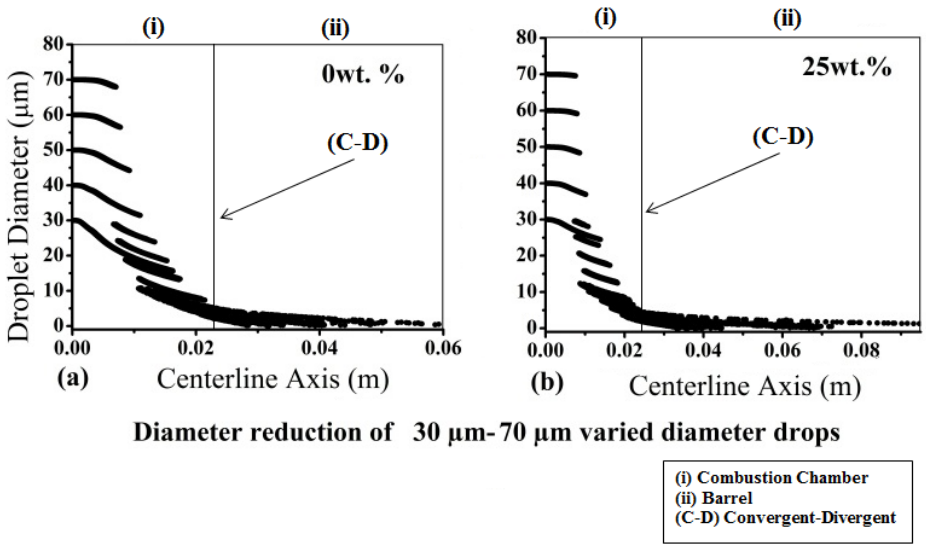

Figure 5-7: Comparison of the droplets (a-b) diameter reduction, with various diameters of 30 µm, 40 µm, 50 µm, 60 µm, 70 µm and having 0 and 25wt. % nanoparticle concentrations

lower for those droplets less than 50 micron. Droplets fragmentation is observed at different positions and it is hardly distinguishable at higher positions (> 0.02 m) in the graph due to the simultaneous injection of droplets with varied sizes and overlapping at higher positions. The value of the Weber number stays below 14 for different concentrations and the breakup type is vibrational as observed for the constant diameter droplets of 50 µm (Case-2.1).

When droplets with various sizes from 130 to 170 µm are injected (Case-2.5), 71% reduction is noticed in their size for the four different concentrations. For these cases, the We fluctuates between 26 to 35 and severe fragmentation is observed inside the combustion chamber. The maximum reduction of 85% in the droplets diameter is observed as they are injected in a range of 280 to 320 micron. Moreover, We increases from 55 to 80 proving that the large droplets experience intensive fragmentation inside the combustion chamber. When the Rosin-Rammler diameter distribution is applied, more droplets discharge through the torch without prior evaporation and this complication becomes intense with increasing nanoparticle concentration in the droplets.

In summary, if injection of droplets with small sizes (diameter $\leq$ 50 µm) is favoured in an application, extra liquid surfactant should be added to the suspension to reduce the droplets surface tension and intensify the fragmentation process. However, with regard to droplets atomization in the HVOF suspension spraying

process, larger droplets undergo severe break up with less evaporation rate when carrying higher nanoparticle concentrations. To increase the effectiveness of the HVOF suspension spraying process when injecting large droplets, an optimum addition of nanoparticles into the solvent is required. In the group type injection, proper selection of the injection angle, initial velocity and diameter distribution are demanded to achieve optimum results.

It should be noted that in the original design of the DJ 2700 gun, the gas carrier tube is located at the centre of the back wall and it is surrounded by annular oxygen/fuel (O/F) inlets. It creates a recirculation zone close to the back wall at the injection area and the particles start to spread out near the nozzle throat where the flame reaches the axis of the torch and interacts with the droplets. It can be anticipated when the droplets are injected at an angle of 45°, they are directed towards the core of the combustion chamber core where they have a close interaction with the flame, which makes the evaporation process more effective in this injection scheme. In this method one has to control the injection parameters to avoid the droplets colliding with the combustion chamber walls. Moreover, even though the employed models in the present work can be applied to liquid-fuelled HVOF guns, the numerical model must include further evaporation from a combustion-driven liquid fuels such as kerosene or liquid propane and its interaction. Therefore, it is highly unlikely these results match with that of liquid-fuelled HVOF torches.

5.3 Conclusion

The effects of the solid nanoparticles on the liquid droplets in the suspension are considered as the change in the liquid bulk thermo-physical properties. Then effects of suspension on the gas dynamics, vaporization rate, and secondary break up in the HVOF suspension spraying process are investigated. The main findings are:

- There is a considerable difference in the final location of evaporation of homogeneous and non-homogeneous droplets. This is an important factor in the numerical analysis of suspension as nanoparticles are created in a computational domain as new entities.

- If a high concentration loading in a suspension is favoured in an application, the use of smaller droplets (up to 50 µm) give a better result as they experience high evaporation in the mid-section of the nozzle.
- If larger droplets (150 and 300 µm) are injected into the gun, fragmentation is the dominant factor which controls the process. With increasing solid particle concentrations in the droplets the final location of evaporation moves towards the gun exit and in the extreme cases the droplets leave the gun without complete evaporation.

6 Heat Transfer in Nanostructured Thermoelectrics

When an electrical current passes across a junction of two dissimilar materials, Peltier effect occurs by the emission or absorption of heat while the Joule heating occurs volumetrically over the thermoelectric elements. The Joule heating takes longer than the Peltier cooling to affect the temperature at the cold side due to finite heat diffusion time. These two cooling effects at steady state conditions along with heat conduction from the hot end to the cold end determine the cold side temperature. The cooling coefficient of performance and maximum temperature drop of the thermoelectric materials are confined by its dimensionless thermoelectric figure of merit $ZT = S^2\sigma T/K$, where S is the Seebeck coefficient, T is the absolute temperature, K and σ are the thermal and electrical conductivities, respectively. If an additional current pulse is applied on the original optimal current, which is the current to obtain the minimum steady state cold side temperature, an instantaneously lower temperature than that reachable at the steady state can be produced at the cold side due to delay of the thermal diffusion of the volumetric Joule heat. This is called the transient thermoelectric effect [91]. The transient cooling effect in thermoelectric (TE) elements has been extensively studied [92-102] after Stilbans and Fedorovich [103] first reported it. A comprehensive review of thermoelectric cooling can be found in [104].

Thermal energy transport at scales comparable to phonon mean free path is a key factor to enhance thermoelectric devices. Heat transfer at this scale is significantly different from that in macro-scales due to size effects on heat carriers, boundary and interface scattering, the finite relaxation time of heat carriers, and the ballistic nature of the transport. In this chapter, the transient ballistic-diffusive heat conduction equations (BDE),as an approximation to the phonon Boltzmann equation (BTE), and hyperbolic heat equation (HHC) are solved numerically and applied to the problem of transient heat conduction across a thin film. Both the diffusive part of the BDE and HHC are solved with a stable and convergent finite difference method. The ballistic part of the BDE is solved with the Gauss-Legendre integration scheme. Finally, these equations are applied across a thermoelectric thin film to investigate the steady-state

and the transient cooling mechanism at the cold side boundary. Background information about the thermoelectric materials can be found in Chapetr2.

6.1 Mathematical Modelling

6.1.1 Transient Heat Conduction

6.1.1.1 Hyperbolic Heat Conduction Equation

It is well known that the Fourier's Law of heat conduction $q = -K\nabla T$ with q the heat flux vector, K the heat conductivity and ∇T the temperature gradient is only valid at large space scales and low frequencies. To cope with high frequency processes, Cattaneo and Vernotte have generalized the Fourier's law into the unsteady form [66, 113]:

$$q + \tau \frac{\partial q}{\partial t} = -K\nabla T \tag{6.1}$$

where τ is thermal relaxation time and can be calculated using the thermal wave speed, C_t, and the thermal diffusivity, α, as:

$$\tau \propto \frac{\alpha}{C_t^2} \tag{6.2}$$

Combining Equation 6.1 with energy conservation equation:

$$C \frac{\partial T}{\partial t} + \nabla . q = 0 \tag{6.3}$$

yields the following unsteady hyperbolic heat conduction equation:

$$\tau \frac{\partial^2 T}{\partial t^2} + \frac{\partial T}{\partial t} = \alpha \nabla^2 T \tag{6.4}$$

The thermal diffusivity is $\alpha = K/C$ and C is the volumetric heat capacity. Equation 6.4 is a hyperbolic type partial differential equation and causes the propagation speed reach a limit amount $\sqrt{\alpha/\tau}$, for $\tau > 0$.

For transient heat conduction in one dimension, Equation 6.4 assumes the following form:

$$\tau \frac{\partial^2 T}{\partial t^2} + \frac{\partial T}{\partial t} = \alpha \frac{\partial^2 T}{\partial x^2} \tag{6.5}$$

With the following initial and boundary conditions:

Initial conditions:

$$t = 0, \qquad T(x,0) = 0, \qquad \frac{\partial T(x,0)}{\partial t} = 0 \tag{6.6}$$

Boundary conditions:

$$x = 0, \qquad T(0,t) = 1 \tag{6.7}$$

$$x = L, \qquad T(L,t) = 0 \tag{6.8}$$

To obtain the normalized equations, the following non-dimensional parameters are considered:

$$\theta = \frac{T-T_0}{T_i-T_0} \qquad t^* = t/\tau \qquad \eta = x/L \qquad Kn = l/L \tag{6.9}$$

where l,L, and $\tau$are the mean molecular free path and characteristic length, and the collision time, respectively. Let us also mention that the heat conductivity and the collision time are not independent but, according to the phonon kinetic theory, they are related by

$$K = \frac{1}{3} C\vartheta l \qquad\qquad \tau = l/\vartheta \tag{6.10}$$

wherein ϑ isthe mean velocity of phonons. In addition, we introduced the Knudsen number, $Kn = l/L$, which by virtue of expression (6.10) can be given the more general form:

$$\mathrm{Kn}^2 = 3K\tau/CL^2 \tag{6.11}$$

Equations 6.5-6.8 can be expressed in terms of these dimensionless quantities as:

$$\frac{\partial^2\theta}{\partial t^{*2}} + \frac{\partial\theta}{\partial t^*} = \frac{\mathrm{Kn}^2}{3}\frac{\partial^2\theta}{\partial \eta^2} \tag{6.12}$$

$$t^* = 0, \qquad \theta(\eta,0) = 0, \qquad \frac{\partial\theta(\eta,0)}{\partial t^*} = 0 \tag{6.13}$$

$$\eta = 0, \qquad \theta(0,t^*) = 1 \tag{6.14}$$

$$\eta = 1, \qquad \theta(1,t^*) = 0 \tag{6.15}$$

By taking into account the size effect of micro-scale conduction heat transfer, Alvarez and Jou [114] defined an effective thermal conductivity using extended irreversible thermodynamics as:

$$K(L) = \frac{K_0 L^2}{2\pi^2 l^2}\left(\sqrt{1+\frac{4\pi^2 l^2}{L^2}} - 1\right) \tag{6.16}$$

Using expressions (6.9), (6.10), (6.16), Equation 6.12 is, then, modified to

$$\frac{1}{4}\frac{\partial^2\theta}{\partial t^{*2}} + \frac{\partial\theta}{\partial t^*} = \frac{1}{6\pi^2}\left(\sqrt{1+4\pi^2\mathrm{Kn}^2}-1\right)\frac{\partial^2\theta}{\partial \eta^2} \tag{6.17}$$

Usually, instead of the normalized effective time τ_{eff}, one directly considers τ and the factor $\frac{1}{4}$ does not appear in the first term. In a recent research work, a diffusive time scale is defined using the device properties as:

$$\tau_d = \frac{\pi^2 L^2 C(L)}{4K(L)} \tag{6.18}$$

Which changes Equation 6.17 into:

$$\varphi\frac{\partial^2\theta}{\partial t^{*2}} + \frac{\partial\theta}{\partial t^*} = \frac{\pi^2}{4}\frac{\partial^2\theta}{\partial \eta^2} \tag{6.19}$$

Where the dimensionless coefficient $\varphi = \tau_{eff}/\tau_d$.

6.1.1.2 Ballistic-Diffusive Heat conduction Equations

Ballistic-diffusive heat conduction equations are a good approximation of the phonon Boltzmann equation under the relaxation time approximation. In these equations, there exists the coexistence of two kinds of heat carriers: ballistic phonons originating at the boundaries and experiencing mainly collisions with wall and diffusive phonons that undergo multiple collisions within the core of the system. Therefore, the heat flux and the internal energy are decomposed into a diffusive and a ballistic component as:

$$q = q_b + q_d \qquad \text{and} \qquad u = u_b + u_d \tag{6.20}$$

The local temperature is considered as a measure of the local internal energy. Subsequently, diffusive temperature $T_d = u_d/C$, ballistic temperature $T_b = u_b/C$,and total temperature $T = T_d + T_b$ are introduced. The transient ballistic-diffusive heat conduction equations in one dimensional form can be expressed as:

$$\tau\frac{\partial^2 u_d}{\partial t^2} + \frac{\partial u_d}{\partial t} = \frac{K}{C}\frac{\partial^2 u_d}{\partial x^2} - \frac{\partial q_b}{\partial x} \tag{6.21}$$

With the following initial and boundary conditions:

Initial conditions:

$$t = 0, \qquad u(x,0) = u_d(x,0) + u_b(x,0) = CT_0, \qquad \frac{\partial u(x,0)}{\partial t} = 0 \tag{6.22}$$

where T_0 is the initial temperature of a thin film.

Boundary conditions:

$$x = 0\,, \qquad \left(\tau\frac{\partial u_d}{\partial t} + u_d\right) = \frac{2l}{3}\left(\frac{\partial u_d}{\partial x}\right) \quad \text{and} \quad u_{b1} = CT_1 \tag{6.23}$$

At time t=0 and x=0, one surface emits phonons at temperatureT_1.

$$x = L\,, \qquad \left(\tau\frac{\partial u_d}{\partial t} + u_d\right) = -\frac{2l}{3}\left(\frac{\partial u_d}{\partial x}\right) \quad \text{and} \quad u_{b2} = CT_0 \tag{6.24}$$

To determine the ballistic heat flux in Equation 6.21, the boundary heat flux, its derivative, and the internal energy of the ballistic components are introduced as:

$$q_b(x,t) = \begin{cases} \frac{C\vartheta\Delta T}{2}\int_{\mu_t}^{1} \mu e^{-\left(\frac{x}{\mu l}\right)}\, d\mu + q_{b0}(x,0) & \left[0 \le \mu_t = \frac{x}{\vartheta t} \le 1\right] \\ q_{b0}(x,0) & other\ \mu_t \end{cases} \tag{6.25}$$

$$\frac{\partial q_b(x,t)}{\partial x} = \begin{cases} -\frac{C\vartheta\Delta T}{2l}\left(\int_{\mu_t}^{1} e^{-\left(\frac{x}{\mu l}\right)}\, d\mu + \frac{xl}{\vartheta^2 t^2} e^{-\frac{\vartheta t}{l}}\right) + \frac{\partial q_{b0}(x,0)}{\partial x} & (0 \le \mu_t \le 1) \\ \frac{\partial q_{b0}(x,0)}{\partial x} & other\ \mu_t \end{cases} \tag{6.26}$$

$$u_b(x,t) = \begin{cases} \frac{C\Delta T}{2}\int_{\mu_t}^{1} e^{-\left(\frac{x}{\mu l}\right)}\, d\mu + u_{b0}(x,0) & (0 \le \mu_t \le 1) \\ u_{b0}(x,0) & other\ \mu_t \end{cases} \tag{6.27}$$

where $\Delta T = T_1 - T_0$, q_{b0} and u_{b0} are the ballistic terms at equilibrium:

$$q_{b0}(x,0) = \frac{C\vartheta}{2}\left\{E_3\left(\frac{x}{l}\right) - E_3\left(\frac{L-x}{l}\right)\right\} \tag{6.28}$$

$$u_{b0}(x,0) = \frac{u_0}{2}\left\{E_2\left(\frac{x}{l}\right) + E_2\left(\frac{L-x}{l}\right)\right\} \tag{6.29}$$

and $u_0 = CT_0$. Here E_n is the exponential integral function of order *n*.

To obtain the normalized equations, the following non-dimensional parameters are considered:

$$\theta_d = \frac{u_d - u_{d0}}{C\Delta T} \qquad \theta_b = \frac{u_b - u_{b0}}{C\Delta T} \qquad \theta = \frac{u - u_0}{C\Delta T} = \frac{T - T_0}{\Delta T}$$

$$q_d^* = \frac{q_d - q_{d0}}{C\vartheta\Delta T} \qquad q_b^* = \frac{q_b - q_{b0}}{C\vartheta\Delta T} \qquad q^* = \frac{q - q_0}{C\vartheta\Delta T}$$

$$t^* = \frac{t}{\tau} \qquad \eta = \frac{x}{L} \qquad \mathrm{Kn} = \frac{l}{L}, \qquad Kn^2 = 3K\tau/CL^2 \tag{6.30}$$

Equations 6.21-6.27 can be expressed in terms of these dimensionless quantities as:

$$\frac{\partial^2\theta_d}{\partial t^{*2}} + \frac{\partial\theta_d}{\partial t^*} = \frac{\mathrm{Kn}^2}{3}\frac{\partial^2\theta_d}{\partial \eta^2} - \mathrm{Kn}\frac{\partial q_b^*}{\partial \eta} \tag{6.31}$$

$$t^* = 0, \qquad \theta(\eta, 0) = 0 \qquad \frac{\partial\theta(\eta,0)}{\partial t^*} = 0 \tag{6.32}$$

$$\eta = 0\,, \qquad \left(\frac{\partial\theta_d}{\partial t^*} + \theta_d\right) = \frac{2\mathrm{Kn}}{3}\left(\frac{\partial\theta_d}{\partial \eta}\right) \quad \text{and} \quad \theta_{b1} = 1 \tag{6.33}$$

$$\eta = 1\,, \qquad \left(\frac{\partial\theta_d}{\partial t^*} + \theta_d\right) = -\frac{2\mathrm{Kn}}{3}\left(\frac{\partial\theta_d}{\partial \eta}\right) \quad \text{and} \quad \theta_{b2} = 0 \tag{6.34}$$

$$q_b^*(\eta, t^*) = \begin{cases} \frac{1}{2}\int_{\mu_t}^{1} \mu e^{-\left(\frac{\eta}{\mu \mathrm{Kn}}\right)} d\mu & (0 \le \mu_t \le 1) \\ 0 & other\ \mu_t \end{cases} \tag{6.35}$$

$$\frac{\partial q_b^*(\eta,t^*)}{\partial \eta} = \begin{cases} -\frac{1}{2\mathrm{Kn}}\left(\int_{\mu_t}^{1} e^{-\left(\frac{\eta}{\mu \mathrm{Kn}}\right)} d\mu + \frac{\eta}{\mathrm{Kn}t^{*2}} e^{-t^*}\right) & (0 \le \mu_t \le 1) \\ 0 & other\ \mu_t \end{cases} \tag{6.36}$$

$$\theta_b^*(\eta, t^*) = \begin{cases} \frac{1}{2}\int_{\mu_t}^{1} e^{-\left(\frac{\eta}{\mu \mathrm{Kn}}\right)} d\mu & (0 \le \mu_t \le 1) \\ 0 & other\ \mu_t \end{cases} \tag{6.37}$$

6.1.2 Transient Thermoelectric Effect

6.1.2.1 Hyperbolic Heat Conduction across Thermoelectric Thin Films

It is assumed the n-type and p-type thermoelectric elements have exactly the same properties except for the opposite sign of Seebeck coefficient. In this way, the theoretical analysis of the transient cooling of free standing TE element can be approximated into a one dimensional hyperbolic partial differential equation, which in the non-dimensional form reads (see section 6.1.1.1):

$$\frac{\partial^2\theta}{\partial t^{*2}} + \frac{\partial\theta}{\partial t^*} = \frac{\mathrm{Kn}^2}{3}\frac{\partial^2\theta}{\partial \eta^2} + \beta_1 J^{*2} \tag{6.38}$$

or

$$\frac{1}{4}\frac{\partial^2\theta}{\partial t^{*2}} + \frac{\partial\theta}{\partial t^*} = \frac{1}{6\pi^2}\left(\sqrt{1 + 4\pi^2\mathrm{Kn}^2} - 1\right)\frac{\partial^2\theta}{\partial \eta^2} + \beta_2 J^{*2} \tag{6.39}$$

or

$$\varphi \frac{\partial^2 \theta}{\partial t^{*2}} + \frac{\partial \theta}{\partial t^*} = \frac{\pi^2}{4} \frac{\partial^2 \theta}{\partial \eta^2} + \beta_3 J^{*2} \tag{6.40}$$

$$J^* = J/J_0 \qquad \beta_1 = \frac{J^2 \tau}{C^2 \sigma \Delta T} \qquad \beta_2 = \frac{J^2 \tau}{C(L)^2 \sigma \Delta T} \qquad \beta_3 = \frac{J^2 \tau_d}{C(L)^2 \sigma \Delta T} \tag{6.41}$$

where J is the magnitude of the electrical current through the film. The new term in the hyperbolic heat conduction equations represents the Joule heating which occurs in the body of the thermoelectric element. Equation 6.38 assumes a constant thermal conductivity and collision time is used in its nondimensionalization. Both Equations 6.39 and 6.40 are formulated with size-dependent thermal conductivity but they differ in the time unit. Equation 6.39 uses a collision time scale,τ, but Equation 6.40 uses a diffusive time scale, τ_d, for the nondimensionalization. In the text and Figures, Equations 6.38-6.40 are referred as HHC1, HHC2, and HHC3 respectively.

Equations 6.38-6.40 are expressed with the following initial and boundary conditions:

$$t^* = 0, \qquad \theta(\eta, 0) = 0, \qquad \frac{\partial \theta(\eta,0)}{\partial t^*} = 0 \tag{6.41}$$

$$\eta = 0, \qquad \theta(0, t^*) = 1 \tag{6.42}$$

$$\eta = 1, \qquad \frac{\partial \theta(1,t^*)}{\partial x} = -\gamma_1 J^* \theta \tag{6.43}$$

$$\eta = 1, \qquad \frac{\partial \theta(1,t^*)}{\partial x} = -\gamma_2 J^* \theta \tag{6.44}$$

where the Peltier coefficient $\gamma_1 = SJL/K$, is the boundary condition for Equation 6.38, which assumes a constant thermal conductivity, and $\gamma_2 = SJL/K(L)$ is the boundary condition for Equations 6.39 and 6.40. Here S is the Seebeck coefficient. It is assumed that the film at $\eta = 0$ is in contact with a perfect heat sink with same temperature as the environment. The lowest temperature is achieved when there is no external heat load onto the thermoelectric element at $\eta = 1$.

6.1.2.2 Ballistic-Diffusive Heat Conduction across Thermoelectric Thin Films

In the ballistic-diffusive heat conduction equations, the total temperature, θ, is decomposed into the diffusive and ballistic components. Thus the Joule heating must be applied for both of these components. To begin with, we rewrite Equation 6.36 as:

$$\frac{\partial q_b^*(\eta,t^*)}{\partial \eta} = \begin{cases} -\frac{1}{2\mathrm{Kn}}\left(2\theta_b^*(\eta,t^*) + \frac{\eta}{\mathrm{Kn}t^{*2}}e^{-t^*}\right) & (0 \le \mu_t \le 1) \\ 0 & other\ \mu_t \end{cases} \quad (6.45)$$

Moreover, we know that Equation 6.45 acts as a source term in Equation 6.31. Therefore, if we apply the Joule heating to Equation 6.37 as:

$$\theta_b^*(\eta,t^*) = \begin{cases} \frac{1}{2}\int_{\mu_t}^{1} e^{-\left(\frac{\eta}{\mu \mathrm{Kn}}\right)} d\mu + Z & (0 \le \mu_t \le 1) \\ 0 & other\ \mu_t \end{cases} \quad (6.46)$$

both the ballistic and diffusive components will be affected by the Joule heating, $Z = \beta_1 J^{*2}$. Since both the ballistic and diffusive temperatures in Equation 6.34 tend to zero, they are replaced with the following boundary condition in order to absorb the Peltier heat at the cold-junction surface:

$$\eta = 1, \qquad \frac{\partial \theta(1,t^*)}{\partial x} = -\gamma_1 J^* \theta \quad (6.47)$$

Here β_1 and γ_1 are used as the Joule and Peltier heating in the BDE, which assume a constant thermal conductivity**.** In total, Equations (6.31-6.33), (6.35), and (6.45-6.47) are all together solved to analyse the transient heat conduction and cooling in thermoelectric thin films.

6.1.3 Numerical solution

A second order fully implicit finite difference scheme is used to solve Equations (6.12), (6.17), (6.19), (6.31), and (6.38-6.40) in which discretization of all derivatives is central. In this way, a stable and convergent three-level finite difference scheme is applied which was introduced by Dai et al. [115]. It should be noted that a weighted average is used for stability and convergence in this method. Additionally, a mesh independency test is carried out to investigate convergence of the numerical cases which are not included in the paper. The above equations, respectively, are then discretized as:

$$\frac{\theta_i^{n+1}-2\theta_i^n+\theta_i^{n-1}}{\Delta t^2}+\frac{\theta_i^{n+1}-\theta_i^{n-1}}{2\Delta t}=\frac{\mathrm{Kn}^2}{3}(P_x)(\theta_i)$$

$$\frac{1}{4}\frac{\theta_i^{n+1}-2\theta_i^n+\theta_i^{n-1}}{\Delta t^2}+\frac{\theta_i^{n+1}-\theta_i^{n-1}}{2\Delta t}=\frac{1}{6\pi^2}\left(\sqrt{1+4\pi^2\mathrm{Kn}^2}-1\right)(P_x)(\theta_i)$$

$$\varphi\frac{\theta_i^{n+1}-2\theta_i^n+\theta_i^{n-1}}{\Delta t^2}+\frac{\theta_i^{n+1}-\theta_i^{n-1}}{2\Delta t}=\frac{\pi^2}{4}(P_x)(\theta_i)$$

$$\frac{\theta_i^{n+1}-2\theta_i^n+\theta_i^{n-1}}{\Delta t^2}+\frac{\theta_i^{n+1}-\theta_i^{n-1}}{2\Delta t}=\frac{\mathrm{Kn}^2}{3}(P_x)(\theta_i)-\mathrm{Kn}\frac{dq_b^*}{d\eta}$$

$$\frac{\theta_i^{n+1}-2\theta_i^n+\theta_i^{n-1}}{\Delta t^2}+\frac{\theta_i^{n+1}-\theta_i^{n-1}}{2\Delta t}=\frac{\mathrm{Kn}^2}{3}(P_x)(\theta_i)+\beta_1 J^{*2}$$

$$\frac{1}{4}\frac{\theta_i^{n+1}-2\theta_i^n+\theta_i^{n-1}}{\Delta t^2}+\frac{\theta_i^{n+1}-\theta_i^{n-1}}{2\Delta t}=\frac{1}{6\pi^2}\left(\sqrt{1+4\pi^2\mathrm{Kn}^2}-1\right)(P_x)(\theta_i)+\beta_2 J^{*2}$$

$$\varphi\frac{\theta_i^{n+1}-2\theta_i^n+\theta_i^{n-1}}{\Delta t^2}+\frac{\theta_i^{n+1}-\theta_i^{n-1}}{2\Delta t}=\frac{\pi^2}{4}(P_x)(\theta_i)+\beta_3 J^{*2}$$

$$P_x=\frac{\theta_{i+1}-2\theta_i+\theta_{i-1}}{\Delta x^2}$$

$$\theta_i=\frac{\theta_i^{n+1}+2\theta_i^n+\theta_i^{n-1}}{4} \tag{6.48}$$

The Gauss-Legendre integration scheme is used to calculate the ballistic components in both the transient ballistic-diffusive heat conduction equations and their application to the thermoelectric thin films. The diffusive boundary conditions in the BDE equations are discretized as:

$$\frac{\theta_i^{n+1}-\theta_i^{n-1}}{2\Delta t}+\theta_i^n=\pm\frac{2\mathrm{Kn}}{3}\left(\frac{\theta_{i+1}^{n+1}-\theta_{i-1}^{n+1}}{2\Delta x}\right) \tag{6.49}$$

MATLAB has been used for programing of these numerical schemes which can be found in the appendix of this thesis.

6.2 Results and Discussion

6.2.1 Transient Heat Conduction

The transient heat conduction in a thin film is investigated by solving the hyperbolic heat conduction equation (HHC) and the ballistic-diffusive heat conduction equations (BDE). The HHC is solved with three different formulations, namely, HHC with constant thermal conductivity and collision time scale (Equation 6.12), HHC with effective thermal conductivity and collision time scale (Equation 6.17), and HHC with effective thermal conductivity and diffusive time scale (Equation 6.19). In total, four different formulations are used to analyse the heat conduction process. Figures 6.1-6.4 show the temperature (or internal energy) and heat flux distributions obtained from

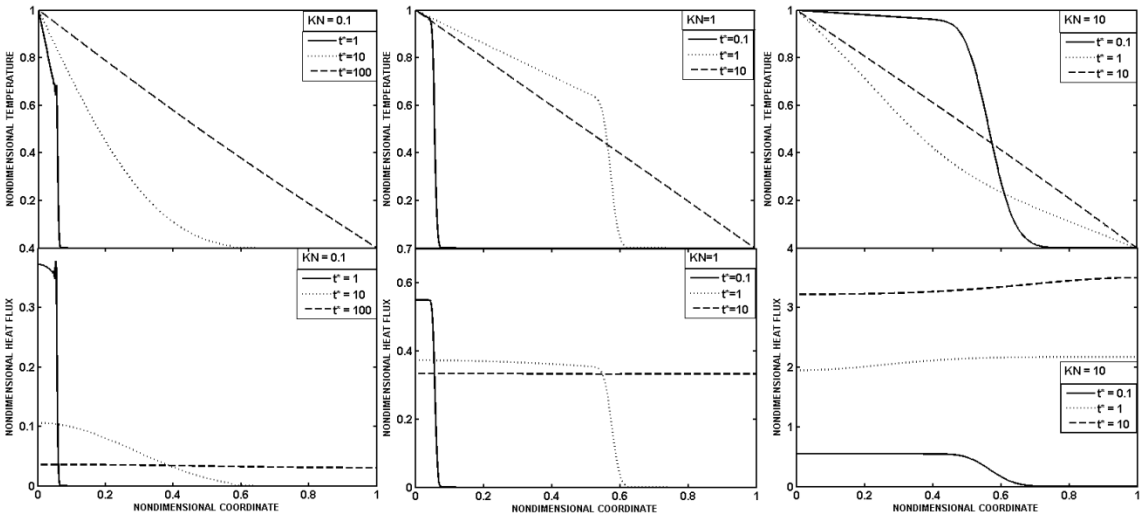

Figure 6-1: Non-dimensional temperature and heat flux distributions calculated from the hyperbolic heat equation with constant thermal conductivity for three different Knudsen numbers (Kn) and different non-dimensional times (t^*)

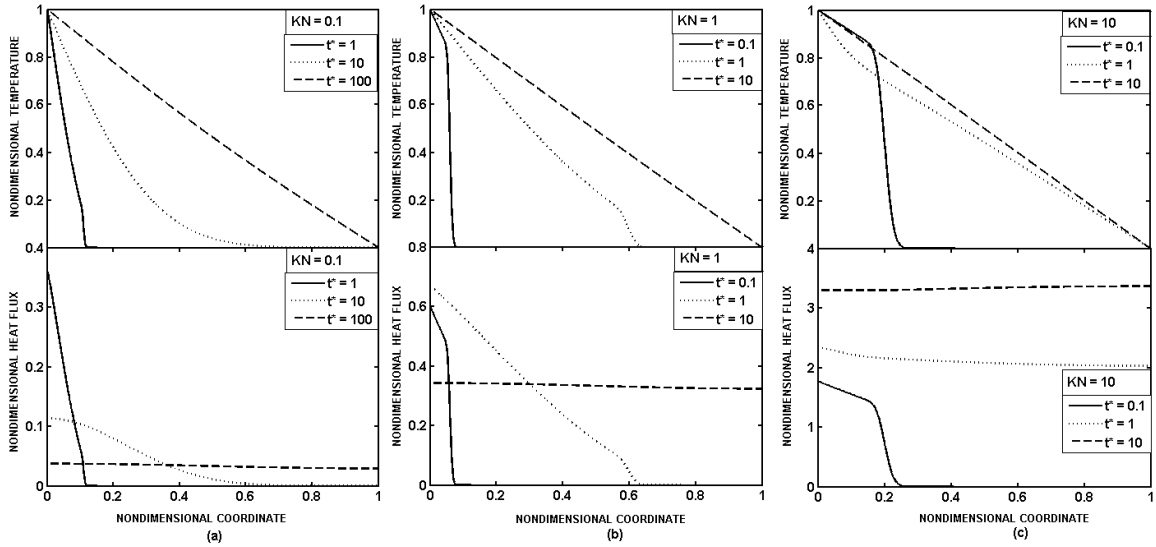

Figure 6-2: Non-dimensional temperature and heat flux distributions calculated from the hyperbolic heat equation with effective thermal conductivity and collision time scale for three different Knudsen numbers (Kn) and different non-dimensional times (t^*)

the HHC equations and the BDE, respectively, at various times for three different values of the Knudsen number. The temperature and heat flux calculated from the four approaches generally agree with each other at Knudsen number 0.1, particularly as the transport reaches steady state. A slight difference, nevertheless, exists between the HHC equations and the BDE even in the small Knudsen number limit.

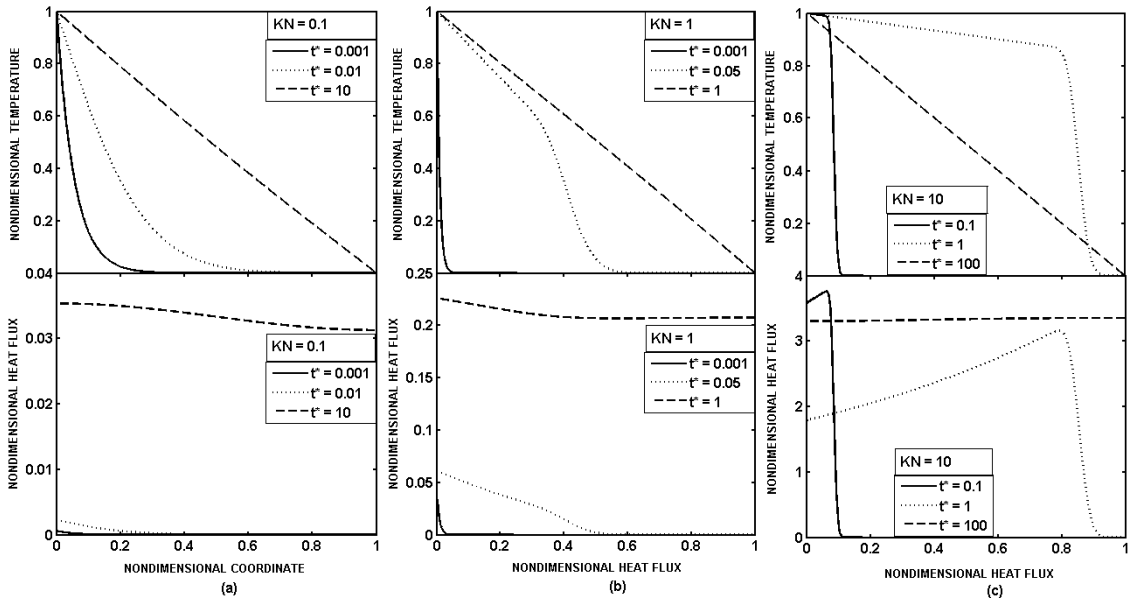

Figure 6-3: Non-dimensional temperature and heat flux distributions calculated from the hyperbolic heat equation with effective thermal conductivity and diffusive time scale for three different Knudsen numbers (Kn) and different non-dimensional times (t^*)

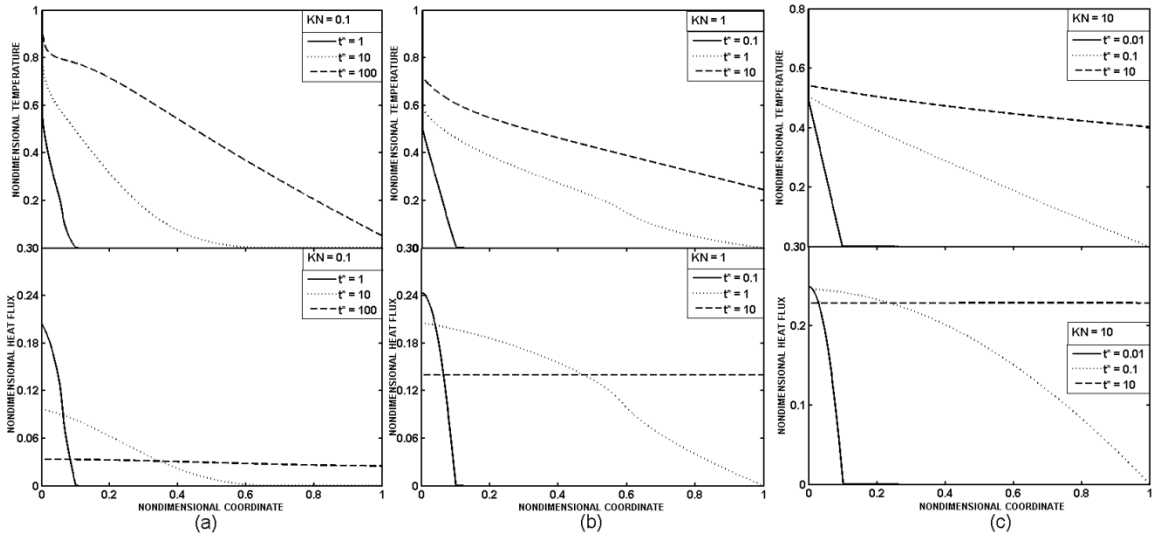

Figure 6-4: Non-dimensional temperature and heat flux distributions calculated from the ballistic-diffusive equations for three different Knudsen numbers (Kn) and different non-dimensional times (t^*)

The underlying physics is due to the subtle difference in the boundary conditions. When the Knudsen number equals unity, the HHC with constant heat conductivity and HHC with diffusive time scale lead to erroneous results, whereas HHC with size-

dependent conductivity reaches a general agreement with that of BDE. For Kn = 10, the BDE shows accurate time retardation due to finite speed of phonons, while the Cattaneo equations results in inaccurate conclusions. At the steady state and different Knudsen numbers, the temperature distribution predicted by the Cattaneo equations approaches that of the Fourier Law. The Cattaneo Equations over-predicts the heat flux by several times compared to the prediction by the BDE, which is in very good agreement with the phonon BTE [69].

Figure 6.5 illustrates the contributions of the ballistic and diffusive components to the total temperature (internal energy) and heat flux. As can be seen, the ballistic component of temperature has the least contribution to the total temperature for Kn = 0.1 and this increases with the Knudsen number. An opposite trend has been observed for the diffusive component. On the other hand, the ballistic component of the heat flux has the highest contribution to the total heat flux at all the Knudsen numbers while the diffusive component becomes negative at $\eta = 0$, and contributes less to the total heat flux. The negative heat flux is due to the fact that the back scattered heat carriers flow out of boundary.

6.2.2 Transient Thermoelectric Effect

The hyperbolic heat conduction equations (Equations 6.38-6.40) and ballistic-diffusive equations (Equations 6.31-6.33, 6.35, 6.45-6.47) are applied across a thermoelectric thin film in order to investigate the transient heat conduction process and the cooling mechanism at the cold junction surface. Doped Silicon is considered as the working material and its properties are taken from [67]. The comparative parameters from Equations 6.38-6.40 are listed in Table 6.1.

Kn	J	β_1	β_2	β_3	γ_1	γ_2	γ_3
0.1	10^{10}	0.0101	0.0110	8.139	0.0118	0.0129	0.0129
1	10^{11}	1.0082	0.9278	27.4743	0.0118	0.0435	0.0435
10	10^{12}	100.82	68.47	238.24	0.0118	0.377	0.377

Table 6-1: Calculated parameters from the hyperbolic heat equations when applied to thermoelectric thin films

Figure 6.6 shows the cooling and heat flux distribution obtained from the hyperbolic heat conduction equations (HHC1, HHC2, and HHC3) and the ballistic-

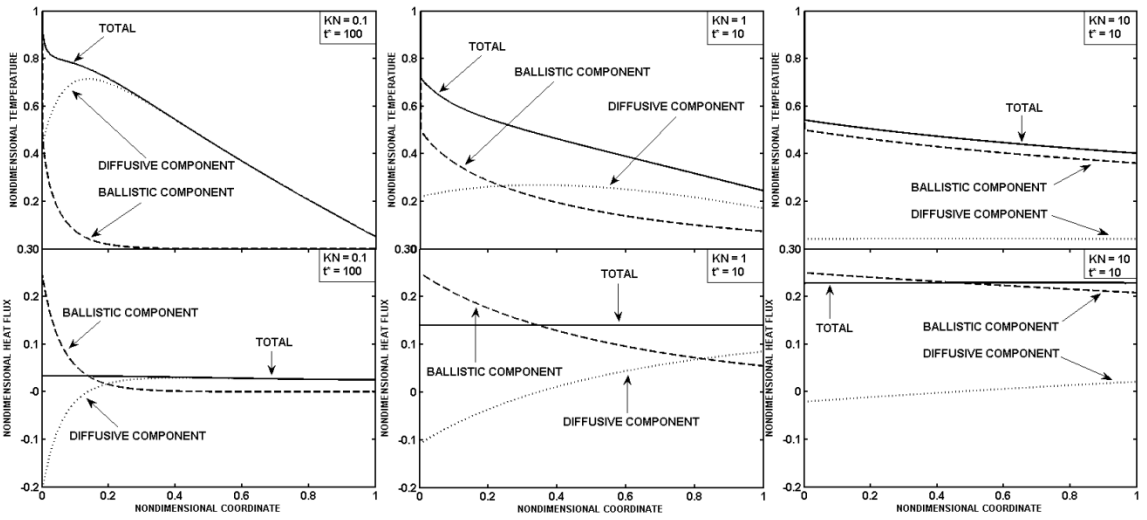

Figure 6-5: Contribution of the ballistic and diffusive components to the total temperature and heat flux

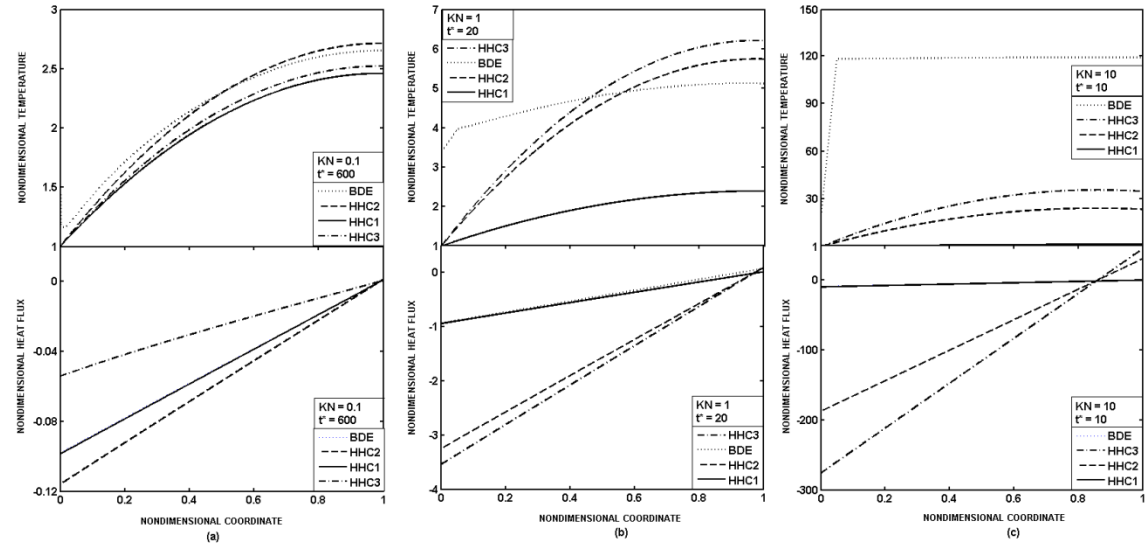

Figure 6-6: A comparison of the steady-state cooling and heat flux calculated from the BDE, HHC1, HHC2, and HHC3

diffusive heat conduction equations (BDE) across a thermoelectric thin film for three different values of the Knudsen number. At Kn = 0.1, all four approaches show approximately 2.5 degrees of cooling at the cold junction at the steady state and their equivalent transient cooling can be seen in Figure 6.7-a. This corresponds to the macro-scale length and similar results have been obtained from the transient parabolic equation for doped silicon analytically [63]. When the phonon mean free path becomes comparable with the device size (Kn = 1), solutions of the HHC2, HHC3,

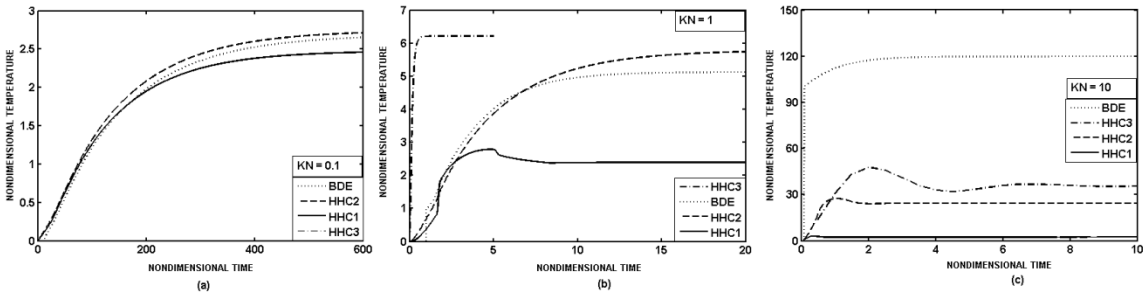

Figure 6-7: A comparison of the transient cooling at the cold side boundary calculated from the BDE, HHC1, HHC2, and HHC3

and the BDE show more than five degrees of cooling at the cold boundary. As can be seen from Table 6.1, the current density is increased one order of magnitude in order to achieve this amount of cooling when the Knudsen number goes from 0.1 to 1. By increasing the current in thermoelectrics, cooling increases linearly but at some point Joule heating dominates and prevents the further net cooling. This is also attributed to the considerable reduction of thermal conductivity in this scale. Similar experimental results have been observed in this scale in the literature [74]. The transient cooling further clarifies the difference among the four approaches (Figure 6.7-b). The result of HHC1 does not change with the Knudsen number and the current density. A close agreement can be seen between BDE and HHC2 as they show a similar result for the transient heat conduction in a thin film too. It can be concluded that those equations, which provide correct results for the transient heat conduction in a thin film, can produce similar results when applied across a thermoelectric thin film. In fact, the transient thermoelectric effect might be affected by the heat conduction. Moreover, it should be noted that in the BDE the boundary temperature is not constant, but increases with time (temperature jump). The temperatures used in the boundary conditions for the ballistic-diffusive equation are the temperatures of the emitted phonons, while those in the hyperbolic heat equations are those of the equilibrium phonons. The inconsistency between the temperatures used in the BDE and in the boundary condition creates this artificial temperature jump. At $\mathrm{Kn} = 10$, the HHC1, again, does not capture the size effect and leads to unrealistic results. There is a remarkable difference among the other three approaches: maximum cooling of approximately 25, 35, and 120 are calculated at the cold side boundary by the HHC2, HHC3, and BDE respectively. At the moment, there is no experimental results to validate these findings at $\mathrm{Kn} = 10$. However, the previous results show that those

equations produce erroneous results for the transient heat conduction in a thin film and can lead to inaccurate results in predicting the cooling in a thermoelectric thin film. Therefore, we can suggest that the results obtained from the calculation of the hyperbolic equations are inaccurate and the results from the BDE remain uncertain as the temperature jump is huge in this case.

Figure 6.8 further analyses the data achieved from the solution of the BDE across a thermoelectric thin film. This can be better appreciated if we compare Figures 6.8 and 6.5, which show the solution of the BDE in a thin film. It is clear that at$\mathrm{Kn} = 0.1$, the diffusive heat carriers are dominant and the BDE shows a similar behaviour as the hyperbolic heat conduction equations. At unity, both the diffusive and ballistic components are affected by the Joule and Peltier heating. However, at $\mathrm{Kn} = 10$, mainly the ballistic component is affected and leads in a linear increase of the temperature in the whole body.

6.3 Conclusion

At first stage, we investigated the transient heat conduction problem in a thin film. The hyperbolic heat conduction equation with three different formulations –HHC1 with constant thermal conductivity, HHC2 with effective thermal conductivity and collision time unit, and HHC3 with effective thermal conductivity and diffusive time scale- are solved. Moreover, the ballistic-diffusive heat conduction equations are solved with a convergent and stable finite difference scheme. Computational results from these four approaches suggest that the HHC1 with constant thermal conductivity and HHC3 with effective thermal conductivity but diffusive time scale lead to unrealistic results at scales when the mean free path is comparable to the system size and when the time is comparable to the carrier relaxation time. HHC2 with effective thermal conductivity but collision time unit reaches to a general agreement with that of the BDE at the Knudsen numbers equal to unity and less and results in inaccurate results at the higher Knudsen number.

Next, these four different equations are applied to a thermoelectric thin film. It was found out that the HHC1 does not capture the size effect and predicts the same amount of cooling for all values of Knudsen number in a thermoelectric thin film. The solutions of the HHC2 and BDE are in a close agreement at Kn = 0.1 and 1 but slightly different with that of HHC3. At Kn = 10, maximum cooling of approximately

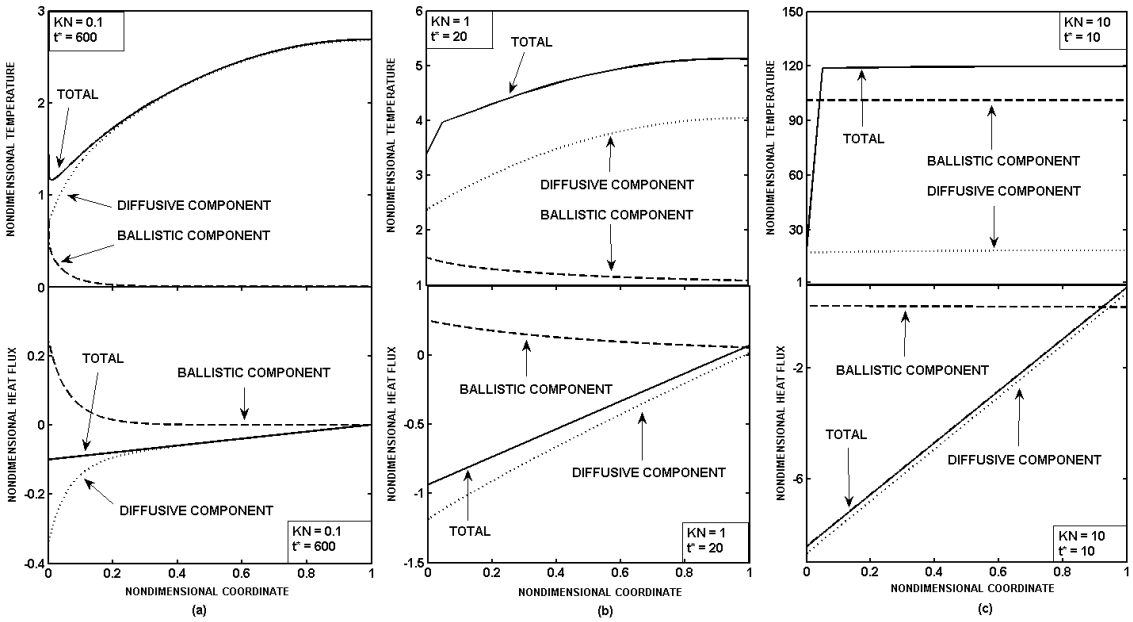

Figure 6-8: Contribution of the ballistic and diffusive components to the total temperature and heat flux calculated from the BDE across a thermoelectric thin film

25, 35, 120 are predicted by the HHC2, HHC3, and BDE, respectively. It is also discovered that the diffusive component in the BDE are mainly affected by the Joule and Peltier heating at Kn = 0.1 and 1 but the ballistic component has the highest contribution in the cooling at Kn = 10.

It can be concluded that the inaccurate predictions of the equations for the transient heat conduction in a thin film, led to less accurate predictions of cooling at the cold side boundary, temperature, and heat flux profile in the thermoelectric film.

7 Conclusions

In this thesis, Supersonic flow phenomena, combustion, discrete droplets motion with heating, disintegration and vaporization, thin film and thermoelectric thin film heating and cooling are studied. Parametric studies have been carried out for the High Velocity Suspension Flame Spray (HVSFS) process to provide an understanding of the underlying physics and investigate the liquid feedstock behaviour under different conditions. These studies thoroughly describe the gas phase characteristics; look in detail at the disintegration, evaporation and combustion of discrete phase ethanol droplets and the interactions between the gas and liquid phases; providing a step forward in the understanding of liquid feedstock devices and nanostructured coatings. In parallel with these works, heat transfer in thin films and thermoelectric thin films is studied for the application of thermally sprayed nanostructured coatings. The results obtained shed light on the physical phenomena involved in the process and suggest a set of optimum spray conditions serving as a fundamental reference to further develop the technology.

7.1 Novel Contributions to the Science of Thermal Spraying

This project has investigated through numerical simulation of the High Velocity Suspension Flame Spraying (HVSFS) process in order to give a detailed understanding of the current supersonic thermal spraying for suspension based coatings, as well as heat propagation in thin films and thermoelectric thin films which are fabricated by thermally sprayed coatings. As it is outlined in Chapter 1, all contributions are published within peer reviewed journals. A list of the chapter by chapter novel contributions made during this project is as following:

- *chapter three* investigates liquid feedstock behaviour in the HVSFS process through numerical modelling of supersonic gas phenomena and the disintegration of discrete phase ethanol droplets with rates of evaporation. The results obtained indicate that the initial mass flow rate of the liquid feedstock mainly controls the HVSFS process. If the optimum amount of liquid mass is

injected to a gun, the area of maximum evaporation will occur inside the combustion chamber, leading to less cooling of the gas temperature and less reduction of gas velocity. However, if more amount of liquid mass injection is demanded, the design of a conventional HVOF gun should be modified such that its combustion chamber accommodates the area of maximum evaporation of suspension. It is found out that the barrel and external injection schemes are not likely suitable for HVSFS process as high injection force is required to penetrate liquid droplets into the core area of the gas dynamics. However, as droplets injected from the combustion chamber vertically, relatively good output is observed as such the gas dynamics is less disrupted and area of maximum evaporation occurs inside the combustion chamber. Combustion analysis illustrated that being achieved maximum gas temperature and velocity in the HVSFS process, oxygen and propane mass fraction should be fixed before introducing liquid feed stock into the gun. Nevertheless, liquid ethanol droplets may not fully combust inside the nozzle due to the lack of oxygen. The results obtained in this chapter give a new insight to the mechanisms which control the HVSFS thermal spraying and serve as a fundamental reference for future development of liquid feedstock devices using ethanol based suspensions.

- *chapter four* examines the liquid feedstock or suspension as a different mixture of liquid fuel ethanol and water which is numerically studied in the HVSFS process and the results are compared for homogenous liquid feedstock of ethanol and water. The results show that organic solvent or mixture with high percentage of combustible species experiences rapid evaporation due to the lower boiling point, while solvent containing aqueous solution or mixture with high aqueous percentage undergoes slower evaporation. Since large relative velocities between liquid droplets and gas phase are developed in the combustion chamber, the aerodynamic break up of particles is more pronounced. Pure solvent or multicomponent solvent droplets leave the combustion chamber with an average size of (5 μm) due to lower surface tension. Full evaporation is achieved before the gun exit. In contrast, those droplets with high surface tension pass through the convergent-divergent section with a diameter larger than 10 μm. When the relative liquid/gas

velocity becomes smaller the droplets evaporate and release the nanoparticles far from the gun exit. In cases of multicomponent droplets of high percentage of organic solvent less cooling is observed. The spontaneous temperature drop upon injection is effectively recovered after secondary (solvent/oxygen) combustion. Large disruption of the gas velocity is prevented mainly due to the limiting cooling effect which allows for high pressure build-up in the combustion chamber. The results of this work can be used as a reference for avoiding extraneous trial and error experimentations. It can assist in adjusting the spraying parameters for different powder materials and it can provide a means of visualization of the phenomena taking place during liquid spray. The particle in-flight heating can be effectively controlled by altering the solvent composition, while the temperature and velocity of the exhaust gases can be pitched at the appropriate level in the same way.

- *chapter five* also investigates the effects of solid nanoparticles, suspended in liquid feedstock, on suspension fragmentation, vaporization rate and gas dynamics in the High Velocity Oxygen Fuel (HVOF) suspension spraying process by numerical modelling. The results reveal that there is a considerable difference in the final location of evaporation of homogeneous and non-homogeneous droplets. This is an important factor in the numerical analysis of suspension as nanoparticles are created in a computational domain as new entities. It is suggested that if a high concentration loading in a suspension is favoured in an application, the use of smaller droplets (up to 50 μm) give a better result as they experience high evaporation in the mid-section of the nozzle. However, if larger droplets (150 and 300 μm) are injected into the gun, fragmentation is the dominant factor which controls the process. With increasing solid particle concentrations in the droplets the final location of evaporation moves towards the gun exit and in the extreme cases the droplets leave the gun without complete evaporation. Finally, it is observed that large droplets undergo severe fragmentation inside the combustion chamber which causes evaporation to take place in front of the convergent-divergent nozzle even with the highest nanoparticle loading.
- *chapter six* studies heat transfer in thin films and nanostructured thermoelectrics. Computational results from the four approaches suggest that

the HHC1 with constant thermal conductivity and HHC3 with effective thermal conductivity but diffusive time scale lead to unrealistic results at scales when the mean free path is comparable to the system size and when the time is comparable to the carrier relaxation time. HHC2 with effective thermal conductivity but collision time unit reaches to a general agreement with that of the BDE at the Knudsen numbers equal to unity and less and results in inaccurate results at the higher Knudsen number. Moreover, it is found out that the HHC1 does not capture the size effect and predicts the same amount of cooling for all values of Knudsen number in a thermoelectric thin film. The solutions of the HHC2 and BDE are in a close agreement at Kn = 0.1 and 1 but slightly different with that of HHC3. At Kn = 10, maximum cooling of approximately 25, 35, 120 are predicted by the HHC2, HHC3, and BDE, respectively. It is also discovered that the diffusive component in the BDE are mainly affected by the Joule and Peltier heating at Kn = 0.1 and 1 but the ballistic component has the highest contribution in the cooling at Kn = 10. It can be concluded that the inaccurate predictions of the equations for the transient heat conduction in a thin film, led to less accurate predictions of cooling at the cold side boundary, temperature, and heat flux profile in the thermoelectric film. Moreover, the BDE model can be used to analyse heat propagation in nanoparticles travelling inside thermal spray torches as well as heat transfer in nanostructured coatings fabricated by thermal spray processes.

7.2 Future Work

As discussed in the Chapter 1 of this thesis, over recent years a great deal of interest has developed for the thermal spraying of submicron and Nano-scale sized powders in order to pursue more advanced thermal spray coatings. Coatings manufactured using thermal spray methods can give a deposition rate an order of magnitude higher than its closes competitors: Physical Vapour Deposition (PVD) and Chemical Vapour Deposition (CVD). Moreover, with PVD and CVD thick coatings beyond 10 μm cannot be produced. Coatings are difficult to be reproduced consistently by the current thermal spray techniques on a large scale, a variety of thermal spray techniques have been used in pursuit of depositing nanoparticles from a suspension, including flame, plasma, and HVOF. For depositing submicron-scale and Nano-scale

powders, the current thermal spray approaches are required to be developed further. The suspension method is a necessary component of this design for health and safety reasons during transport and storage and in order to provide powders the enough momentum to enter the centre of the thermal spray jet. There exists a knowledge gap which is hindering thermal spray technology from entering the commercial market and making the next step forward.

Compared with the traditional spraying of micro-scale particles, the suspension processing is far more complex due to the disintegration and evaporation of the liquid component of the suspension. Detailed understanding of these phenomena within the complex thermal spray jet for close control is required in order to create a consistent coating with the required coating architecture. It is highly necessary to simulate and compare the wide range of thermal spray conditions in order to design and develop the next generation of thermal spray technologies. Numerical simulations can provide a full spectrum of thermal spray velocities and temperatures and the interrelation between processing gas and the liquid droplets. This thesis includes the simulation of the HVSFS process along with the discrete phase liquid droplets.

The trajectory of the suspension as well as their breakup and vaporization characteristics within the HVSFS process have been studied under different conditions in Chapter 3-5 of this thesis. However, with some assumptions nanoparticles are not charged into the liquid feedstock, and this is a key requirement for the next stages of study as nanoparticles might precipitate and agglomerate within liquid droplets. Therefore, the next step should be injection of a suspension, which contains both nanoparticles and liquid solvent, into the flame jet where heat propagation inside nanoparticles and heat transfer from gas and liquid to powders should be based on a Nano-scale formula not macro-scale. Fundamental studies are required to analyse heat transfer in single and agglomerated nanoparticles as heat phenomena differs in Nano-scale from that of macro-scale, which is discussed in the Chapter 6. The BDE model is required to be applied for the nanoparticles discharged during thermal spray processes and on thermally sprayed nanostructured coatings especially for thermally sprayed thermoelectric coatings.

Appendix A

8 Computational Methodology

8.1 Flow Description

This appendix provides further descriptions of the models applied in this project. The basic equations of fluid dynamics are derived based on the assumption of continuum, where:

$$\begin{bmatrix} rate\ of\ change\ of \\ total\ property\ in\ Vol \end{bmatrix} = \begin{bmatrix} rate\ of\ property \\ being\ created\ in\ Vol \end{bmatrix} + \begin{bmatrix} property\ flowing \\ into\ Vol \end{bmatrix} + \begin{bmatrix} property\ flowing \\ out\ of\ Vol \end{bmatrix}$$

which expresses the conservation of flow quantity inside an arbitrary volume (Control Volume Method). These conservation laws (mass, momentum, and energy) describes the dynamics behaviour of fluid flow and make the complete system by the integral expressions as follows:

$$\frac{\partial}{\partial t}\int_{\Omega} \vec{W} d\Omega + \int_{S} \left(\vec{F}_c - \vec{F}_v\right) dS = \int_{S} \vec{Q} dS \tag{A.1}$$

where Ω stands for the control volume and S represents the surface that encloses Ω. The term $\vec{W}$ holds five components: namely, mass, momentum in all three directions and energy. The terms $\vec{F}_v$ and $\vec{F}_c$ represent the viscous flux and the convective flux vectors respectively. The contribution of all external volume sink and source terms is represented by the vector $\vec{Q}$.

The expanded expression of the column vectors are:

$$\vec{W} = \begin{bmatrix} \rho \\ \rho u \\ \rho v \\ \rho w \\ \rho E \end{bmatrix};\ \vec{F}_c = \begin{bmatrix} \rho V \\ \rho u V + n_x p \\ \rho v V + n_y p \\ \rho w V + nzp \\ \rho H V \end{bmatrix};\ \vec{F}_v = \begin{bmatrix} 0 \\ n_x\tau_{xx} + n_y\tau_{xy} + n_z\tau_{xz} \\ n_x\tau_{yx} + n_y\tau_{yy} + n_z\tau_{yz} \\ n_x\tau_{zx} + n_y\tau_{zy} + n_z\tau_{zz} \\ n_x\Theta_x + n_y\Theta_y + n_z\Theta_z \end{bmatrix};\quad Q = \begin{bmatrix} 0 \\ \rho f_{ex} \\ \rho f_{ey} \\ \rho f_{ez} \\ \rho \vec{f}_e.\vec{v} + \dot{q}_h \end{bmatrix} \tag{A.2}$$

The viscous stresses in a Newtonian fluid are related to the rate of deformation. For compressible flows the three dimensional form of Newton's law of viscosity has two constants: the second viscosity λ (related to volumetric deformations) and the dynamic viscosity μ (related to linear deformations). The symmetric viscous stress, τ, is defined as:

$$\tau_{ij} = \mu\left(\frac{\partial u_i}{\partial x_j} + \frac{\partial u_j}{\partial x_i}\right) + \delta_{ij}\lambda\vec{\nabla}.\vec{v} \tag{A.3}$$

In practice, the bulk viscosity has less effect and is approximated as:

$$\lambda = -\frac{2}{3}\mu \tag{A.4}$$

All the typology acting directly on the mass such as gravitational, Coriolis, and buoyancy forces are considered as the external or body forces, $\bar{f}_e$. The total enthalpy H is given by the relation:

$$H = e + \frac{|\upsilon|^2}{2} + \frac{p}{\rho} \tag{A.5}$$

where e is the internal energy per unit mass and for a perfect gas is given as:

$$e = \frac{p}{\rho(\gamma - 1)} \tag{A.6}$$

where γ is the heat specific heat ratio $\frac{C_p}{C_v}$.

8.2 Turbulence Modelling

Fluid flow becomes random and chaotic above a critical Reynolds number which is termed turbulence. Within science today, the modelling of turbulence is one of the most challenging and unexplainable concepts. The characteristics of turbulence can be summarized as:

- Three dimensional random fluctuations occur in flow-field variables. Consequently, compared with sole molecular diffusion the turbulence strongly increases the mixing behaviour of the flow. The mixing activity is directly

linked to the presence of gradients in the time-averaged flow in terms of mathematical point of view.

- The Kolmogorov length scale is known as the presence of eddies of various sizes from a characteristic dimension down to the smallest eddy.
- The small-scale eddies motion is dissipated and converted into thermal energy and work against the action of viscous stresses.

Turbulence is mostly encountered flow regime in engineering applications. Direct Numerical Simulation (DNS) is the only way to solve numerically the Navier-Stokes equations in order to obtain a complete description of the flow field in time and space. However, for engineering applications, the DNS method is not practical owing to the great range of time scales which require to be resolved. That is the reason; an approximation solution is used to solve the instantaneous turbulent flow.

There are three groups of turbulence models; namely, large eddy simulation (LES), first order closure, and second order closure. The LES model solves the large vortex structures and models the effect of small structure which has a more homogeneous character. On the other hand, the first order closure models are typically based on the linear eddy viscosity hypothesis introduced by Boussinesq and RSM models use the exact equations for the Reynolds-Stresses $\overline{v_i'v_j'}$ in which the closure is necessary for higher order correlation terms $\overline{v_i'v_j'v_k'}$. These two methods are known as RANS (Reynolds Averaged Navier Stokes).

8.2.1 The RANS Equations

The differential form of the Navier Stokes equation with assumption that there are no sources or sinks are given by:

$$\frac{\partial \rho}{\partial t} + \frac{\partial}{\partial x_i}(\rho v_i) = 0$$

$$\frac{\partial}{\partial t}(\rho v_i) + \frac{\partial}{\partial x_i}\left(\rho v_j v_i\right) = -\frac{\partial p}{\partial x_i} + \frac{\partial \tau_{ij}}{\partial x_j} \qquad \text{(A.7)}$$

$$\frac{\partial}{\partial t}(\rho E) + \frac{\partial}{\partial x_j}\left(\rho v_j H\right) = \frac{\partial}{\partial x_j}\left(v_i \tau_{ij}\right) + \frac{\partial}{\partial x_j}\left(k \frac{\partial T}{\partial x_j}\right)$$

The compact notation for the viscous stress tensor is given by:

$$\tau_{ij} = \mu\left(\frac{\partial v_i}{\partial x_j} + \frac{\partial v_j}{\partial x_i}\right) - \left(\frac{2\mu}{3}\right)(\vec{\nabla}.\vec{v})\delta_{ij} \tag{A.8}$$

The underlying concept in the statistical analysis of the RANS equations is to decompose the flow variable u into a fluctuating component u' and its mean value $\bar{u}$:

$$u = \bar{u} + u' \tag{A.9}$$

There are four possible averaging methods that can be used to obtain the mean value as follows:

1. Time averaging (u varies only in space)
2. Spatial averaging (u varies only in time)
3. Ensemble averaging (u varies with both time and space)
4. Density weighted averaging (Favre decomposition)

The first three approaches are called Reynolds averaging and they are equivalent when the turbulent flow is homogeneous and stationary. Favre method is suitable for compressible flow. The analytical expressions for the four approaches are:

$$\begin{aligned}
&a) \quad \bar{u}_i = \lim_{\Delta t\to\infty} \frac{1}{\Delta t}\int_t^{t+\Delta t} u_i dt \,; \\
&b) \quad \bar{u}_i = \lim_{\Omega\to\infty} \frac{1}{\Omega}\int_\Omega u_i d\Omega \,; \\
&c) \quad \bar{u}_i = \lim_{N\to\infty} \frac{1}{N}\sum_{n=1}^{N} u_i \,; \\
&d) \quad \overline{\bar{u}}_i = \frac{1}{\bar{\rho}} \lim_{\Delta t\to\infty} \frac{1}{\Delta t}\int_t^{t+\Delta t} \rho u_i dt \,;
\end{aligned} \tag{A.10}$$

The mean of fluctuating term, $\overline{u_i'}$, is zero and the mean of the product of the two fluctuating terms, $\overline{u_i'u_j'}$, is not zero. $\overline{\overline{\rho u_i}} = \bar{\rho}\overline{\bar{u}}_i$ and $\overline{\overline{\rho u_i''}} = 0$ for the Favre decomposition method. The application of the Favre averaging to the Navier-stokes equations (A.7) gives the so called RANS equations:

$$\begin{aligned}
&\frac{\partial \bar{\rho}}{\partial t} + \frac{\partial}{\partial x_i}\left(\bar{\rho}\overline{\bar{v}}_i\right) = 0 \\
&\frac{\partial}{\partial t}\left(\bar{\rho}\overline{\bar{v}}_i\right) + \frac{\partial}{\partial x_i}\left(\bar{\rho}\overline{\bar{v}}_j\overline{\bar{v}}_i\right) = -\frac{\partial \bar{p}}{\partial x_i} + \frac{\partial}{\partial x_j}\left(\overline{\bar{\tau}}_{ij} - \bar{\rho}\overline{v_i''v_j''}\right)
\end{aligned} \tag{A.11}$$

$$\frac{\partial}{\partial t}\left(\bar{\rho}\tilde{E}\right)+\frac{\partial}{\partial x_j}\left(\bar{\rho}\tilde{v}_j\tilde{H}\right)=\frac{\partial}{\partial x_j}\left[\tilde{v}_i\left(\tilde{\tau}_{ij}-\bar{\rho}\widetilde{v_i''v_j''}\right)\right]+\frac{\partial}{\partial x_j}\left(k\frac{\partial\bar{T}}{\partial x_j}-\bar{\rho}\widetilde{v_j''h''}+\widetilde{\tau_{ij}v_i''}-\bar{\rho}\widetilde{v_j''K}\right)$$

The Reynolds stress tensor in the above equation is given by:

$$\tau_{ij}^R=-\bar{\rho}\widetilde{v_i''v_j''} \tag{A.12}$$

The sum of the normal stresses forms the turbulent kinetic energy:

$$\bar{\rho}\tilde{K}=\frac{1}{2}\bar{\rho}\widetilde{v_i''v_i''} \tag{A.13}$$

The term expressing the turbulent transport of K, $\frac{\partial}{\partial x_j}\left(\bar{\rho}\widetilde{v_j''K}\right)$ and molecular diffusion, $\frac{\partial}{\partial x_j}\left(\widetilde{\tau_{ij}v_i''}\right)$, are usually neglected in transonic and supersonic flow. After the averaging procedure, six more unknown terms in the equations describing the flow are introduced as the Reynolds stress tensor is symmetric. Additionally, three other unknowns come from the components of the turbulent heat flux vector $\frac{\partial}{\partial x_j}\left(\bar{\rho}\widetilde{v_j''h''}\right)$.

By averaging the product of second equation in (A.7) and fluctuating quantity, the exact Reynolds stress transport description can be derived:

$$\frac{\partial\tau_{ij}^R}{\partial t}+\frac{\partial}{\partial x_k}\left(\tilde{v}_k\tau_{ij}^R\right)=-\tau_{ik}^R\frac{\partial\tilde{v}_j}{\partial x_k}-\tau_{jk}^R\frac{\partial\tilde{v}_i}{\partial x_k}+\varepsilon_{ij}-\Pi_{ij}+\frac{\partial}{\partial x_k}\left[-\overline{\tau_{kj}v_i''+\tau_{ki}v_j''}+C_{ijk}\right]$$
$$+\bar{v}_i''\frac{\partial\bar{p}}{\partial x_j}+\bar{v}_j''\frac{\partial\bar{p}}{\partial x_i} \tag{A.14}$$

where

$$\Pi_{ij}=\overline{p'\left(\frac{\partial v_i''}{\partial x_j}+\frac{\partial v_j''}{\partial x_i}\right)};\qquad \varepsilon_{ij}=\overline{\tau_{kj}\frac{\partial v_i''}{\partial x_k}+\tau_{ki}\frac{\partial v_j''}{\partial x_k}}$$
$$C_{ijk}=\bar{\rho}\widetilde{v_i''v_j''v_k''}+\overline{p'v_i''}\delta_{jk}+\overline{p'v_j''}\delta_{ik} \tag{A.15}$$

Extra unknowns (e.g. $\widetilde{v_i''v_j''v_k''}$) are created every time a higher moment (averaging level) is taken due to the nonlinearity of the momentum conservation equation. An empirical model is used for the closure of equation (A.14).

8.2.2 The $k-\epsilon$ Turbulence Model

This is a two-equation turbulence model which relies on the solution of two additional transport equations, one for the turbulent dissipation rate ε and the other for its kinetic energy K:

$$\frac{\partial \bar{\rho}\overline{\overline{K}}}{\partial t}+\frac{\partial}{\partial x_j}\left(\overline{\overline{K}}\bar{\rho}\overline{\overline{v_j''}}\right)=\frac{\partial}{\partial x_j}\left[\left(\mu+\frac{\mu_T}{\mathrm{Pr}_K}\right)\frac{\partial \overline{\overline{K}}}{\partial x_j}\right]-\bar{\rho}\varepsilon-P_K-P_b-2\bar{\rho}\varepsilon M_T^2$$

$$P_K=\bar{\rho}\overline{\overline{v_i''v_j''}}\frac{\partial \overline{\overline{v_i}}}{\partial x_j};\qquad P_b=g_i\frac{\mu_T}{\bar{\rho}\,\mathrm{Pr}_T}\frac{\partial \bar{\rho}}{\partial x_i};\quad M_T=\sqrt{\frac{\overline{\overline{K}}}{a^2}} \tag{A.16}$$

where P_b and P_K represent the generation of turbulent kinetic energy due to main buoyancy and velocity gradients, respectively. The equation for approximating the dissipation of turbulent kinetic energy is given by:

$$\frac{\partial \bar{\rho}\varepsilon}{\partial t}+\frac{\partial \bar{\rho}\varepsilon\overline{\overline{v_j}}}{\partial x_j}=\frac{\partial}{\partial x_j}\left[\left(\mu+\frac{\mu_T}{\mathrm{Pr}_\varepsilon}\right)\frac{\partial \varepsilon}{\partial x_j}\right]-\left(C_{\varepsilon 1}P_K+C_{\varepsilon 2}\bar{\rho}\varepsilon+C_{\varepsilon 3}P_b\right)\frac{\varepsilon}{\overline{\overline{K}}} \tag{A.17}$$

where the eddy viscosity is given by:

$$\mu_T=C_\mu\bar{\rho}\frac{\overline{\overline{K^2}}}{\varepsilon} \tag{A.18}$$

The closure coefficients are:

$$C_{\varepsilon 1}=1.44;\qquad C_{\varepsilon 2}=1.92;\qquad C_\mu=0.09;\qquad P_K=1.0;\qquad P_\varepsilon=1.3; \tag{A.19}$$

8.3 Programming Heat Conduction Equations

In this thesis, the parabolic, hyperbolic, and ballistic-diffusive heat conduction equations are numerically solved and their application for thin films and thermoelectric thin films are investigated. A complete description of the investigation can be found in the Chapter 6 of this thesis. In this section, only two sample programs are selected in order to illustrate the overall programming method.

The first programing code which is implemented in Matlab attempts to solve the hyperbolic heat conduction equation in a thermoelectric thin film:

```
XL=1;                    % non-dimensional length
TL=600;                  % nondimensional time
```

```
KN=0.1;                  % Knudsen number
LANDA=40*10^-9;          % mean free path
L=LANDA/KN;              % dimensional length

DELTAX=.001;
DELTAT=.001;

IMAX=XL/DELTAX+1;
KMAX=TL/DELTAT+1;

R2=(DELTAT/DELTAX)^2;
R1=(DELTAT/DELTAX);


A=(KN^2)/3;

ERRMAX=10e-8;
ERR=1;

%-------------------thermoelectric properties------------
K0=149;
a=88*10^-6;
C0=K0/a;
SIG=35.5*10^3;
TO=6.06*10^-12;
J0=10^10;
J=1;
BETA=(J0^2*TO)/(C0*SIG*1);
Z=BETA*J^2;
S=440*10^-6;
GAMA=(S*J0*J*L)/K0;


%-------------------INITIAL CONDITION--------------------
TMN(1:IMAX)=0;
TMO(1:IMAX)=0;
TTM(1:IMAX)=0;
TTTM(1:IMAX)=0;
QMN(IMAX)=0;
QMO(IMAX)=0;
T(IMAX)=0;
X(IMAX)=0;
Q(IMAX)=0;
P(IMAX)=0;
U(IMAX,KMAX)=0;
V(IMAX,KMAX)=0;

%-----------------------SOLVING -------------------------
for K=1:KMAX
    T(K)=DELTAT*(K);
 for I=1:IMAX
```

```
  X(I)=DELTAX*(I-1);
 end
TMO(1:IMAX)=0;
TMN(1:IMAX)=0;
                              % TEMPERATURE
  while ERR>ERRMAX
  TMN(1)=1;

  for I=2:IMAX-1
   TMN(I)=(TTM(I)*(2)+TMO(I+1)*(A*R2)+TMO(I-1)*(A*R2)+...
   TTTM(I)*(.5*DELTAT-1)+Z*DELTAT^2)/(1+DELTAT/2+2*A*R2);
  end

  TMN(IMAX)=(TTM(IMAX)*(2-2*A*R2*DELTAX*GAMA)+TMO(IMAX-
1)*(2*A*R2)+...
   TTTM(IMAX)*(.5*DELTAT-
1)+Z*DELTAT^2)/(1+DELTAT/2+2*A*R2);


 ERR=max(abs(TMN-TMO));
 TMO=TMN;
  end
                              % HEAT FLUX
 QMO=QMN;
 QMN(1)=(QMO(1)-KN*R1*(TMN(2)-TMN(1))/3)/(DELTAT+1);

 for  I=2:IMAX-1
   QMN(I)=(QMO(I)-KN*R1*(TMN(I+1)-TMN(I-1))/6)/(DELTAT+1);
 end

 QMN(IMAX)=(QMO(IMAX)-KN*R1*(TMN(IMAX)-TMN(IMAX-
1))/3)/(DELTAT+1);

TTTM=TTM;
TTM=TMN;
ERR=1;

U(1:IMAX,K)=TMN;
V(1:IMAX,K)=QMN;

end
```

The second code solves the application of ballistic-diffusive heat conduction equation for a thermoelectric thin film:

```
XL=1;                  % non-dimensional length
TN=600;                % non-dimensional time
KN=0.1;                % Knudsen number
LANDA=40*10^-9;        % mean free path
```

```
L=LANDA/KN;          % dimensional length

DELTAX=.001;
DELTAT=.001;

IMAX=XL/DELTAX+1;
KMAX=TN/DELTAT+1;

R1=DELTAT/DELTAX;
R2=(DELTAT/DELTAX)^2;
A=(KN^2)/3;
B=(2*KN)/3;
ERRMAX=10e-8;
ERR=1;

%---------------THERMOELECTRIC PROPERTIES----------------
J0=10^10;
TO=6.06*10^-12;
K0=149;
a=88*10^-6;
C0=K0/a;
SIG=35.5*10^3;
BETA=(J0^2*TO)/(C0*SIG*1);
J=1;
Z=BETA*J^2;
S=440*10^-6;
GAMA=(S*J0*J*L)/(K0);


%--------GAUUS INTEGRATION'S ROOTS AND COOFICIENTS-------
C(1)=.3478548451;
C(2)=.6521451549;
C(3)=C(2);
C(4)=C(1);

R(1)=.8611363116;
R(2)=.3399810436;
R(3)=-R(2);
R(4)=-R(1);

%-------------------INITIAL CONDITION--------------------
TB(IMAX)=0;
QB(IMAX)=0;
DQB(IMAX)=0;
TMN(IMAX)=0;
TMO(IMAX)=0;
TTM(IMAX)=0;
TTTM(IMAX)=0;
QMN(IMAX)=0;
QMO(IMAX)=0;
T(KMAX)=0;
```

```
Q(IMAX)=0;
P(IMAX)=0;
X(IMAX)=0;
U(IMAX,KMAX)=0;
%-------------------BOUNDARY CONDITION-------------------
TB(1)=1;

%-----------------------SOLVING ------------------------
for K=1:KMAX
    T(K)=DELTAT*(K-1);
                  %CALCULATING BALLISTICE PART
 for I=1:IMAX
  X(I)=DELTAX*(I-1);
   MUT=X(I)/(KN*T(K));
      if  MUT<=1
                   % TEMPERATURE
      F1=exp(-2*X(I)/(KN*((1-MUT)*R(1)+(1+MUT))));

      G1=exp(-2*X(I)/(KN*((1-MUT)*R(2)+(1+MUT))));

      FF1=exp(-2*X(I)/(KN*((1-MUT)*R(3)+(1+MUT))));

      GG1=exp(-2*X(I)/(KN*((1-MUT)*R(4)+(1+MUT))));

      TB(I)=((C(1)*F1+C(2)*G1+C(3)*FF1+C(4)*GG1)*(1-
MUT)/4)+Z;
      P(1)=TB(1);
      TB(1)=1;


                  % HEAT FLUX
      F2=((1-MUT)*R(1)+(1+MUT))*exp(-2*X(I)/(KN*((1-
MUT)*R(1)+(1+MUT))))/2;

      G2=((1-MUT)*R(2)+(1+MUT))*exp(-2*X(I)/(KN*((1-
MUT)*R(2)+(1+MUT))))/2;

      FF2=((1-MUT)*R(3)+(1+MUT))*exp(-2*X(I)/(KN*((1-
MUT)*R(3)+(1+MUT))))/2;

      GG2=((1-MUT)*R(4)+(1+MUT))*exp(-2*X(I)/(KN*((1-
MUT)*R(4)+(1+MUT))))/2;
      QB(I)=(C(1)*F2+C(2)*G2+C(3)*FF2+C(4)*GG2)*(1-MUT)/4;

                        %HEAT FLUX GRADIENT
           if I~=1
           DQB(I)=-(2*TB(I)+(X(I)/(KN*T(K)^2))*exp(-
T(K)))/(2*KN);
           else
           DQB(I)=-(2*P(I)+(X(I)/(KN*T(K)^2))*exp(-
T(K)))/(2*KN);
```

```
            end

        else
        TB(I)=0;
        QB(I)=0;
        DQB(I)=0;
        end

 end


% ----------------------Calculating DIFFUSIVE PART-------
TMO(IMAX)=0;
TMN(IMAX)=0;
 S=-KN*DQB;
                                % TEMPERATURE
  while ERR>ERRMAX
  TMN(1)=(TMO(2)*(2*R2*A)+TTTM(1)*(DELTAT/2-
1+A*R2/(B*R1))+TTM(1)*...
          (2-
2*DELTAT*A*R2/(B*R1))+S(1)*DELTAT^2)/(1+DELTAT/2+2*A*R2...
          +A*R2/(B*R1));

  for I=2:IMAX-1
   TMN(I)=(TTM(I)*(2)+TMO(I+1)*(A*R2)+TMO(I-1)*(A*R2)+...
   TTTM(I)*(.5*DELTAT-
1)+S(I)*DELTAT^2)/(1+DELTAT/2+2*A*R2);
  end

  TMN(IMAX)=(TMO(IMAX-1)*(2*R2*A)+TTTM(IMAX)*(DELTAT/2-
1)...
            +TTM(IMAX)*(2-
2*A*R2*DELTAX*GAMA)+S(IMAX)*DELTAT^2)/...
             (1+DELTAT/2+2*A*R2);


 ERR=max(abs(TMN-TMO));
 TMO=TMN;
  end
                                % HEAT FLUX
 QMO=QMN;
 QMN(1)=(QMO(1)-KN*R1*(TMN(2)-TMN(1))/3)/(DELTAT+1);

 for  I=2:IMAX-1
   QMN(I)=(QMO(I)-KN*R1*(TMN(I+1)-TMN(I-1))/6)/(DELTAT+1);
 end

 QMN(IMAX)=(QMO(IMAX)-KN*R1*(TMN(IMAX)-TMN(IMAX-
1))/3)/(DELTAT+1);

TTTM=TTM;
```

```
TTM=TMN;
ERR=1;

TTOTAL=TB+TMN;
Q=QB+QMN;

U(1:IMAX,K)=TTOTAL;

end
```

Bibliography

[1] Ishikawa, K., Seki, M. and Tobe, S. (1993). Application of Thermal Spray Coatings to Prevent Corrosion of Construction in Japan, in *Thermal Spray Coatings*: *Research, Design and Applications*, C.C. Berndt and T.F. Bernecki (Eds), ASM International, Materials Park, OH, USA, pp. 679-684.

[2] Zhao, L., Lugscheider, E. (2002). Influence of the Spraying Processes on the Properties of 316L Stainless Steel Coatings. *Surface and Coatings Technology*, 162 (1), pp. 6-10.

[3] Fauchais, P., Etchart-salas, R., Rat, V., Coudert, J. –F., Caron, N. Wittmann-Teneze, K. (2008). Parameters controlling liquid plasma spraying : solutions, sols, or suspensions, *Journal of Thermal Spray Technology*, 17(1), pp. 31-59.

[4] Gadow, R., Killinger, A., Rauch, J. (2008). New results in High Velocity Suspension Flame Spraying (HVSFS). *Surface and Coatings Technology*, 202 (18), pp. 4329-4336.

[5] Chen, G. (2006). Nanoscale Heat Transfer and Nanostructured Thermoelectrics. *Components and Packaging Technologies, IEEE Transactions on*, 29 (2), pp. 238-246.

[6] Li, D., Huxtable, S., Abramson, A., Majumdar, A., (2005). Thermal Transport in Nanostructured Solid-State Cooling Devices. *ASME Journal of Heat Transfer*, 127 (1), pp. 108-114.

[7] Dongmo, E., Gadow, R., Wenzelburger, M. (2008). Analysis and Optimization of the HVOF Process by Combined Experimental and Numerical Approaches. *Surface & Coatings Technology*, 202 (18), pp. 4470–4478.

[8] Killinger, A. Gadow, R. Mauer, G. Guignard, A. Vasen, R. Stover, D. (2011). Review of New Developments in Suspension and Solution Precursor Thermal Spray Processes. *Journal of Thermal Spray Technology*, 20(4), pp. 677-695.

[9] Fauchais, P. Montavon, G. Vardelle, M. Cedelle, J. (2006). Development in direct current plasma spraying, *Surface and Coating Technology*, 5(201), pp. 1908-1921

[10] Lima, VR. S. Marple, B.R. (2007). Thermal spray coatings engineered from nano-structured ceramic agglomerated powders for structural, thermal barrier and biomedical applications: a review, *Journal of Thermal Spray Technology*, 16(1), pp. 40-63

[11] Dongmo, E. Killinger, A. Wenzelburger, M. Gadow R. (2009). Numerical approach and optimization of the combustion and gas dynamics in High Velocity Suspension Flame Spraying (HVSFS) . *Surface and Coating Technology*, 203(15), pp. 2139-2145.

[12] Davis, J.R. (Ed.). Handbook of Thermal Spray Technology. (2004). *Thermal Spray Society*, ASM International, Materials Park, OH, USA, pp. 338.

[13] Heinrich. P. Thermal spraying -Facts and state of the art. Sonderdruck, E10/92 (1992), pp. 28.

[14] Pawlowski, L. (1995). The science and engineering of thermal spray coatings. *John Wiley and Sons*, New York, NY, USA, pp. 432.

[15] Kulkarni, A. Gutleber, J. Sampath, S. Goland, A. Lindquist, W.B. Herman, H. Allen, A.J. and Dowd, B. (2004). Studies of the microstructure and properties of dense ceramic coatings produced by high-velocity oxygen-fuel combustion spraying. *Materials Science and Engineering*, A369, pp. 124.137.

[16] Ramm, D.A.J. Clyne, T.W. Sturgeon, A.J. and Dunkerton, S. (1994). Correlations between spraying conditions and microstructure for alumina coatings produced by HVOF and VPS. *Proceedings of the 7th National Thermal Spray Conference*, Boston, Massachusetts, USA, pp. 239-244.

[17] Sturgeon, A.J. Harvey, M.F.D. and Blunt, F.J. (1997). The influence of fuel gas on the microstructure and wear performance of alumina coatings produced by the High Velocity Oxyfuel (HVOF) thermal spray process. *British Ceramic Proceedings*, 54, pp. 57-64.

[18] Sturgeon, A.J. (1996). Recent advantages and applications of thermal sprayed ceramic coatings, *British Ceramic proceedings*, 55, pp. 3-12

[19] Kreye, H., Schwetzke, R. and Zimmermann, S. High velocity oxy-fuel flame spraying process and coating characteristics. Thermal Spray: Practical solutions for Engineering Problems. Berndt, C.C. (Ed.). Published by ASM International, Materials Park, Ohio-USA (1996), pp. 451.456.

[20] Li, M. Shi, D. and Christofides, P.D. (2004). Model-based estimation and control of particle velocity and melting in HVOF thermal spray. *Chemical Engineering Science*, 59(22-23), pp. 5647-5656.

[21] Power, G.D. Smith, E.B. Barber, T.J. Chiappetta, L.M. (1991). Analysis of a combustion (HVOF) spray deposition gun. Report 91-8, *United Technologies Research Centre*, East Hartford, Connecticut, USA.

[22] Smith, E. B. Power, G. D. Barber, T. J. and Chiappetta, L. M. (1992). Application of Computational Fluid Dynamics to the HVOF Thermal Spray Gun. *International Thermal Spray Conference*, Orlando, FL, pp. 805-810.

[23] Oberkampf, W.L. Talpallikar, M. (1996). Analysis of a high-velocity oxygen fuel (HVOF) thermal spray torch part 2: computational results. *Journal of Thermal Spray Technology*, 5, pp. 62-68.

[24] Chang, C. H., and Moore, R. L. (1995). Numerical simulation of gas and particle flow in HVOF torch. *Journal of Thermal Spray Technology*, 4, pp. 358-366.

[25] Eidelman, S. Yang, X. and Lottati, I. and Grossmann, W. (1995). Numerical simulation of thermal spray processing. *Proceeding 8th National Thermal Spray Conference*. Houston, Texas, pp. 219.

[26] Leonard, B. P. (1995). Order of accuracy of QUICK and related convection-diffusion schemes. *Applied Mathematical Modelling*, 19(11), pp. 640-653.

[27] Cheng, D. Xu, Q. Trapaga, G. Lavernia, E.J. (2001b). A numerical study of high-velocity oxygen fuel thermal spraying process. Part I: gas phase dynamics. *Metallurgical and Materials Transactions*, A 32, pp. 1609-1620.

[28] Dolatabadi, A. Mostaghimi, J. Pershin, V. (2002). Effect of a cylindrical shroud on particle conditions in high velocity oxy-fuel spray process. *Journal of Materials Processing Technology*, 3, pp. 245-525.

[29] Li, M., Christofides, P.D. (2005). Multi-scale modelling and analysis of HVOF thermal spray process. *Chemical Engineering Science*, 60(13), pp. 3649-3669.

[30] Shih, T.H. Liou, W.W. Shabbir A. and Zhu, J. (1995). A new $k-\varepsilon$ eddy viscosity model for high Reynolds number turbulent flows. *Computers and Fluids*, 24(3), pp. 227-238.

[31] Yang, X. Eidelman, S. (1996). Numerical analysis of a high-velocity oxygen fuel thermal spray system. *Journal of Thermal Spray Technology*, 5, pp. 175-184.

[32] Gu, S. Eastwick, C.N. Simmons, K.A. McCartney, D.G. (2001). Computational fluid dynamic modelling of gas flow characteristics in a high-velocity oxy-fuel thermal spray system. *Journal of Thermal Spray Technology*, 10(3), pp. 461-469.

[33] Hassan, B. Lopez, A.R. Oberkampf, W.L. (1998). Computational analysis of a three-dimensional high-velocity oxygen fuel (HVOF) thermal spray torch. *Journal of Thermal Spray Technology*, 7, pp. 71-77.

[34] Lopez, A. R. Hassan, B. Oberkampf, W. L. Neiser, A. R. Roemer, T. J. (1996). *Thermal Spray: Practical Solution for Engineering Problems* ed C C Berndt (Materials Park, Ohio, USA: ASM International), pp 531.

[35] Kamnis, S. and Gu, S. (2006). Numerical Modelling of Propane Combustion in a High Velocity Oxygen-Fuel Thermal Spray Gun. *Chemical Engineering Processes*, 45(4), pp. 246-253.

[36] Kamnis, S. Gu, S. 3-D (2006). Modelling of Kerosene-Fuelled HVOF Thermal Spray Gun. *Chemical Engineering Science*, 61(16), pp. 5427–5439.

[37] Voronetsky, A. V. Jagodnikov, D. A. Filimono, L. A. Suchkov, S. A. Shirjaeva, N. V. Elisseev, A. A. and Boronin, E. V. (1998). *Proceeding 15th International Thermal Spray Conference*, Nice, France, pp. 1393.

[38] Oberste-Berghaus, J. Legoux, J –G. Moreau, C. Hui, R. Deces-Petit, C. Qu, W. Yick, S. Wang, Z. Maric, R. Ghosh, D. (2008) Suspension and HVOF spraying of reduced temperature Solid Oxide Fuel Cell Electrolytes. *Journal of Thermal Spray Technology*, 17 (5-6), pp. 700-707.

[39] Stöver, D. Hathiramani, D. Vaßen, R. Damani, R. J. (2006) Plasma-sprayed components for SOFC applications. *Surface and Coatings Technology*, 201 (5), pp. 2002-2005.

[40] Maric, R. Roller, J. Neagu. R. (2011). Flame-Based Technologies and Reactive Spray Deposition Technology for Low-Temperature Solid Oxide Fuel Cells: Technical and Economic Aspects. *Journal of Thermal Spray Technology*, 20(4), pp. 696-718.

[41] Fauchais, P. Montavon, G. Lima, R. S. Marple, B. R. (2011). Engineering a new class of thermal spray nano-based microstructures from agglomerated nanostructured particles, suspensions and solutions: an invited review. *Journal of Physics D: Applied Physics*, 44 (9), pp. 1-53.

[42] Fauchais, P. Montavon, G. (2010). Latest Developments in Suspension and Liquid Precursor Thermal Spraying. *Journal of Thermal Spray Technology*, 19 (1-2), pp. 226-239.

[43] Pawlowski, L. (2008a). Finely grained nanometric and submicrometric coatings by thermal spraying: A review. *Surface and Coatings Technology*, 202(18), pp. 4318–4328.

[44] Pawlowski, L. (2009). Suspension and solution thermal spray coatings. *Surface and Coatings Technology*, 203(19), pp. 2807–2829.

[45] Huang, Y. Song, L. Liu, X. Xiao, Y. Wu, Y. Chen, J. Wu, F. Gu, Z. (2010). Hydroxyapatite coatings deposited by liquid precursor plasma spraying: controlled dense and porous microstructures and osteoblastic cell responses. *Biofabrication*, 2(4), pp. 1-10.

[46] Vaßen, R. Yi, Z. Kaßner, H. Stöver, D. (2009). Suspension plasma spraying of TiO_2 for the manufacture of photovoltaic cells. *Surface and Coatings Technology*, 203(15), pp. 2146-2149.

[47] Toma, F-L. Berger, L-M. Stahr, C. C. Naumann, T. Langner, S. (2010). Microstructures and functional properties of suspension-sprayed Al_2O_3 and TiO_2 coatings: an overview. *Journal of Thermal Spray Technology*, 19(1-2), pp. 262-274.

[48] Oberste-Berghaus, J. Legoux, J.-G. Moreau, C. Tarasi, F. Chraska, T. (2008). Mechanical and Thermal Transport Properties of Suspension Thermal-Sprayed Alumina-Zirconia Composite Coatings. *Journal of Thermal Spray Technology*, 17(1), pp. 91-104.

[49] Bolelli, G. Cannillo, V. Gadow, R. Killinger, A. Lusvarghi, L. Rauch, J. and Romagnoli, M. (2010). Effect of the Suspension Composition on the Microstructural Properties of High Velocity Suspension Flame Sprayed (HVSFS) Al2O3 Coatings. *Surface and Coatings Technology*, 204(8), pp. 1163-1179.

[50] Bemporad, E. Bolelli, G. Cannillo, V. De Felicis, D. Gadow, R. Killinger, A. and Lusvarghi, L. (2010). Structural Characterisation of High Velocity Suspension Flame Sprayed (HVSFS) TiO2 Coatings. *Surface and Coatings Technology*, 204(23), pp. 3902-3910.

[51] Stiegler, N. Bellucci, D. Bolelli, G. Cannillo, V. Gadow, R. Killinger, A. Lusvarghi, L. and Sola, A. (2012). High-Velocity Suspension Flame Sprayed (HVSFS) Hydroxyapatite Coatings for Biomedical Applications. *Journal of Thermal Spray Technology*, 21(2), pp. 275-287.

[52] Bertolissi, G. Chazelas, C. Bolelli, G. Lusvarghi, L. Vardelle, M. and Vardelle, A. (2012). Engineering the Microstructure of Solution Precursor Plasma-Sprayed Coatings. *Journal of Thermal Spray Technology*, 21(6), pp. 1148-1162.

[53] Chen, D. Jordan, E.H. and Gell, M. (2010). The Solution Precursor Plasma Spray Coatings Influence of Solvent Type. *Plasma Chemistry and Plasma Processing*, 30(1), pp. 111-119.

[54] Drew, D.A. Passman, S. L. (1999). Theory of Multicomponent Fluids, Springer, Berlin, Heidelberg, New York.

[55] Murshed, S.M.S. Leong, K.C. Yang, C. (2008). Investigations of thermal conductivity and viscosity of nanofluids. *International Journal of Thermal Sciences*, 47(5), pp. 560-568.

[56] Xuan, Y. Roetzel, W. (2000). Conceptions for heat transfer correlation of nanofluids. *International Journal of Heat and Mass Transfer*, 43(19), 3701-3707.

[57] Gao J.W., Zheng, R.T. Ohtani, H. Zhu, D.S. Chen, G. (2009). Experimental Investigation of Heat Conduction Mechanisms in Nanofluids. Clue on Clustering. *NanoLetters*, 9 (12), 4128–4132.

[58] Tanvir, S. Qiao, L. (2012). Surface tension of Nanofluid-type fuels containing suspended nanomaterials. *Nanoscale Research Letters*, 7, 226.

[59] Moosavi, M. Goharshadi, E.K. Youssefi, A. (2010). Fabrication, characterization, and measurement of some physicochemical properties of ZnO nanofluids. *International Journal of Heat Fluid Flow*, 31(4), pp. 599-605.

[60] Chen, RH. Phuoc, T. X. Martello, D. (2010). Effects of nanoparticles on nanofluid droplet evaporation. *International Journal of Heat and Mass Transfer*, 53(19-20), pp. 3677-3682.

[61] Xiong, H.B. and Lin, J.Z. (2009). Nanoparticles Modelling in Axially Injection Suspension Plasma Spray of Zirconia and Alumina Ceramics. *Journal of Thermal Spray Technology*, 18(5-6), 887-895.

[62] Mao, J.N. Chen, H.X. Jia, H. Qian, X.L. (2012). The transient behaviour of peltier junctions pulsed with supercooling. *Journal of Applied Physics*, 112.

[63] Zhou, Q. Bian, Z. Shakouri, A. (2012). Pulsed cooling of inhomogeneous thermoelectric materials. *Journal of Applied Physics*, 40, pp. 4376-4381.

[64] Lepri, S. Livi, R. Politi, A. (2003). Thermal conduction in classical low-dimensional lattices, *Physics Reports*. 377(1), pp. 1-80.

[65] Tien, C. L. Majumdar, A. and Gerner, F. M., (1998). Microscale Energy Transport. Taylor & Francis, Washington, DC.

[66] Cattaneo, C. (1958). A form of heat conduction which eliminates the paradox of instantaneous propagation. *Compte Rendus*, 247, pp. 431-433.

[67] Figueroa, A. Vazquez, F. (2014). Optimal performance and entropy generation transition from micro to nanoscaled thermoelectric layers. *International Journal of Heat and Mass Transfer*, 71, pp. 724-731.

[68] Chen, G. (2001). Ballistic-Diffusive Heat Conduction Equations. *Physical Review Letters*, 86, pp. 2297–2300.

[69] Chen, G. (2002). Ballistic-Diffusive Equations for Transient Heat ConductionFrom Nano to Macroscales. *ASME Journal of Heat Transfer*, 124, pp. 320–328.

[70] Stettler, M. Alam, M. Lundstrom, M. (1993). A critical examination of the assumptions underlying macroscopic transport equations for silicon devices. *IEEE Trans*, 40, pp. 733–740.

[71] Lee, K.H. Kim, O.J. (2007). Analysis on the cooling performance of the thermoelectric micro-cooler. *Int. J. Heat Mass Transfer*, 50, pp. 1982–1992.

[72] Lee, K.H. Kim, H. Kim, O.J. (2010). Effect of thermoelectric and electrical properties on the cooling performance of a micro thermoelectric cooler. *J. Electron. Mater*, 39, pp. 1566–1571.

[73] Sellito, A. Cimmelli, V. Jou, D. (2013). Thermoelectric effects and size dependency of the figure-of-merit in cylindrical nanowires. *Int. J. Heat Mass Transfer*, 57, pp. 109–116.

[74] Shakouri, A. (2006). Nanoscale Thermal Transport and Microrefrigerators on a chip, *Proceeding of The IEEE*, 94, pp. 1613 - 1638.

[75] Minnich, A. Dresselhaus, M. Ren, Z. Chen, G. (2009). Bulk nanostructured thermoelectric materials: current research and future prospects, *Energy Environ. Sci.*, 2, pp. 466–479.

[76] Dubi, Y. Ventra, M.D. 83 (2011). Colloquium: heat flow and thermoelectricity in atomic and molecular junctions, *Rev. Modern Phys,*. Pp. 131–155.

[77] Van Doormal, J.P. Raithby, G.D. McDonald, B.H. (1987). The segregated approach to predicting viscous compressible fluid flows. *ASME Journal of Turbomachinery*, 109, pp. 268-277.

[78] Peric, M. (1990). Analysis of pressure-velocity coupling on non-orthogonal grids. *Numerical Heat Transfer, Part B: Fundamentals*, 17, pp. 63-82.

[79] Raithby, G.D. Schneider, G.E. (1979). Numerical solution of problems in compressible fluid flow: Treatment of the velocity-pressure coupling. *Numerical heat transfer*, 2, pp. 417-440.

[80] Launder, B.E. and Spalding, D.B. (1972). Lectures in Mathematical Models of Turbulence, Academic Press, London, England.

[81] Shih, T.H. Liou, W.W. Shabbir, A. and Zhu, J. (1995). A new $K-\varepsilon$ eddy viscosity model for high Reynolds number turbulent flows. *Computers and Fluids*, 24(3), pp. 227-238.

[82] Furuhata, T. Tanno, S. Miura, T. Ikeda, Y. and Nakajima, T. (1997). Performance of numerical spray combustion simulation. *Energy Conversion and Management*, 38(10-13), pp. 1111-1122.

[83] Haider, A. Levenspiel, O. (1989). Drag coefficient and terminal velocity of spherical and nonspherical particles. *Powder Technology*, 58(1), pp. 63-70.

[84] Ranz, W. E. and Marshall, W. R. (1952a). Evaporation from drops, Part I. *Chemical Engineering Progress*, 48 (3), pp. 141-146.

[85] Ranz, W. E. and Marshall, W. R. (1952b). Evaporation from drops, Part II. *Chemical Engineering Progress*, 48 (4), pp. 173-180.

[86] Kuo, K. K. Y. (1986). Principles of Combustion. John Wiley and Sons, New York.

[87] Rourke, P.J. Oand Amsden, A.A. (1987). The TAB Method for Numerical Calculation of Spray Droplet Breakup. *SAE Technical Paper*, 872089, SAE. pp. 12.

[88] Reitz, R. D. (1987). Mechanisms of Atomization Processes in High-Pressure Vaporizing Sprays. *Atomization and Spray Technology*, 3 (4), pp. 309–337.

[89] Liu, A. B. Mather, D. and Reitz, R. D. (1993). Modelling the Effects of Drop Drag and Breakup on Fuel Sprays. *SAE Technical Paper*, 930072, SAE.

[90] Zeoli, N., Gu, S., Kamnis, S. (2008). Numerical Simulation of in-Flight Particle Oxidation during Thermal Spraying. *Computers & Chemical Engineering*, 32 (7), pp. 1661-1668.

[91] Zeoli, N., Gu, S., Kamnis, S. (2008). Numerical Modelling of Metal Droplet Cooling and Solidification. *International Journal of Heat and Mass Transfer*, 51 (15-16), pp. 4121-4131.

[92] Gozali, E. Kamnis, S. Gu, S. (2013). Numerical investigation of combustion and liquid feedstock in high velocity suspension flame spraying process. *Surface and Coatings Technology*, 228, pp. 176-186.

[93] Miller, R. S. Harstad, K. and Bellan, J. (1998). Evaluation of Equilibrium and Non-Equilibrium Evaporation Models for Many Droplet Gas-Liquid Flow Simulations. *International Journal of Multiphase Flow*, 24(6), pp. 1025 –1055.

[94] Sazhin, S. S. (2006). Advanced Models of Fuel Droplet Heating and Evaporation. *Progress in Energy Combustion Science*, 32, pp. 162–214.

[95] Perry, R.H. Green D.W. Perry's Chemical Engineers' Handbook, 7th ed., McGraw-Hill, 1997.

[96] Brinkman, H.C. (1952). The Viscosity of Concentrated Suspensions and Solutions. *Journal of Chemical Physics*, 20, pp. 571-581.

[97] Wang, B.X. Zhou, L.P. Peng, X.F. (2003). A Fractal Model for Predicting the Effective Thermal Conductivity of Liquid with Suspension of Nanoparticles. *International Journal of Heat and Mass Transfer*, 46(14), pp. 2665-2672.

[98] Li, M. and Christofides, P.D. (2006). Computational study of particle in-flight behavior in the HVOF thermal spray process. *Chemical Engineering Science*, 61(19), pp. 6540–6552.

[99] Goldsmid, H.J. (1986). Electronic refrigeration, New York: Plenum Press.

[100] Parrott, J.E. (1960). Interpretation of stationary and transient behaviour of refrigerating thermocouples. *Solid State Electron*, 1, pp. 135–43.

[101] Landecker, K. Findlay, A.W. (1961). Study of fast transient behaviour of Peltier junctions. *Solid State Electron*, 2, pp. 239–60.

[102] Idnurm, M. Landecker, K. (1963). Experiments with Peltier junctions pulsed with high transient currents. *Journal of Applied Physics*, 34, pp. 1806–10.

[103] Babin, V.P. Iordanishvili, E.K. (1969). Enhancement of thermoelectric cooling in nonstationary operation. *Soviet Physics – Technical Physics*, 14, pp. 293–8.

[104] Hoyos, G.E. Rao, K.R. Jerger, D. (1977). Fast transient response of novel Peltier junctions. *Energy Conversion*, 17, pp. 23–9.

[105] Field, R.L. Blum, H.A. (1979). Fast transient behavior of thermoelectric coolers with high current pulse and finite cold junction. Energy Conversion, 19, pp.159–65.

[106] Miner, A. Majumdar, A. Ghoshal, U. (1999). Thermoelectromechanical refrigeration based on transient thermoelectric effects. Applied Physics Letters, 75, pp. 1176–8.

[107] Snyder, G.J. Fleurial, J.P. Caillat, T. Yang, R.G. Chen, G. (2002). Supercooling of Peltier cooler using a current pulse. Journal of Applied Physics, 92(3), pp. 1564.

[108] Hoyos, G.E. Rao, K.R. Jerger, D. (1977). Numerical analysis of transient behaviour of thermoelectric coolers. Energy Conversion, 17, pp. 45–54.

[109] Landecker, K. (1974). Some further remarks on the improvements of Peltier junctions for thermoelectric cooling. Energy Conversion, 14, pp. 21–33.

[110] Kumar, R. Yang, R.G. Chen, G. Fleurial, J.P. (2000). Transient thermoelectric cooling of thin film devices. *International Proceedings of the MRS Spring meeting*, 626.

[111] Stilbans, L.S. Fedorovich, N.A. (1958). Cooling of thermoelectric cells under nonstationary conditions. *Soviet Physics – Technical Physics*, 3, pp. 460.

[112] Zhao, D. Tan, G. (2014). A review of thermoelectric cooling: Materials, modelling and applications. *Applied Thermal Engineering*, 66(1-2), pp. 15-24.

[113] Vernotte, P. (1958). Les paradoxes de la theorie continue de lequation de la chleur, *compte Rendus*, 252, pp. 3154-3155.

[114] Alvarez, F.X. Jou, D. (2007). Memory and nonlocal effects in heat transport: from diffusive to ballistic regimes. Applied Physics Letters, 90(8).

[115] Dai, W. Shen, L. Nassar, R. Zhu, T. (2004). A stable and convergent three-level finite difference scheme for solving a dual-phase-lagging heat transport equation in spherical coordinates. *International Journal of Heat and Mass Transfer*, 47(8-9), pp. 1817-1825.

[116] ANSYS FLUENT Theory Guide. (2013).